Karlsruher Institut für Technologie

Tritiumlabor Karlsruhe

Investigation and Reduction of Rear Wall Systematics relevant for keV sterile Neutrino Search with KATRIN

Zur Erlangung des akademischen Grades eines

Doktors der Naturwissenschaften (Dr. rer. nat.)

von der KIT-Fakultät für Physik
des Karlsruher Instituts für Technologie (KIT)

angenommene

Dissertation

von

M. Sc. Dominic Batzler

aus Bruchsal

Referent: Prof. Dr. Guido Drexlin
Korreferentin: Prof. Dr. Susanne Mertens

Tag der mündlichen Prüfung: 11. Juli 2025

Declaration of Authorship

I declare that I have developed and written the enclosed thesis completely by myself. I have not used any other than the aids that I have mentioned. I have marked all parts of the thesis that I have included from referenced literature, either in their original wording or paraphrasing their contents. I have followed the by-laws to implement scientific integrity at KIT.

Selbstständigkeitserklärung

Ich versichere wahrheitsgemäß, die Arbeit selbstständig verfasst, alle benutzten Quellen und Hilfsmittel vollständig und genau angegeben und alles kenntlich gemacht zu haben, was aus Arbeiten anderer unverändert oder mit Abänderungen entnommen wurde sowie die Satzung des KIT zur Sicherung guter wissenschaftlicher Praxis in der jeweils gültigen Fassung beachtet zu haben.

Karlsruhe, den 04. Juni 2025

Dominic Batzler

Abstract

The Karlsruhe Tritium Neutrino (KATRIN) experiment performs high-precision β-spectroscopy near the kinematic endpoint of tritium decay, with the aim to measure the effective electron antineutrino mass with a sensitivity of better than 0.3 eV. After achieving this goal, the setup will be upgraded to search for keV-scale sterile neutrinos in the scope of the Tritium Investigation on Sterile to Active Neutrino Mixing (TRISTAN) project. Reaching the target sensitivity on the mixing amplitude of 10^{-6} requires precise modelling of all the systematic effects. The subject of this thesis is the Rear Wall (RW), which is a gold-coated stainless steel disk and the physical upstream end of the tritium source. There are two systematic effects associated with the RW: inelastic electron backscattering and surface activity. Modelling the measured spectrum more accurately required replacing the currently available RW datasets describing these effects. Using the Monte Carlo toolkit Geant4, a new simulation code was created to study the interactions of electrons with the RW surface. Due to developing performance-enhancing options, new RW datasets could be generated by simulating up to 280 times more electrons than before. Possibilities to reduce both electron backscattering from the RW, and RW activity were explored experimentally. Surface activity can be removed by in-situ UV/ozone decontamination, which is not yet fully understood. To improve upon the knowledge on the underlying mechanism, and to extend the method to tritium systems in general, a dedicated experiment was set up to study the properties of ozone in vacuum vessels. By applying the findings to a tritiated sample, 60% of its surface activity could be removed. However, no inherent decontamination effect of ozone without simultaneous UV irradiation was found. Electron backscattering from the RW can be reduced significantly by replacing it with a material possessing a lower nuclear charge number. One of the possible upgrades for the TRISTAN project is installing a new RW made of beryllium. However, it has not been clear yet whether beryllium is compatible with the conditions inside the tritium source. An experimental routine, including e.g. tests on tritium accumulation, was developed, with which alternative RW materials can be qualified. The first tests performed on beryllium did not provide any reason to exclude its use as an alternative RW.

Contents

List of Figures

List of Tables

Acronyms

AES Auger electron spectroscopy

BIXS beta-induced X-ray spectrometry

CPS cryogenic pumping section

DPS differential pumping section

FPD focal plane detector

FSD final state distribution

FTIR Fourier transform infrared

HITRAN high-resolution transmission molecular absorption database

IR infrared

KATRIN Karlsruhe Tritium Neutrino

KNM KATRIN neutrino-mass campaign

MAC-E Magnetic Adiabatic Collimation with Electrostatic

RW Rear Wall

SDD silicon drift detector

TLK Tritium Laboratory Karlsruhe

TMP turbo-molecular pump

TRACE Tritium Activity Chamber Experiment

TRIADE Tritium Adsorption Desorption Experiment

TRISTAN Tritium Investigation on Sterile to Active Neutrino Mixing

UV ultra-violet

UVO ultra-violet ozone

WGTS windowless gaseous tritium source

Chapter 1

Introduction

Neutrinos are the most abundant massive particle in the universe. Although assumed to be massless in the Standard Model of particle physics, the evidence of neutrino flavour oscillations (McDonald et al., 2002) hints towards neutrinos possessing a non-zero mass. However, from these experiments, the absolute mass scale of the neutrinos cannot be inferred. A method to determine the neutrino mass in a model-independent way is high-precision spectroscopy of electrons generated from β-decay.

The Karlsruhe Tritium Neutrino (KATRIN) experiment (Aker et al., 2021a) follows this approach by using the combination of a high-resolution integrating spectrometer of Magnetic Adiabatic Collimation with Electrostatic (MAC-E) filter type (Lobashev & Spivak, 1985; Picard et al., 1992), and a high-luminosity windowless gaseous tritium source (WGTS) (Marsteller, 2020) to measure the tritium spectrum near the kinematic endpoint. It is currently the world-leading experiment of this type, resulting in an upper limit on the electron antineutrino mass of 0.45 eV at 90% C.L., as published recently (Aker et al., 2025). After reaching its sensitivity goal of better than 0.3 eV with 1000 measurement days by the end of 2025, KATRIN transitions into the next phase.

Within the Tritium Investigation on Sterile to Active Neutrino Mixing (TRISTAN) project (Mertens et al., 2019), the new objective is the search for sterile neutrinos on the keV mass scale (Dodelson & Widrow, 1994). Their postulation is an extension of the Standard Model, which could explain the small masses of the known active neutrinos through the seesaw mechanism (Minkowski, 1977). Since the exact sterile neutrino mass is not known, the system will be upgraded to differentially measure the tritium β-spectrum with an energy range spanning the majority of the spectrum. Reaching the target sensitivity on the sterile to active mixing amplitude of $< 10^{-6}$ necessitates a thorough study of systematic effects – both known ones from KATRIN, and expected new ones. This can be done with the TRModel (Descher, 2024), which is a Python-based software which includes various systematic effects.

Two systematic effects stem from the Rear Wall (RW), which is a gold-coated stainless steel disk and the physical upstream end of the WGTS. Contributing to studying them and investigating ways to suppress them is central to this work. One of them is known from KATRIN's current operation mode: the accumulation of surface activity during tri-

tium circulation (Aker, 2025). This results in a secondary β-spectrum with a slightly shifted endpoint that acts as a background, whose signal can increase over time. A countermeasure was identified in the UV/ozone decontamination method, which was applied to the KATRIN RW multiple times (Aker et al., 2024). How that mechanism achieves its decontamination efficiency is not yet clear, but understanding it is required to optimise and extend it to tritium handling systems in general. The second effect arises from the extended region of interest. β-electrons can inelastically backscatter from the RW and be detected, while having lost information on the decay during the interaction with the RW surface. This leads to a distortion of the measured spectrum. Since it is expected to be the most dominant systematic effect for measurements far below the endpoint, electron backscattering is of particular interest. Multiple concepts to mitigate it are being studied through theory and simulation. This thesis focuses on the possibility to replace the golden RW with one made of beryllium, which provides a significantly reduced backscattering probability due to its low nuclear charge. Prior to seriously considering beryllium as a candidate material, a qualification routine including tests for tritium compatibility will have to be developed and conducted. To better study systematic effects, including the RW, the TRModel is being updated. This requires improved, external input using Geant4, which will be provided for the RW effects in the scope of this work.

This thesis is structured as follows: chapter 2 gives a brief overview of KATRIN's current and future measurement mode for the search of active and sterile neutrinos, respectively, as well as relevant hardware components. A model description of RW activity and backscattering, including thorough analysis of the simulation results, as well as the generation of the new RW inputs, performed with the Monte Carlo toolkit Geant4 is presented in chapter 3. The investigation of ozone properties in the context of UV/ozone cleaning, as well as a first application on a tritiated sample is given in chapter 4. Measurements for a qualification routine of alternative RW materials are treated in chapter 5, together with preliminary studies on the suitability of beryllium. This work is concluded in chapter 6 with a summary of the key results, as well as potential future measurements and improvements.

Chapter 2

Direct neutrino mass measurement with the KATRIN experiment

The non-zero value of the neutrino mass remains one of the last unsolved issues of the Standard Model of particle physics. One approach to determine it is through direct measurement using tritium β-decay, which is pursued with the Karlsruhe Tritium Neutrino (KATRIN) experiment. After the neutrino mass measurements are concluded, the setup will be upgraded to scan the β-spectrum for the signature of sterile neutrinos of the keV mass scale. This creates new systematic effects related to the upstream end of the tritium source, the Rear Wall (RW), which need to be mitigated. This chapter introduces KATRIN's measurement principle, the relevant hardware, as well as the systematic effects. Finally, the goals of this work are presented.

2.1 Tritium β-decay

KATRIN is based on the β-decay of molecular tritium, according to

$$\mathrm{T_2} \rightarrow {}^3\mathrm{HeT}^+ + \mathrm{e}^- + \bar{\nu}_e, \tag{2.1}$$

with the resulting energy being distributed amongst the decay products. For most of the decays, the ${}^3\mathrm{HeT}^+$ nucleus carries the least amount of energy in the form of recoil and vibronic excitations, which is taken into account by the theoretical description of the final state distribution (FSD) (Saenz et al., 2000; Bodine et al., 2015; Schneidewind et al., 2024). The remaining energy is transferred to the electron and neutrino as kinetic energy. Since neutrinos only interact weakly with matter, detecting them directly is not viable. However, by accurately measuring the electron energy spectrum close to the kinematic endpoint E_0 of around 18.6 keV (Kleesiek et al., 2019), the electron neutrino rest mass (to be more precise: the weighted sum of the three mass eigenstates) can be inferred. Using Fermi's golden rule (Fermi, 1934), it is possible to calculate the β-spectrum including a neutrino of any mass. This can be done in principle with any β-emitter, but using

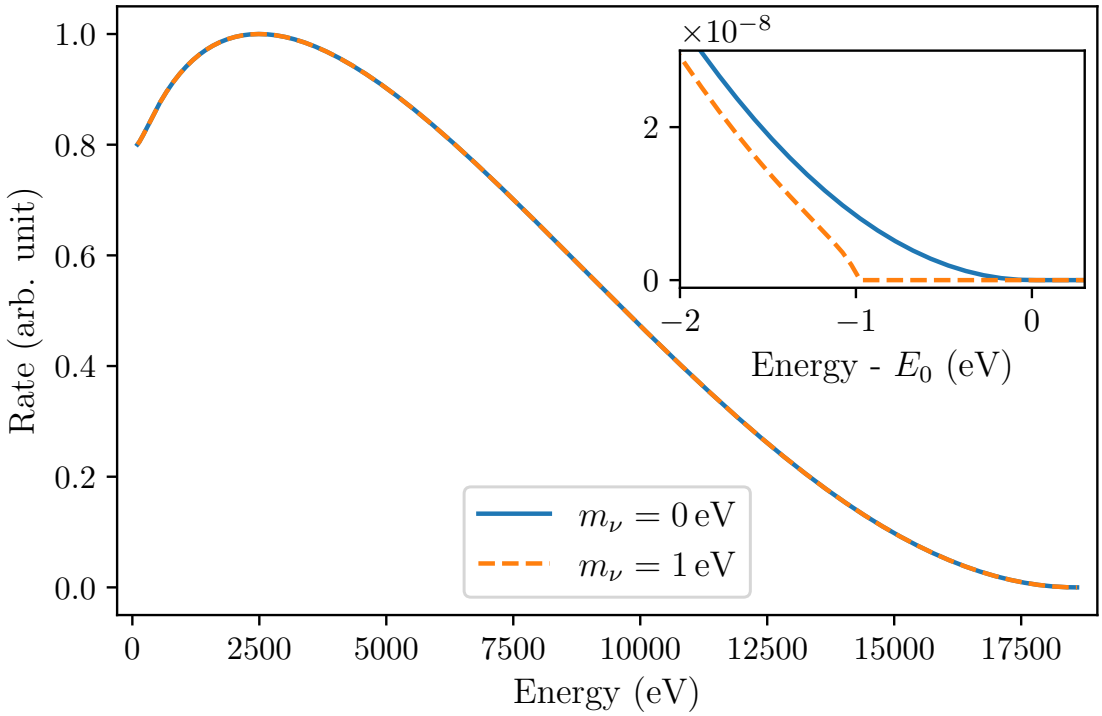

Figure 2.1: Tritium β-spectrum with and without massive neutrino. The signature of the neutrino's effective mass is visible around the endpoint E_0, leading to both a shift and a change in shape.

tritium has certain advantages. Its short half-life of around 12.3 years leads to a high decay rate and hence a large number of signal electrons (Lucas & Unterweger, 2000). Another favourable property is the low energy difference between parent and daughter nuclei leading to the low endpoint energy. This results in a maximum relative distortion of the spectrum caused by the generation of the neutrino (Myers et al., 2015).

Figure 2.1 illustrates the tritium β-decay spectrum, as well as the impact of an arbitrary neutrino mass of $m_\nu = 1\,\mathrm{eV}$ on its endpoint region. In case of a massless neutrino (blue curve), the electron energy extends all the way to the endpoint, while it vanishes 1 eV below it for the massive neutrino (dashed orange curve). Apart from the shift, the overall shape of the spectrum also changes.

In the past, multiple experiments used this approach in search for the neutrino mass, namely Los Alamos (Wilkerson et al., 1991), Mainz (Kraus et al., 2005), and Troitsk (Aseev et al., 2011). Eventually, an upper limit of the neutrino mass of 2 eV was found (Otten & Weinheimer, 2008). KATRIN as a successor experiment follows the same measurement principle and has started tritium scanning in 2019.

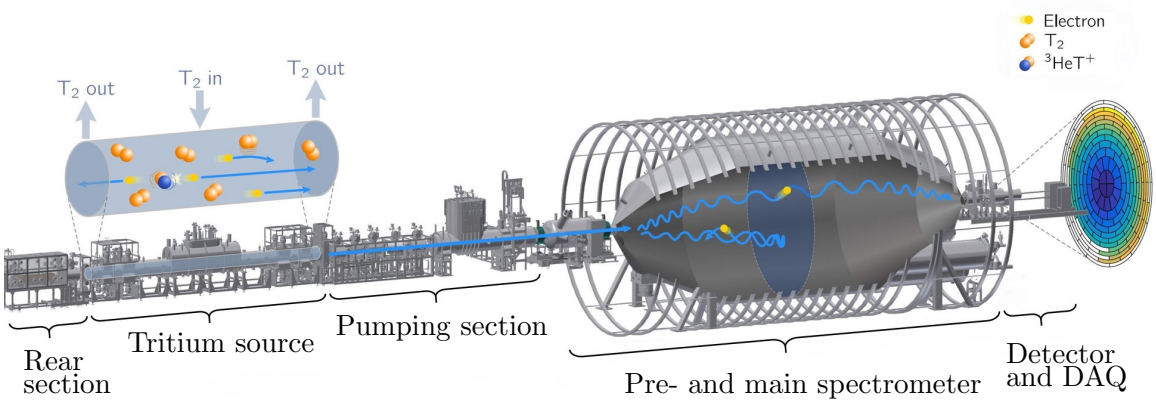

Figure 2.2: The KATRIN beamline, which is 70 m long in total. Adapted from Aker et al. (2022) under the CC BY 4.0 license https://creativecommons.org/licenses/by/4.0/.

2.2 The KATRIN experiment

Up until now, the KATRIN experiment has lowered the upper limit on the neutrino mass multiple times, with the latest result being 0.45 eV (Aker et al., 2019, 2022; Aker et al., 2025). By the end of 2025, the collaboration aims to reach a sensitivity of better than 0.3 eV at 90% C.L. on the neutrino mass (Aker et al., 2025). This is achievable by a combination of improved energy resolution and tritium source luminosity with respect to its predecessor experiments (Lobashev, 2003). The KATRIN beamline is shown in Figure 2.2. A detailed description of the entire experimental setup is given in Aker et al. (2021a).

2.2.1 The windowless gaseous tritium source

The signal electrons are generated in the windowless gaseous tritium source (WGTS) (Marsteller, 2020), located inside Tritium Laboratory Karlsruhe (TLK). With a throughput of up to 40 g of high-purity tritium per day (Sturm et al., 2021; Hillesheimer et al., 2023), up to 10^{11} electrons are generated each second by tritium decay (Aker et al., 2021a). The amount of gas present in the WGTS is represented by the nominal column density $\rho d_{\mathrm{nom}} = 5 \cdot 10^{17}\,\mathrm{cm}^{-2}$ (Aker et al., 2021a; Block, 2022). During neutrino mass measurements, the column density is maintained at 75% of the nominal value. The potential within the WGTS serves as the reference point for applying the retarding voltage to the main spectrometer. To study the source potential, e.g. its homogeneity, metastable krypton can be injected, which emits multiple instances of mono-energetic electrons with energies of up to 32.1 keV via internal conversion (Vénos et al., 2018; Marsteller et al., 2022; Acharya et al., 2025). Since the beamtube is unobstructed for its entire length from source to the detector, it is required to prevent the tritium from entering the spectrometers and by that elevating the background. This is realised by the differential and cryogenic pumping

sections (DPS and CPS), which connect the WGTS to the pre-spectrometer. Since both sections are curved, the electrons are guided through them adiabatically via magnetic field lines generated by numerous normal and superconducting magnets along the beamline. The neutral, molecular tritium, which is unaffected by the magnetic field, is pumped off by several turbo-molecular pumps (TMPs) along the beamtube. Over the length of the DPS, the tritium flow is reduced by more than seven orders of magnitude (Marsteller et al., 2021). The CPS is the final barrier for the tritium to the spectrometer hall. Its inner surface is gold-coated and, operated at a temperature of around 3 K, covered in argon frost on which the residual tritium freezes out. Using this concept, the tritium flow is reduced by another eight orders of magnitude (Röttele et al., 2023). Both sections together successfully reduce the tritium-induced background in the main spectrometer to a sufficiently low rate of less than 10^{-3} counts per second (Aker et al., 2021a).

2.2.2 Spectrometer and detector section

The decay electrons being magnetically guided through the DPS and CPS eventually reach the pre- and main spectrometers. Both spectrometers are of Magnetic Adiabatic Collimation with Electrostatic (MAC-E) filter type (Lobashev & Spivak, 1985; Picard et al., 1992). The excellent energy resolution is achieved by converting the electrons' transverse energy from cyclotron motion into their longitudinal energy, while conserving their total energy. This is possible if the magnetic field strength changes little over a cyclotron radius. By gradually reducing the magnetic field strength to a minimum, the MAC-E filter's energy resolution, according to

$$\frac{\Delta E}{E} = \frac{B_{\mathrm{min}}}{B_{\mathrm{max}}}, \tag{2.2}$$

is realised. In the case of KATRIN's main spectrometer, this corresponds to $\Delta E = 0.93\,\mathrm{eV}$ at an energy of 18.6 keV (Aker et al., 2021a). By applying a voltage U_0, the energy selection is performed, since only electrons with longitudinal energies $E > eU_0$ are transmitted through the spectrometer. Varying U_0 enables measuring an integral spectrum using the focal plane detector (FPD). The FPD is a silicon PIN diode with 148 pixels and a high detection efficiency of more than 90% for electrons in the relevant energy range (Amsbaugh et al., 2015). It resides behind the pinch magnet, which creates the highest magnetic field of 4.2 T in the beamline and reduces the diameter of the magnetic flux tube. Before reaching the detector, the electrons are accelerated by 10 keV for background mitigation. For the neutrino mass measurements, the region of interest is typically down to 40 eV below the endpoint. Due to the low count rates at these energies, a high-luminosity tritium source was required.

2.2.3 The Rear Wall

The RW (Figure 2.3) is located at the upstream end and marks the physical limit of the WGTS. It consists of a stainless steel disk with a diameter of roughly 14.5 cm, which is sputter-coated with a gold layer of 1 µm thickness (Schönung, 2016). For the neutrino

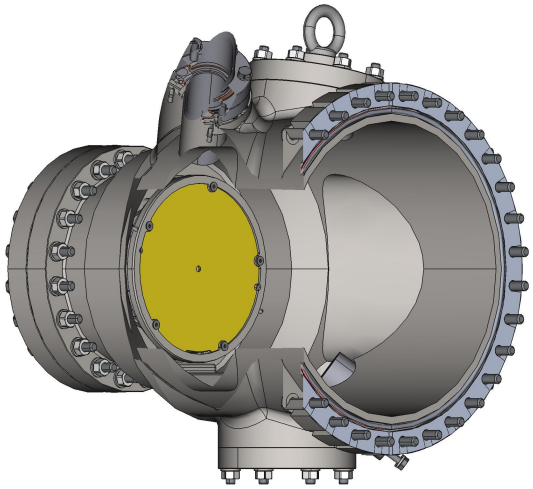

Figure 2.3: CAD model of the golden RW in its vessel located at the upstream end of the WGTS.

mass measurements, the RW serves multiple purposes, e.g. the termination of the magnetic flux tube. The magnetic field strength at the RW is 1.26 T. In addition, the RW is used to control the β-electrons' starting potential inside the WGTS by applying a voltage. The latter point is possible because at nominal source strength, a cold plasma from the tritium decay including secondary ionisation processes forms (Kuckert, 2016; Kellerer, 2022), which couples to the RW due to the magnetic field (Schönung, 2016).

The fact that the RW is directly mapped onto the detector comes with a drawback. As tritium is circulated through the WGTS, a small portion of it will be adsorbed on the nearby surfaces – including the RW. Tritium decay from its surface inevitably generates a background signal in the form of a secondary β-spectrum with a measurably different endpoint energy (Aker, 2025), that has to be accounted for in the neutrino mass analysis (Aker et al., 2025). With increasing cumulative tritium flow over time, the RW activity increases, as shown in Figure 2.4, which in turn leads to a growing systematic uncertainty on the neutrino mass. The rates depicted are extrapolated to a main spectrometer voltage of 0 V and were measured with the FPD while the WGTS was empty. These measurements were performed regularly during the KATRIN neutrino-mass campaigns (KNMs). During KNM5 and 6 (blue crosses), the RW activity increased rapidly, followed by a reduced, linear increase. The RW chamber (Figure 2.3) is equipped with optical ports for ultra-violet (UV) illumination, which can be used for UV/ozone decontamination of the RW (chapter 4, Aker et al., 2024). This was performed twice between KNM6 and KNM8. At the start of KNM8, after an initial increase in activity, the RW surface appears to have saturated (orange dots). A thorough investigation of this effect is available in Aker (2025).

In view of the aforementioned task of controlling the starting potential in the WGTS, as well as tritium accumulation, gold as a RW material presented itself as the ideal choice

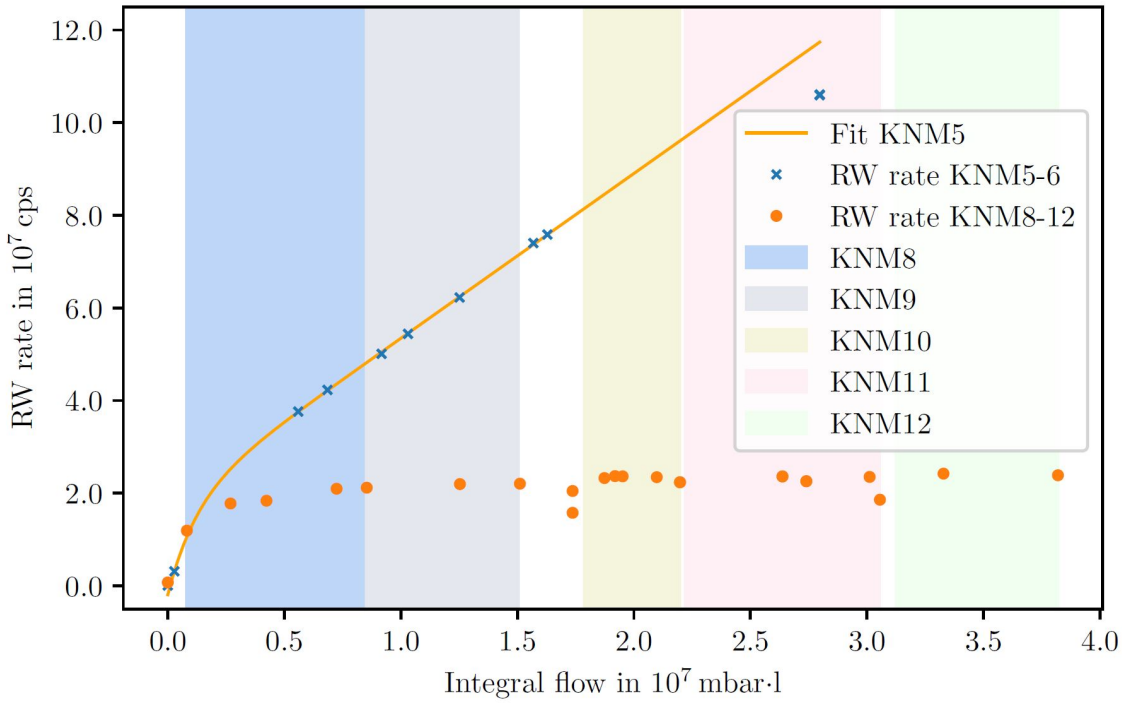

Figure 2.4: RW rate increase due to tritium accumulation on its surface over integral flow through the WGTS. The different behaviour of the rate evolutions for KNM5+6 and KNM8+ were traced back to the two UV/ozone decontaminations in between. Figure as published in Aker (2025) under the CC BY 4.0 license https://creativecommons.org/licenses/by/4.0/.

for KATRIN. It is a good electric conductor with a homogeneous surface potential, and is chemically inert which reduces tritium uptake to a minimum (Babutzka, 2014). It additionally enables monitoring of the source activity via beta-induced X-ray spectrometry (BIXS) due to its high nuclear charge number (Röllig, 2015). Tailored towards KATRIN's goal of measuring the neutrino mass, the current RW is suboptimal for the next phase of KATRIN: the Tritium Investigation on Sterile to Active Neutrino Mixing (TRISTAN) project. Its goal is the search for sterile neutrinos of keV mass scale and it is planned to run for two years. A brief overview of the future measurement mode is given in the next section.

2.3 Searching for keV-scale sterile neutrinos with TRISTAN

Sterile neutrinos are a theoretical extension to the Standard Model and would be the right-handed counterpart to the active neutrinos (Dodelson & Widrow, 1994). A fourth, relatively large mass eigenstate could potentially explain the small masses of the active

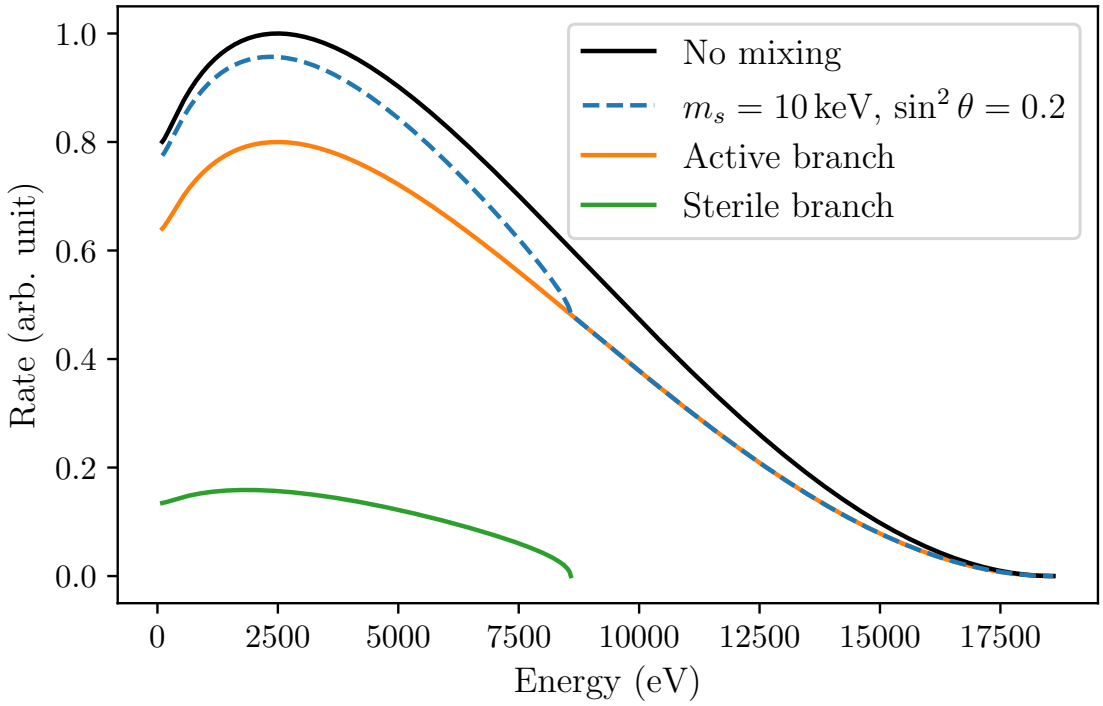

Figure 2.5: Tritium β-spectrum with a sterile neutrino of keV mass scale. The mixing with the active neutrinos generates an active (orange) and sterile (green) branch. In the superimposed spectrum (blue dashed) this is visible as a kink. An arbitrary sterile mass and an exaggerated mixing were chosen in this example.

neutrinos through the type-I seesaw mechanism (e.g. Minkowski, 1977; Mohapatra and Senjanović, 1980; Schechter and Valle, 1980; Yanagida, 1980). In addition, sterile neutrinos on the keV mass scale are a promising candidate for warm dark matter (e.g. Dodelson and Widrow, 1994; Abazajian et al., 2001; Dolgov and Hansen, 2002).

A sterile neutrino could couple to the active ones given by the differential decay rate

$$\frac{\mathrm{d}\Gamma}{\mathrm{d}E} = \cos^2\theta \, \frac{\mathrm{d}\Gamma}{\mathrm{d}E}(m_{\bar{\nu}_\mathrm{e}}) + \sin^2\theta \, \frac{\mathrm{d}\Gamma}{\mathrm{d}E}(m_\mathrm{s}), \tag{2.3}$$

with the effective mass of the active neutrinos $m_{\bar{\nu}_\mathrm{e}}$, the mass of the sterile neutrino m_s, and the sterile mixing amplitude $\sin^2\theta$ (Mertens et al., 2019). The effect of the coupling on the tritium β-spectrum is depicted in Figure 2.5, in which an arbitrary sterile mass of 10 keV and an unphysically large mixing amplitude of 0.2 were chosen for illustration. In the mixing case, two branches are visible: the decay into the known active neutrinos (orange), and an additional sterile branch emerging up to an energy of $E_0 - m_\mathrm{s}$. The superposition of both branches creates an energy spectrum with a kink-like signature due to the sterile neutrino (dashed blue curve) that needs to be detected. Theory does not

predict the position of such a kink, which means it could be located anywhere in the spectrum.

During KATRIN's commissioning phase, a first data set for the search of keV-scale sterile neutrinos was taken. An upper bound for the mixing amplitude of $\sin^2\theta < 5 \cdot 10^{-4}$ (95% C.L.) at a sterile mass of 0.3 keV was found, which already improved the limits from laboratory experiments in the mass range from 0.1 to 1 keV at the time (Aker et al., 2023). After concluding KATRIN's active neutrino mass campaign in the end of 2025, a dedicated measurement phase to survey the tritium spectrum for signatures of keV sterile neutrinos will be initiated. The enabler of this endeavour is the new TRISTAN detector, which will replace the FPD. It consists of an array of silicon drift detectors (SDDs), which can measure rates of up to 10^8 electrons per second with a resolution of < 300 eV (Mertens et al., 2019; Siegmann et al., 2024). With these properties, it will be possible to differentially measure the majority of the tritium β-spectrum with high sensitivity and cover a large parameter space of the sterile neutrino (Mertens et al., 2015). To account for the higher rate during measurements deep below the endpoint, the column density is estimated to be set to 1% of the nominal value. The duration of the TRISTAN measurement campaign is planned to be two years, divided into two phases. During phase I, the measurements will be performed using the KATRIN setup without major hardware changes, apart from changing to the new detector system. In order to reach the target sensitivity for the mixing amplitude of 10^{-6}, and by that improving the current laboratory-based limits by two orders of magnitude (Mertens et al., 2019), understanding the measured spectrum will be of paramount importance. This includes meticulously studying known, but also newly introduced or expected systematic effects. A tool to do this is available with the TRModel (Descher, 2024).

For deep-spectrum measurements, the RW is foreseen to cause two systematic effects: surface activity known from KATRIN (subsection 2.2.3), and electron backscattering (subsection 3.2.2). Electron backscattering will emerge as a new effect, since they can deposit energy in the RW through inelastic scattering, while still appearing in the spectrum due to the increased region of interest. This effect is examined more closely in chapter 3. Individual strategies to mitigate both RW effects have already been identified. The RW activity can be efficiently reduced in-situ by performing a UV/ozone decontamination, which was already proven in KATRIN (Aker et al., 2024; Aker, 2025). To reduce electron backscattering on the RW, an option could be to replace it by one made of beryllium, which has an inherently lower backscattering probability. Such a major hardware change is only planned for phase II of the TRISTAN measurements, which means the golden RW will remain until then.

2.4 Goals of this work

In this thesis, the RW and its systematic effects for deep-spectrum measurements are the central topic. This includes studying them through the TRModel description, but also reducing the effects by exploring hardware-oriented possibilities. The following major objectives are identified.

1. Contributing to the spectral modelling with focus on the RW,
2. Exploring UV/ozone decontamination for an in-situ reduction of RW activity,
3. Developing a strategy to qualify alternative RW materials with reduced backscattering probability, and applying it to beryllium as the prime candidate to check its suitability.

The individual points are further elaborated in the following sections.

2.4.1 Providing input for the TRModel code to study RW effects

The TRModel is used as a tool to estimate the impact of individual systematic effects on the sensitivity to detect the signature of a sterile neutrino in the tritium β-spectrum. Each effect is implemented in the form of a response matrix, some of which are generated using external simulation tools; in case of the RW, Geant4. An update of the TRModel is planned, which requires new inputs. For the RW, new, improved backscattering matrices with extended energy ranges and up to 280 times the current statistics were specified. Since the simulations are time-consuming (in the order of months), this demands the development of a Geant4 code with increased computational efficiency to reach the statistics, while maintaining its accuracy. This code shall then be used to generate the new response matrices. In this context, the results are to be investigated for physical and numerical effects, as well as variations due to the choice of simulation input.

2.4.2 Further investigation of UV/ozone cleaning to reduce RW activity

From KATRIN operation, it is evident that the RW's surface activity can be reduced by performing a UV/ozone decontamination. However, it is not clear – also not from literature – whether the efficiency is achieved by the UV radiation, ozone, or their combination. Hence, the underlying mechanism shall be explored to potentially increase the decontamination efficiency even further, but also to enable its application to tritium-containing systems in general. Since ozone is highly reactive and thus unstable, its properties like production and lifetime, as well as equilibrium concentrations within a vacuum system are of special interest. A dedicated experimental setup with suitable analytical tools has to be conceptualised and commissioned. With the knowledge gained from this predecessor experiment, an existing setup within TLK is to be upgraded to be able to study the effect of ozone on the surface activity of tritiated samples.

2.4.3 Development of a qualification procedure for alternative RW materials to reduce backscattering

To reduce the limitations arising from electron backscattering off the golden KATRIN RW, alternative materials could be used. Since the RW, located inside the WGTS, is subject to special conditions, it has to fulfil additional requirements. Three key components were identified: tritium accumulation, resilience to UV/ozone, and decontamination. In

order to confirm or deny a material's suitability, a measurement routine around these three properties has to be developed. One of the candidates is beryllium, which initially is being considered purely because of its very low nuclear charge. Hence, the developed qualification strategy should be tested and applied to beryllium first. The questions to be addressed are how much tritium is accumulated by the beryllium surface, and if it is possible to remove it in a fashion similar to KATRIN. Both can be answered by exposing beryllium to gaseous tritium and ozone, respectively. At the end of this work, a qualification routine for any alternative RW material shall be available.

Chapter 3

Rear Wall simulations for TRISTAN measurements using Geant4

To successfully identify potential ppm-level deviations in the tritium β-spectrum due to a sterile neutrino, it is required to model the anticipated spectrum to the same accuracy. This includes precise knowledge of each systematic effect that might play a role for measurements deep into the spectrum. The Rear Wall (RW) is of special importance, since it evokes electron backscattering from its surface, which is presumably the largest systematic effect (Descher, 2024). With the TRModel code, it is possible to model the differential β-spectrum and estimate the impact of different systematics on the sensitivity for a sterile neutrino. A short introduction on how systematic effects are treated in the TRModel is given in section 3.1. For an upcoming update, new RW inputs in the form of response matrices were required to enable a more accurate description of the entire spectrum. These matrices were generated using Geant4, which is described in section 3.2, together with their implementation in the TRModel to investigate backscattering from the RW and RW activity. section 3.3 presents a thorough examination of the energy spectra of the backscattered electrons in the improved response matrices, with a special emphasis on effects that cause narrow spectral features. Variations of the simulation output is discussed in section 3.4, followed by a conclusion in section 3.5.

3.1 Studies on systematic effects using TRModel

Searching the tritium β-spectrum for ppm-level signatures of sterile keV-scale neutrinos requires a thorough understanding of systematic effects. Table 3.1 lists all the systematic effects that are expected to be of relevance for differential measurements deep into the spectrum. Within the scope of this work, the systematic effects originating from the RW, namely electron backscattering and surface activity, are the focus. For a description of all

Table 3.1: Systematic effects relevant for deep spectrum measurements, according to Descher (2024). The RW effects, marked in red, are central to this work.

Category	Systematic effect
Tritium decay	Atomic corrections
	Final state distribution
Source	T_2 scattering
	Magnetic traps
	Plasma potential
Rear Wall	Backscattering
	Tritium decays
Transport and spectrometer	Magnetic reflection
	Magnetic collimation
	Synchrotron energy loss
	Transmission function
	Adiabaticity
	Post acceleration
Detector	Backreflection
	Energy deposition
	Charge sharing
	Fano noise
Background	Energy spectrum
Readout	Pileup
	Electronic noise
	Detection threshold
	Dead time
	ADC-nonlinearity
	Energy calibration

the effects, see Descher (2024). To investigate nearly all of the effects from Table 3.1, the TRModel code is a suitable tool.

The TRModel, developed by Descher (2024), calculates the differential β-spectrum of electrons that is foreseen to be measured with the future Tritium Investigation on Sterile to Active Neutrino Mixing (TRISTAN) detector. It is used within the Karlsruhe Tritium Neutrino (KATRIN) collaboration to study systematic effects relevant for deep spectrum measurements and their impact on its sensitivity to the mixing angle and mass of keV-scale sterile neutrinos. In the TRModel, the spectrum is not calculated on the single electron level, but described by the electrons' binned energy distribution $\vec{S}_{\text{in}}$ – initially the β-distribution from tritium decay. A systematic effect is treated as a response matrix R_1 that contains information on how it changes the distribution. By applying the response via matrix multiplication to the energy distribution according to

$$\vec{S}_{\text{out}} = R_1 \, \vec{S}_{\text{in}}, \tag{3.1}$$

a new distribution $\vec{S}_{\text{out}}$ is obtained that represents the energy spectrum altered by the systematic effect (Descher, 2024). In case multiple systematics are relevant, the total response is the product of the individual matrices:

$$R = R_N \times R_{N-1} \times ... \times R_1. \tag{3.2}$$

One decisive advantage of the response matrix formalism is the performance with which the spectra are computed: Since it is sufficient to calculate most of these once and store them in a database, they are simply accessed when needed for the computation. Some of the response matrices are created using external simulation software. Both RW activity and electron backscattering can be described by the same response matrix, which is generated using Geant4 (Agostinelli et al., 2003; Allison et al., 2006, 2016). For an updated version of the TRModel, a new, improved set of response matrices were required, which were produced within the scope of this work. Before going into detail on the new matrices, a brief introduction to Geant4 and how its output is used for RW activity and electron backscattering is given in the next section.

3.2 Modelling of systematic RW effects with Geant4

Similar to the current response matrices, the new ones were produced with Geant4. Geant4 is a software toolkit based on a Monte Carlo approach to simulate particles interacting with and propagating through matter (Agostinelli et al., 2003; Allison et al., 2006, 2016). Developed at CERN, it is used in a variety of research fields aside from high-energy physics, and is also suitable to use in this study due to its high versatility. Before describing the simulation setup with which the new RW response matrices were created, it is required to introduce some of the commonly used terminology in Geant4. For a detailed description on Geant4, see *Geant4 User's Guide for Toolkit Developers*[1] and *Geant4 Physics Reference Manual*[2].

- **World volume:** The world volume is the entire simulation domain and contains all other volumes. Any particle leaving this volume will be terminated.
- **G4_galactic:** Since it is not possible in Geant4 to simulate a perfect vacuum with zero pressure, an alternative material, G4_galactic, needs to be defined by the user. It consists of gaseous hydrogen with density $10^{-25}\,\text{g/cm}^3$, pressure $10^{-19}\,\text{Pa}$ and temperature 0.1 K.
- **Run:** Starting the simulation begins a run, which entails emitting a number of particles, tracking their interactions and terminating them once certain criteria are met. A run is typically started using a "macro" file, in which certain settings and

[1] https://geant4-userdoc.web.cern.ch/UsersGuides/ForToolkitDeveloper/BackupVersions/V10.7/fo/BookForToolkitDevelopers.pdf

[2] https://geant4-userdoc.web.cern.ch/UsersGuides/PhysicsReferenceManual/BackupVersions/V10.7/fo/PhysicsReferenceManual.pdf

boundary conditions are defined. Such a macro file is included in Appendix A. At the end of a run, the desired physical information can be stored to a file.

- **Primary and secondary particles:** Primary particles are initially emitted according to user input. Through interactions with matter, they can generate secondary particles, e.g. by ionisation, which possess lower energies than their parent particles. Since these carry a computation-internal identifier, they can be distinguished from primary particles to be saved separately.

- **Production cut:** To improve the CPU performance of a run, it is possible to define production cuts, which lead to a threshold energy for secondary particle production. Above this cut, particles propagating through matter lose energy in a discrete manner by producing secondaries. Below it, continuous energy loss is modelled instead and no secondary particles are generated (Sternheimer, 1952; Sternheimer et al., 1984; Salvat et al., 2001; Apostolakis et al., 2009). Setting this cut too high can have detrimental effects on accuracy by increasing the dependency on models.

- **Physics list:** A physics list is a collection of models with which the underlying physical processes are described. A multitude of these physics lists are available. In this study, the Penelope (Salvat et al., 2001) and Single Scattering physics lists are used due to their suitability for low energies and their level of detail. They include electromagnetic processes such as Coulomb scattering, ionisation, bremsstrahlung, and atomic de-excitation through Auger electron and characteristic X-ray generation. While Penelope models multiple scattering (Ivanchenko et al., 2010), Single Scattering calculates every scattering event explicitly, which leads to it being slower, but potentially more accurate. All physics lists are documented in the *Geant4 Guide For Physics Lists*[3] .

3.2.1 Simulation setup using the Geant4 toolkit

For the simulations performed in this study, Geant4 version 10.7.2 (June 2021) was used, which was the latest version at the beginning of this project. A more up-to-date version towards the end of this work (11.2.0, December 2023) revealed no significant differences in the results.

Figure 3.1a illustrates the simulation setup. A box made of G4_galactic – effectively vacuum – was chosen as the world volume, hence, particles can propagate it without significant energy loss. Contained in the world volume is a cylindrical absorber that represents the RW. Within the simulation, the RW surface is considered to be an ideal, perfectly flat surface; surface roughness is not taken into account. The RW material can be freely selected before the start of each run. In this example, electrons, represented by the red traces, are emitted from the world volume's center in a cone shape towards the RW. Figure 3.1b showcases the geometry defined in this study. The electron's pitch

[3] https://geant4-userdoc.web.cern.ch/UsersGuides/PhysicsListGuide/BackupVersions/V10.7/fo/PhysicsListGuide.pdf

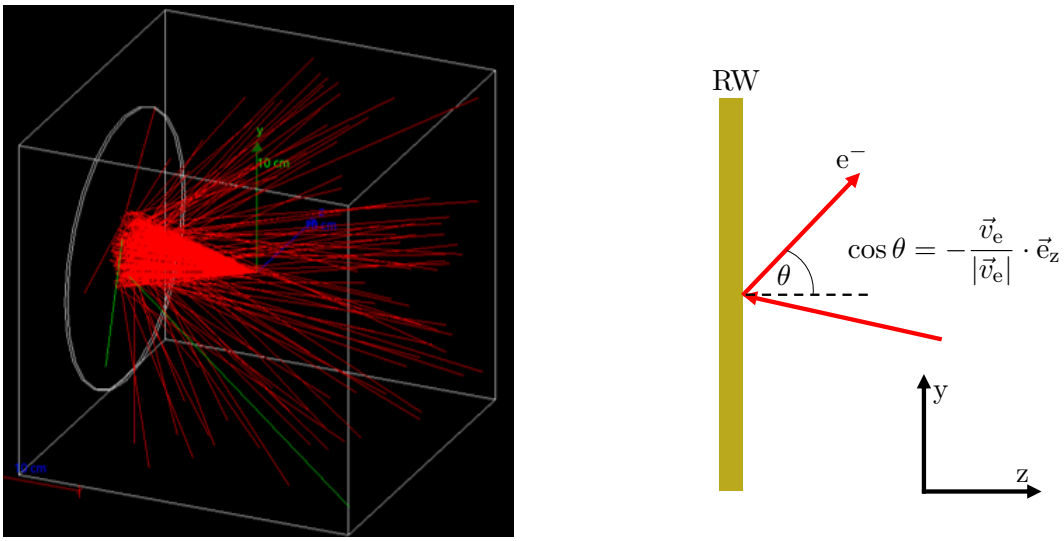

(a) Simulation setup

(b) Definition of geometry

Figure 3.1: (a): World volume containing the RW. The incident and backscattered electrons are displayed as the red tracks. Photons, e.g. in the form of bremsstrahlung, are visible in green. (b): Definition of the pitch angle θ with respect to the RW surface normal in the geometry.

angle θ relative to the beam axis takes values such that $\cos\theta = (+) - 1$ if its velocity vector $\vec{v}_e$ is (anti-)parallel to the RW surface normal. An electron is considered to have backscattered if at the instance of its termination it is outside the RW volume and its velocity vector fulfils $\cos\theta < 0$. Secondary electrons which satisfy this condition are also included. Even from this exemplary run shown in Figure 3.1a, the significance of electron backscattering is evident. Although the magnetic field strength at the RW is 1.26 T at nominal KATRIN settings, and 0.12 T during TRISTAN phase II measurements, it is neglected in the simulation, as it is irrelevant for the length scale of $\mathcal{O}(10\,\text{nm})$ at which electron scattering processes occur. Generally, an arbitrary number of primary electrons can be emitted from any location within the world volume, with user-defined energy and angle distributions. In order to simulate electrons with shallow angles of incidence, they are emitted directly at the RW surface.

The electron energies and angles are stored as histograms with 1300 bins, ranging from $(0 - 32.5)$ keV, and 100 bins from $\cos\theta = (-1 - 0)$, respectively. This choice is the refined binning for the new response matrices. Unless otherwise stated, the Penelope physics list is used for the shown simulation results throughout this chapter. However, both the old and the new RW response matrices are also available using the Single Scattering physics list. Since Penelope and Single Scattering feature independent descriptions of physics, their availability facilitates an estimation on how large the variations of the Geant4 simulations are expected to be.

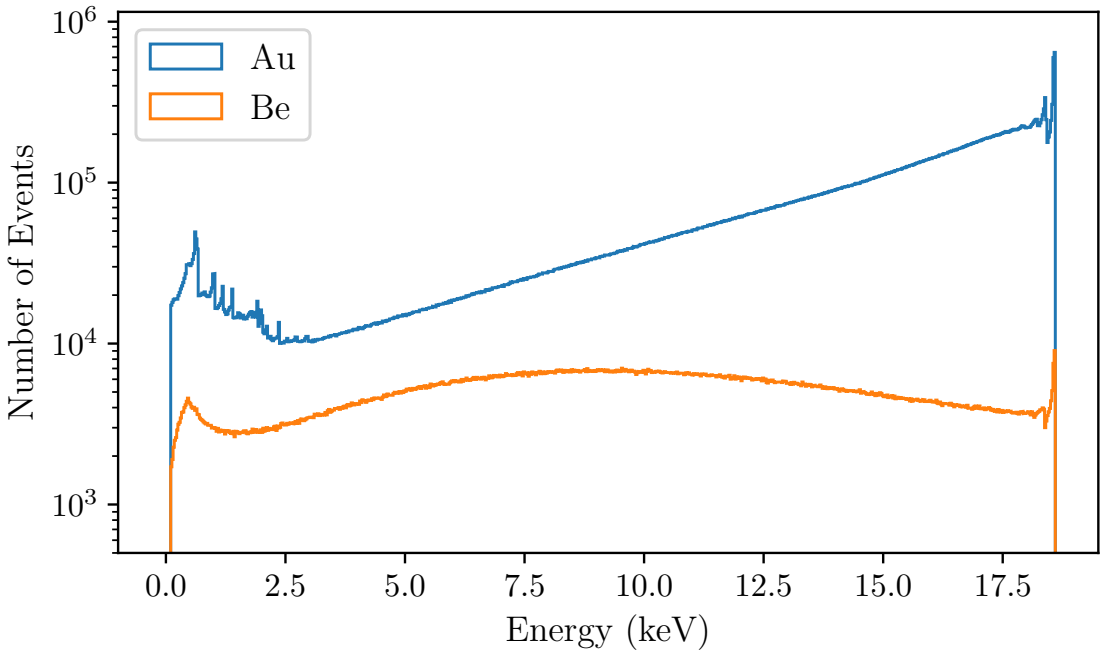

Figure 3.2: Energy spectrum of electrons backscattered on gold (blue) and beryllium (orange) with initial energies between (18.575 and 18.600) keV and angles of incidence from (0 to 8.1)°.

3.2.2 Electron backscattering from the RW

Figure 3.2 shows the energy spectra of backscattered electrons from gold (blue) and beryllium (orange). Initially, 10^8 electrons were emitted with energies of (18.575 – 18.600) keV, hitting the surface at angles from (0 – 8.1)°. The energies were sampled from a uniform distribution with the given limits. For the angles θ, a uniform distribution of $\cos\theta$ was used to reflect the isotropy of β-decay. These energy and angle ranges were chosen to study the simulation results, since they are representative for the new RW response matrices.

The greatest difference between the backscattering spectra from gold and beryllium is the overall number of electrons. For gold, 48.3% of the emitted electrons are either backscattered primaries, or secondary electrons propagating in downstream direction, while for beryllium, it is only 3.7% for these impact parameters. The elastic backscattering peak is constituted of $6 \cdot 10^{-3}$ and $9 \cdot 10^{-5}$, respectively, of the impinging electrons. At energies slightly below the elastic peak, oscillations resembling plasmon excitations are apparent. The Penelope physics list is the only list in which plasmons are implemented, and these structures are not seen when using the Single Scattering list. In this semi-logarithmic diagram, the backscattered spectrum for gold has a linear, positive slope from 3 keV to the very high-energy region, while beryllium shows a curvature with a local maximum at around 9 keV. The energy at which it emerges correlates to the nuclear charge

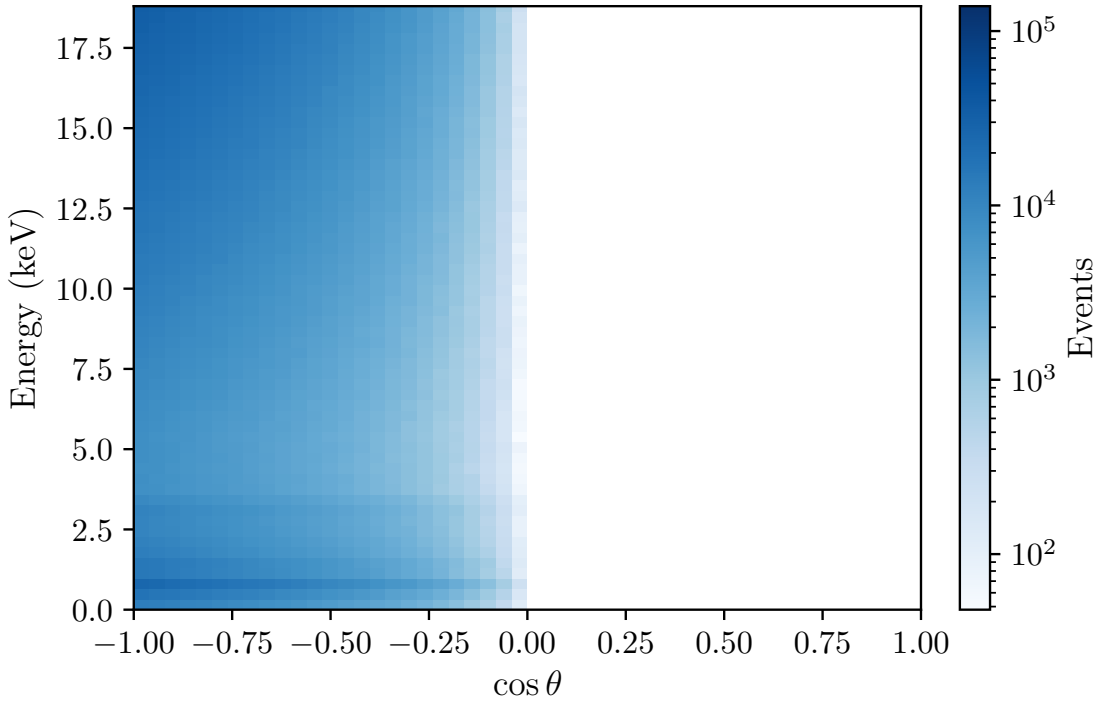

Figure 3.3: Post-scattering energy and angle distribution of 10^8 electrons with initial energies between (18.575 and 18.600) keV, hitting a gold surface at angles from (0 to 8.1)°.

of the absorber material, with lower Z leading to shifts towards lower energy. For both gold and beryllium, energies below 3 keV are dominated by secondary electrons. Due to the more complicated atomic structure of gold, discrete peaks from Auger electrons are present.

For a full physics description, the angular distributions are also of interest. The four-dimensional RW response matrices are a collection of two-dimensional energy and angular distributions of the backscattered electrons for any given input energy and angle combination. One of the components of such a matrix is shown in Figure 3.3, which displays the post-scattering energy and angular distributions of electrons with initial energies of (18.575 – 18.600) keV and angle of incidence of (0 – 8.1)° on the RW. From the number of initial electrons, the probability distribution for a single emitted electron to possess any energy and angle combination after backscattering can be calculated. By definition, the backscattered electrons only populate the half-space of $\cos\theta < 0$.

Figure 3.4 shows the expected energy spectra including all systematic effects, calculated with the TRModel using the old set of response matrices. Additionally, it gives a demonstration of why backscattering from the RW is critical[4]. During the first phase of

[4]Master's thesis by Kerstin Trost, "Mitigation of Rear Wall Backscattering in keV Sterile Neutrino Search at the KATRIN Experiment", ETP, 2024

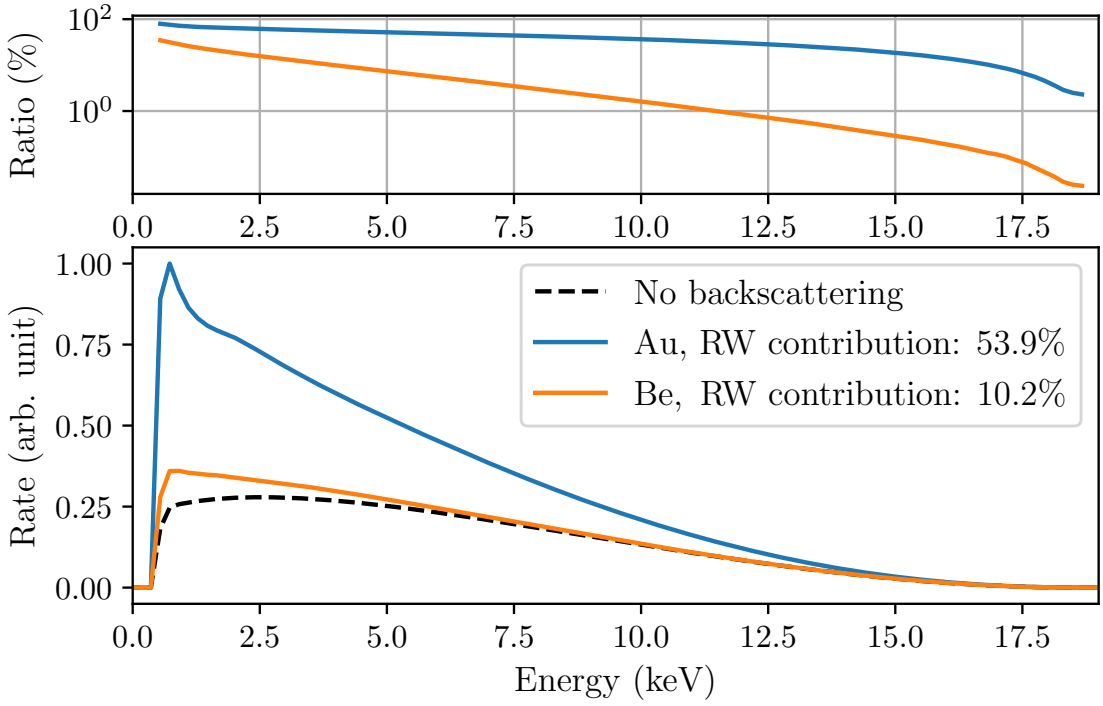

Figure 3.4: Differential energy spectrum reaching the TRISTAN detector under nominal KATRIN conditions, with and without scattering on the RW. The blue spectrum highlights backscattering from gold, where 54% of the total electrons have interacted with the RW. In case of beryllium, shown as the orange curve, a reduction to 10% seems possible. Data kindly provided by K. Trost.

the measurements with the current golden RW, due to its high nuclear charge, 54% of the detected electrons have interacted with the RW (blue curve). Since backscattering can also occur at the detector or at steep magnetic field gradients, multiply scattered electrons are present. These electrons distort the spectral shape significantly, with the highest impact towards lower energies. One of the possibilities to mitigate this effect, and the one which is the focus of this work (chapter 5), is replacing the current RW by one made of beryllium. By this, the contribution of electrons backscattered from the RW relative to the total number of detected electrons could be reduced to around 10% (orange spectrum in Figure 3.4).

3.2.3 RW activity as a systematic effect modelled from backscattering response

From the RW backscattering response matrices, it is also possible to model the spectrum of tritium decays of molecules adsorbed on the RW. Isotropically emitting electrons with energies following the tritium β-distribution directly from the RW surface instead of the

entire length of the windowless gaseous tritium source (WGTS) effectively creates a RW spectrum. Figure 3.5 displays the modelled RW spectra originating from surface-bound tritium on the RW for gold (a) and beryllium (b). The input spectrum in blue contains all electrons, emitted over the full solid angle, while the grey curve considers only the electrons emitted downstream. This spectral component is superimposed by the backscattered electrons, that were initially emitted upstream towards the RW surface. The resulting spectrum, shown in orange, shows the energy distribution of electrons leaving the RW surface, which is distorted due to backscattering.

In case of a beryllium RW, the spectrum consists of 20% fewer electrons overall. Another advantage of beryllium over gold can be seen in the low-energy region of the spectrum. Due to scattering events of electrons with gold, four discontinuous, unphysical peaks at energies of 0.61, 1.01, 1.18 and 1.38 keV are visible in the spectra simulated with the Penelope physics list. These originate from the internal model description of scattering. When using beryllium, another numerical artefact related to cuts arises at 450 eV. Both of these effects are explained in more detail in section 3.3. With the simulation setup presented here, it is in principle also possible to simulate tritium decays beneath the surface. Appendix B displays electron energy spectra generated by β-decay from different depths below the surface. However, sub-surface tritium is not expected to play a role, as indicated by the efficiency of UV/ozone cleaning, which removes only surface-bound tritium (Aker et al., 2024; Aker, 2025). For the spectra modelled from the backscattering response, the influence of a final state distribution (FSD) (Aker et al., 2021b) – the energy transfer from the β-electron to the daughter nucleus during decay – is not included, since the induced energy shift of $\mathcal{O}(1\,\mathrm{eV})$ is negligible compared to the foreseen detector resolution of $\mathcal{O}(100\,\mathrm{eV})$ (Mertens et al., 2019).

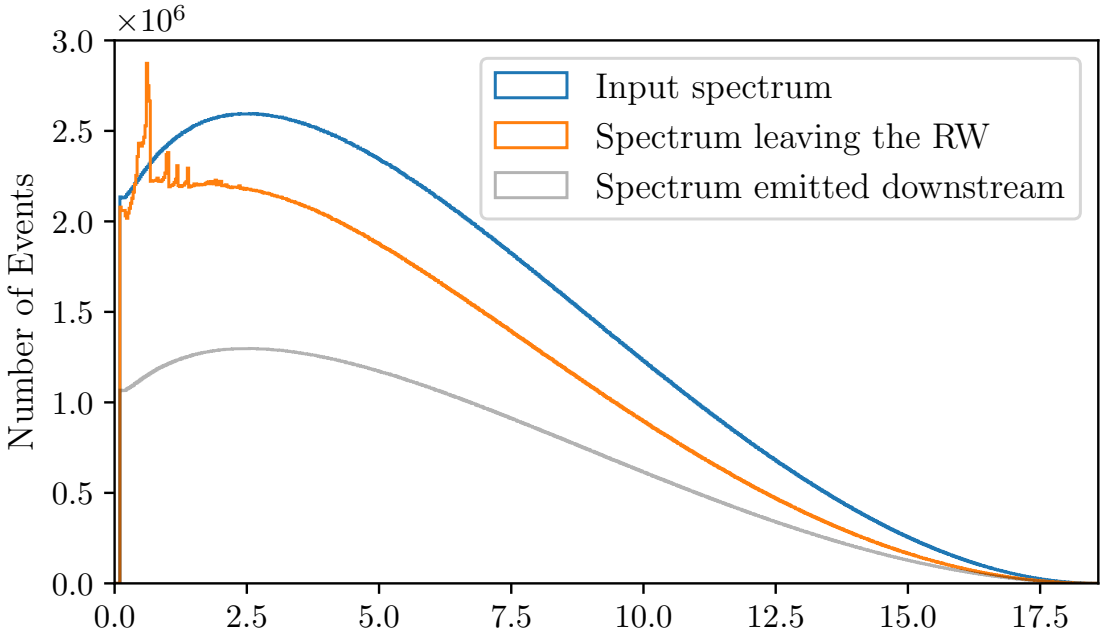

(a) Gold

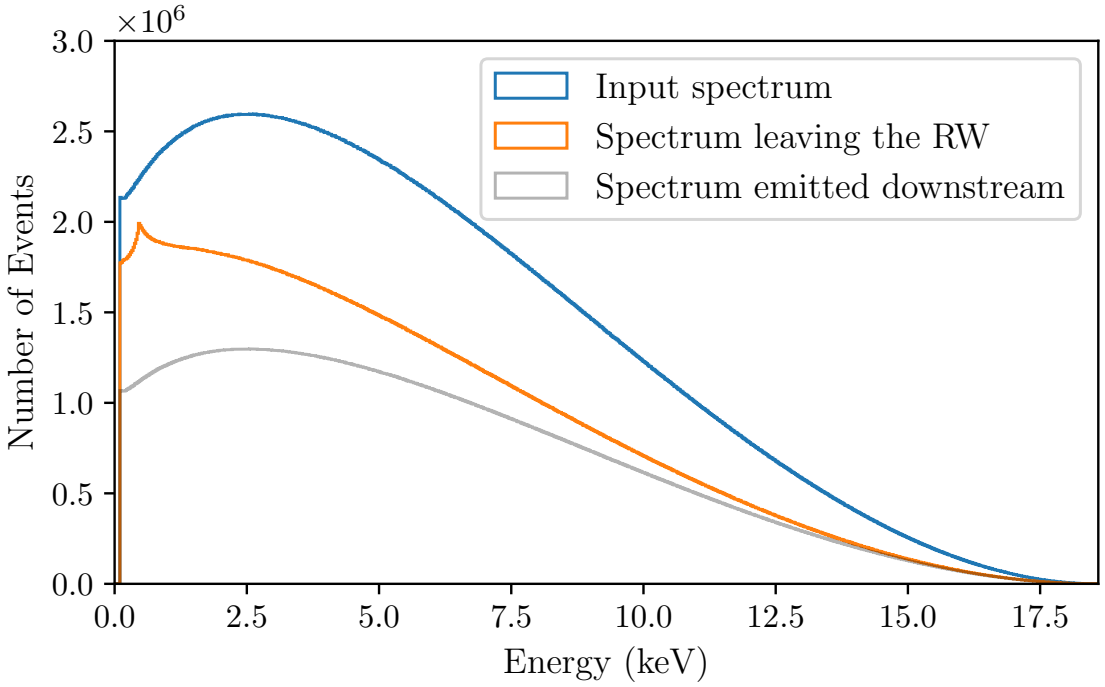

(b) Beryllium

Figure 3.5: RW spectra for gold (a) and beryllium (b) generated from backscattering simulations. Blue: elastic scatterings only, grey: absorption at the RW only, orange: spectrum including inelastic scattering.

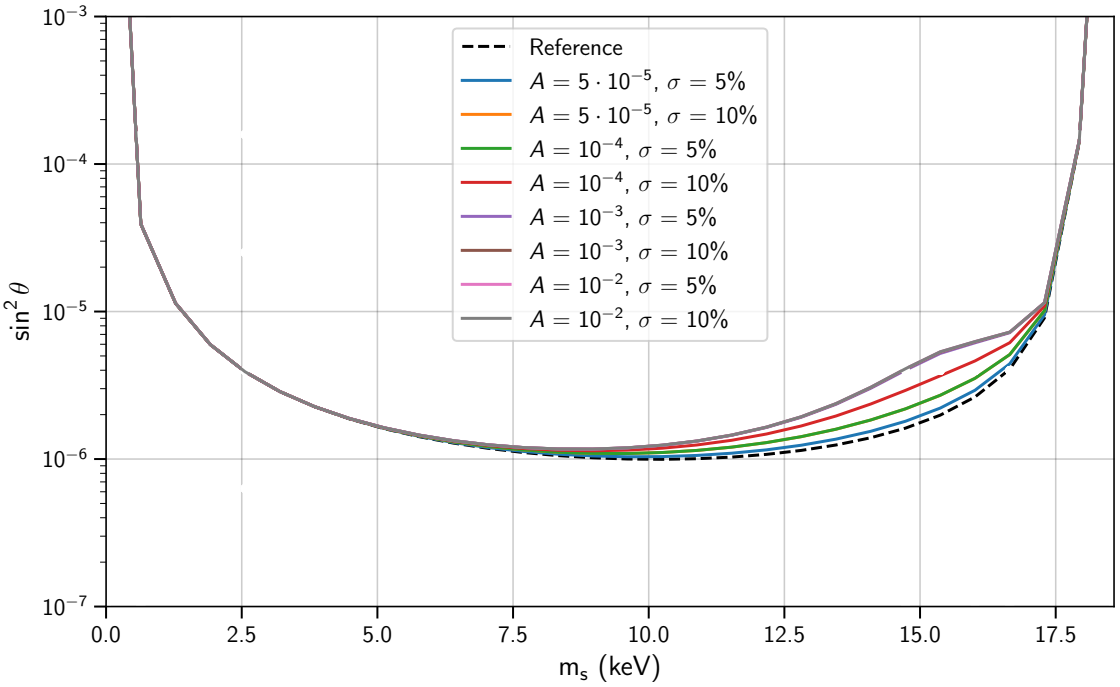

Figure 3.6: Sensitivity study on RW activity for beryllium and optimised magnetic field settings and one of the current RW response matrices.

Sensitivity studies were originally performed using a covariance matrix approach with correlated uncertainties (Descher, 2024), which is also employed in the scope of this work. Figure 3.6 shows the result of such a study on RW activity. Both the total activity on the RW surface, given in units of source activity A, and its relative uncertainty σ were varied. This case assumes a beryllium RW with optimised magnetic field settings, consistent with TRISTAN phase II parameters. As the accumulated activity increases starting at $5 \cdot 10^{-5}$, sensitivity on the mixing angle for sterile masses above 7 keV decreases, until an upper limit at 10^{-3} is reached. Above this threshold, additional activity does not seem to influence the sensitivity. As of now, it is unclear whether this behaviour is a physical effect that could be expected experimentally, or if it is a caveat of the method used to determine the sensitivity loss. One possibility for this observation's origin might be an insufficient number of electrons simulated for the production of the RW response matrices, which leads to too large statistical fluctuations in the matrices, and ultimately to a bias. To eliminate this possibility, improved sets of RW response matrices with more statistics, finer binning and extended energy ranges were produced, which is thoroughly described in the following section.

Table 3.2: Comparison of the old and new RW response matrices

Parameter	Old response matrices	New response matrices
RW materials	Au, Be	Au, Be, stainless steel
Physics lists	Penelope, Single Scattering	Penelope, Single Scattering
Statistics	$2.5 \cdot 10^{10}$ (Au), $2.5 \cdot 10^{9}$ (Be)	$7 \cdot 10^{11}$ (Penelope), 10^{11} (SS)
Energy range	$(0.1 - 18.6)$ keV	$(0 - 32.5)$ keV
Energy bins	100	1300
Angle range ($\cos\theta$)	-1 – 0	-1 – 0
Angle bins	25	100
Production cut	100 eV	100 eV
Tracking cut	–	450 eV

3.3 Improvements over previous RW response

The new set of response matrices needed to fulfil three given key requirements: more statistics, finer binning, and an extended energy range. Table 3.2 lists important parameters for the generation of the new RW matrices and compares them to those of the old data set.

A higher maximum energy of 32.5 keV was chosen to be able to study source-related systematic effects using krypton (Vénos et al., 2018; Marsteller et al., 2022; Acharya et al., 2025). The latter two requirements are easily met by adjusting the histogram in which the data is stored, and emitting primary electrons with higher energies, respectively. The backscattered spectra for gold and beryllium with the new maximum energy of 32.5 keV with the appropriate binning is displayed in Figure 3.7. Qualitatively, their shape is similar to the spectra from electrons with lower energies, and the backscattering probabilities of 3.7% and 48% for beryllium and gold, respectively, are also not significantly different compared to the 18.6 keV case.

Increasing the statistics poses a greater challenge due to the computation time it takes to complete the calculations. For the response matrices made with the Single Scattering and the Penelope physics lists, 10^{11} and $7{\cdot}10^{11}$ initially emitted electrons, respectively, were desired. For beryllium this corresponds to up to 280 times the statistics of the available matrices. A higher number of electrons was chosen for Penelope, since it is inherently faster by a factor of about seven than Single Scattering at tritium decay energies. With this in mind, the simulation setup had to be made more efficient, while simultaneously maintaining its accuracy. One way of speeding up the computations is increasing the production cut for secondary particles, which is not preferred due to the heavier reliance on modelling for the continuous energy loss. Geant4 uses a cut of 990 eV by default; for the current response matrices, 100 eV was used instead. Its global impact on the backscattered spectrum from beryllium is demonstrated in Figure 3.8. The transition of energy loss from discrete emission of secondary particles to the modelled continuous regime is seen at the energies corresponding to the cuts. Below these, a rapid decrease of electrons occurs the lower the energy, because no new secondaries are created. To conserve energy, the

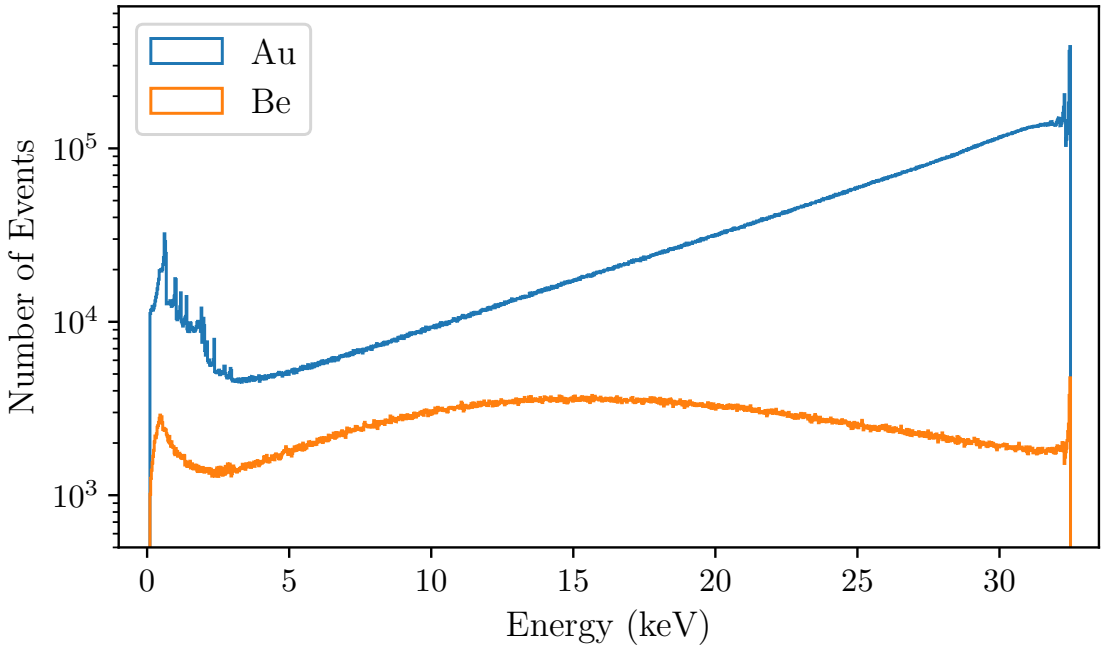

Figure 3.7: Energy spectra of electrons with initial energies of (32.475 – 32.500) keV, and angles of (0 – 8.1)° backscattered from gold and beryllium, including secondaries. For both gold and beryllium, the spectra do not differ qualitatively from backscattered spectra at lower energies.

surplus is instead contained in the high-energy primary electrons. Apart from the elastic scattering peak, for a cut of 990 eV there are consistently more electrons present in the backscattered spectrum at energies above 7 keV.

It is possible to circumvent the issue with the production cuts by choosing a hybrid approach: defining an additional "tracking cut", below which the secondary particles are generated, but neglected for further calculations. This resolves the energy balance by considering the theoretical cross sections of the discrete energy loss by secondary generation, and shifting the model-dependent, continuous description to energies as low as possible. Within Geant4, particles can be "killed", which essentially removes them from the simulation and forfeits their energy. By not further tracking low-energy secondary electrons, computation time is saved. Since the option for a tracking cut is not available by default, the source code had to be adjusted. At the beginning of a time step for each secondary particle, its energy is checked, and if it is below the value given by the tracking cut, it will be killed. For the response matrices, the production and tracking cuts are 100 and 450 eV, respectively, which means secondary particles with energies as low as 100 eV can be generated, but they will only be tracked as long as their energy is above 450 eV. An upper energy of 450 eV for secondary electrons is an appropriate choice, since it is expected to operate the main spectrometer at a voltage of 500 V for background suppression (Descher,

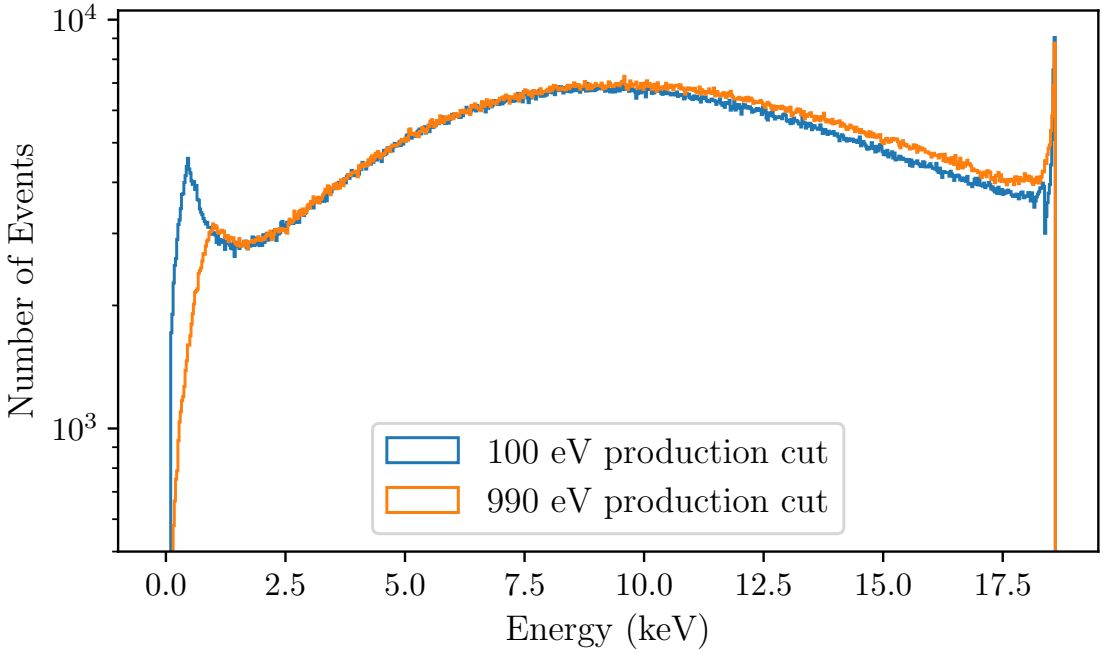

Figure 3.8: Energy spectra of electrons with input energies of (18.575 – 18.600) keV, and angles of (0 – 8.1)°, backscattered from beryllium with different production cuts. For the higher cut, low-energy secondaries are absent, but a higher number of primary electrons in the high-energy region are visible.

2024). Using this implementation, which can be activated or deactivated from the macro file, resulted in a speed-up of 24% for the simulations of gold using Penelope. For Single Scattering, however, the speed-up is a factor of 2.2 at 18.6 keV, due to its extensive use of explicit calculations.

To further optimise the statistics in view of the extended energy range up to 32.5 keV, weight factors of up to 600 on the number of the initially emitted electrons depending on the given energy and angle combination were applied. Increased weights were chosen for energies in the tritium β-spectrum and around the krypton lines, as well as for angles smaller than the main spectrometer's acceptance angle. The matrix containing all the weight factors is included in Appendix C. For each of the new RW response matrices, a combination of 130,000 energies and angles of the emitted electrons were simulated. The energy ranged from (0 – 32.5) keV, with 1300 bins (25 eV per bin) and 100 angle bins from $\cos\theta = 1$ to 0 (0.01 per bin). Within each bin, the electrons were sampled from a uniform distribution. The new RW response matrices are available for three different materials: gold, beryllium, and, as a reference, stainless steel. For each of them, a Penelope and a Single Scattering version were created. With the statistics increased by a factor of up to 280 per matrix, and a significantly finer energy binning, it is important to explore physical

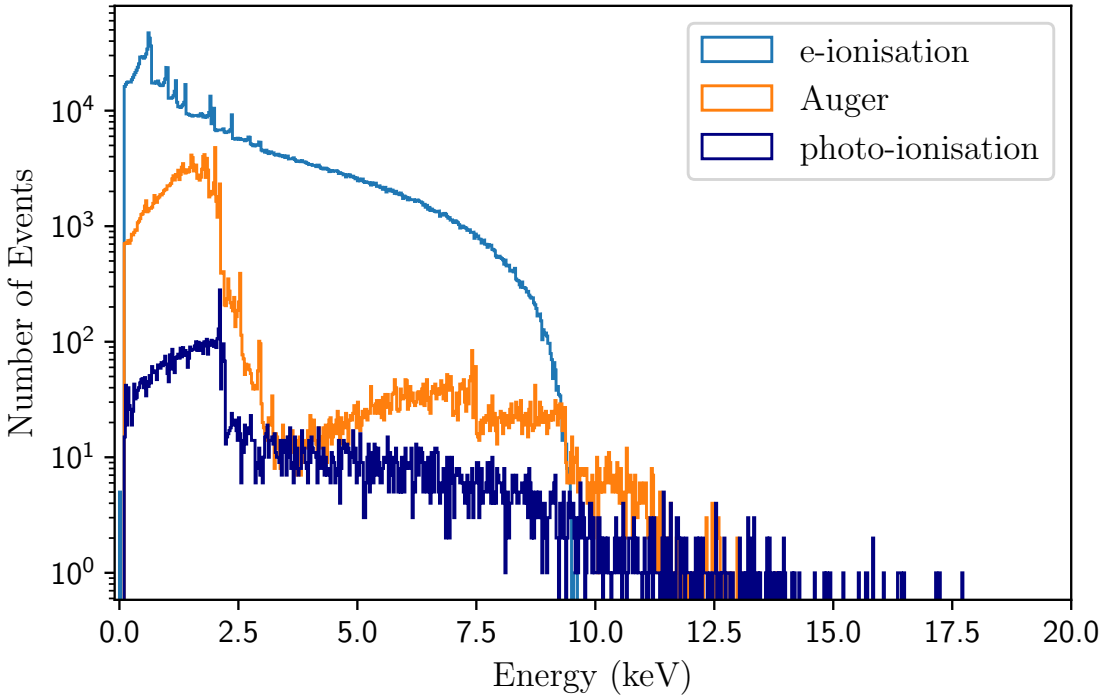

Figure 3.9: Distribution of secondary electrons originating from scattering of electrons with initial energies and angles of (18.575 – 18.600) keV and (0 – 8.1)°, respectively, on gold, divided into their generation process. Electrons resulting from impact ionisation are the most likely secondary particles.

and numerical effects which could potentially cause narrow features in the backscattered spectra.

3.3.1 Physical and computational effects in backscattered electron spectra

Figure 3.9 shows the energy spectrum of secondary electrons emitted downstream after scattering on gold, divided into their generating process. In the relevant energy range, three processes contribute to the generation of secondary electrons: impact ionisation, the Auger effect (Meitner, 1922; Auger, 1923), and photoionisation. Photoelectrons are the fewest number of secondaries. This is expected, since photoionisation is a second-order process that requires a photon, e.g. from bremsstrahlung. For beryllium, these are negligible due to its low nuclear charge. A more prominent population of electrons, which are present as narrow features in backscattering spectra, arises from the Auger effect. Although Auger electrons have discrete energies at the time of their creation, they lose energy when propagating through and escaping the material if they are generated below the RW surface. In Geant4, Auger transitions for elements with $Z < 5$, are not

considered, as there is no information available in the database used (Perkins et al., 1991). However, due to beryllium possessing only four electrons, there are only two possible energies for Auger electrons, which are both below 200 eV (Coghlan & Clausing, 1973). Hence, the absence of these electrons is not expected to have a considerable effect on the resulting spectra, since the main spectrometer voltage is expected to be set to 500 V (Descher, 2024). The largest contribution to secondary particles with 91% comes from electrons produced due to impact ionisation. Since both electrons are indistinguishable, at most half of the incident electron's kinetic energy can be transferred, which is why they do not produce electrons with energies above 9.3 keV. Geant4 considers the electron with more kinetic energy as the primary. Impact ionisation creates secondary electrons with a continuous energy distribution, since the result is a free electron. The simulated spectrum seems to partly disagree with this statement due to the presence of narrow peaks at around 3 keV and below. These are of numerical origin and stem from the way the Penelope physics list treats inelastic collisions using a Generalised Oscillation Strength model (Salvat et al., 2001). In this model, inelastic scattering is divided into close and distant parts, with distant excitations of an atomic shell being approximated by the emission of a secondary electron with exactly the resonance energy of the shell involved. In the Geant4 documentation it is reasoned that these peaks will be smoothed out after multiple interactions, however, this does not seem to be the case for gold due to its large backscattering probability.

These resonances are even more pronounced in the energy spectrum shown in Figure 3.10, for which a finer binning was used. At the low end, the solid black lines indicate the resonance energies of the M and N shells. Even though the approximation is implemented to directly affect secondary electrons, it has global consequences that are not restricted to lower energies. If primary electrons have a single interaction with the RW atoms before being backscattered and excite one of the shells, they will lose exactly that energy each time. This leads to an overpopulation of single-scattered primary electrons, which results in discontinuities at higher energies. With increasing bin size, these features start to disappear, which is why they may not be visible in the current set of response matrices. It has to be emphasised that this modelling approach is only used in the Penelope physics list and is irrelevant to Single Scattering. This phenomenon is also not a concern for beryllium in general. Now that the energy spectra of the backscattered electrons are understood, the variation of the results from the different physics lists and simulation parameters are examined.

3.4 Variations of Geant4 simulations

From the previous sections, it became obvious that identical simulations can produce significantly different results purely based on a few, albeit inconspicuous settings. This issue is further highlighted by also considering differences in physics lists.

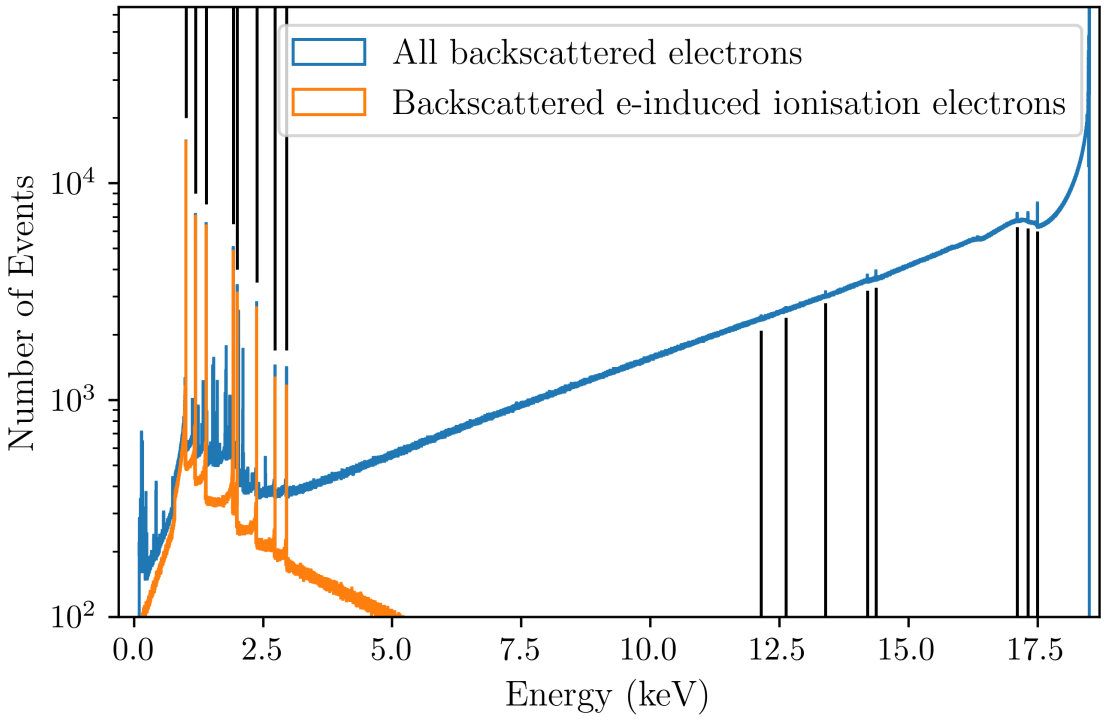

Figure 3.10: Unphysical peaks visible in the backscattered spectrum from gold including secondaries due to the modelling of impact ionisation. The solid lines mark the energies corresponding to the N and M shells, which also appear at high energies as energy loss from primary electrons.

3.4.1 Impact of physics list and simulation execution

Observations within this study hint towards differing default states of physical processes for different physics lists. While some processes are enabled for one list, they may be disabled for the other. Hence, it is crucial to explicitly set the desired state for each process every time a run is started to not rely on ambiguity.

For the backscattered spectra in Figure 3.11, the production of secondary particles was disabled for the orange curve. Disabling some of the processes effectively leads to a production cut of infinite energy, which is why the result is similar to too high cuts, but greater in magnitude. It is practically impossible for high-energy primary electrons to undergo, and therefore lose energy to, interactions that would produce secondary electrons. In consequence, more energy is retained in higher energies compared to the scenario where secondaries could be generated, as shown in Figure 3.11 (b). The overall shape is also different, with the plasmon-like structures disappearing completely for the case without secondaries. The largest difference in bin content is about 60% at an energy of around 18.4 keV. At the low-energy end of the spectrum (a), the lack of secondary electrons leads

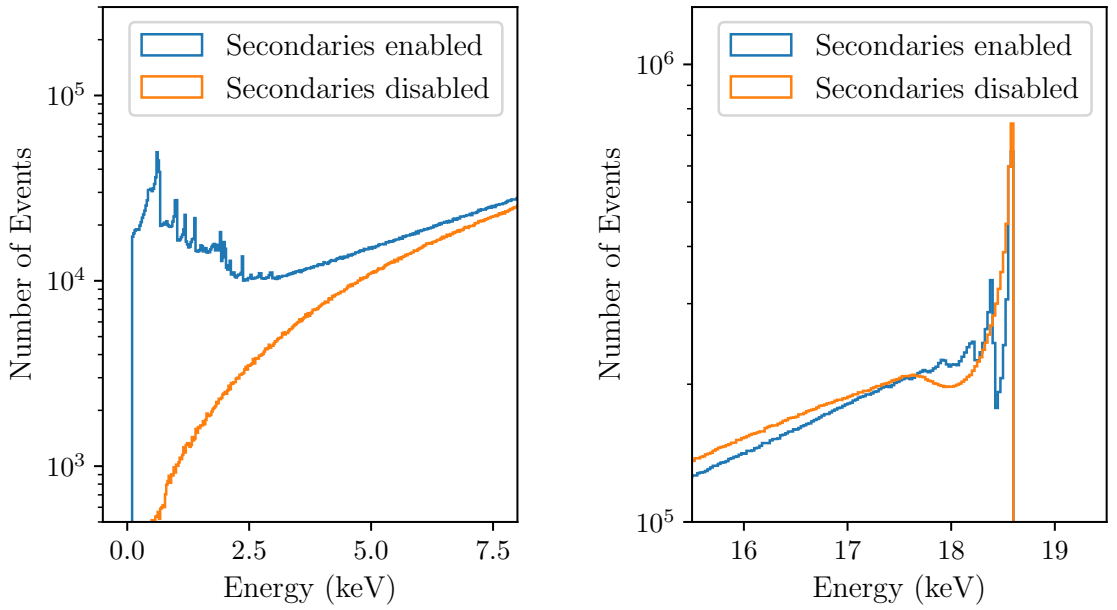

(a) Low-energy region

(b) High-energy region

Figure 3.11: Comparison of backscattered spectra from gold with and without production of secondary particles enabled, highlighting the low (a) and high-energy (b) region within the spectrum. The primary electrons initially possessed energies of (18.575 – 18.600) keV and angles ranging from (0 – 8.1)°.

to a smooth, fast decrease of particles with energies lower than around 5 keV. The overall number of electrons in the spectra is consistent within 3%.

Depending on which physics list is used for the simulations, a similar effect in magnitude can be expected. Figure 3.12 displays the energy spectra of electrons backscattered from gold produced with the Penelope (blue) and Single Scattering (orange) physics lists. Although the deviation of the high-energy region of Single Scattering is similar to the Penelope case with an increased production cut, their greatest difference is visible in the secondary electrons. Because Single Scattering explicitly calculates every single collision, more secondaries are created, whereas Penelope makes use of multiple scattering models that include energy loss implicitly. Due to its high nuclear charge, more than double the number of secondary electrons are present in the Single Scattering spectrum than for Penelope. In the case of beryllium, the numbers are comparable. In the intermediate energy range from (7 – 13.5) keV, the results of both physics lists are in agreement. From the backscattered spectra alone, it is unclear which of the physics lists produces the more accurate results. To get an impression on the overall agreement of Geant4 simulations in the low-energy range relevant to β-decay, literature is consulted.

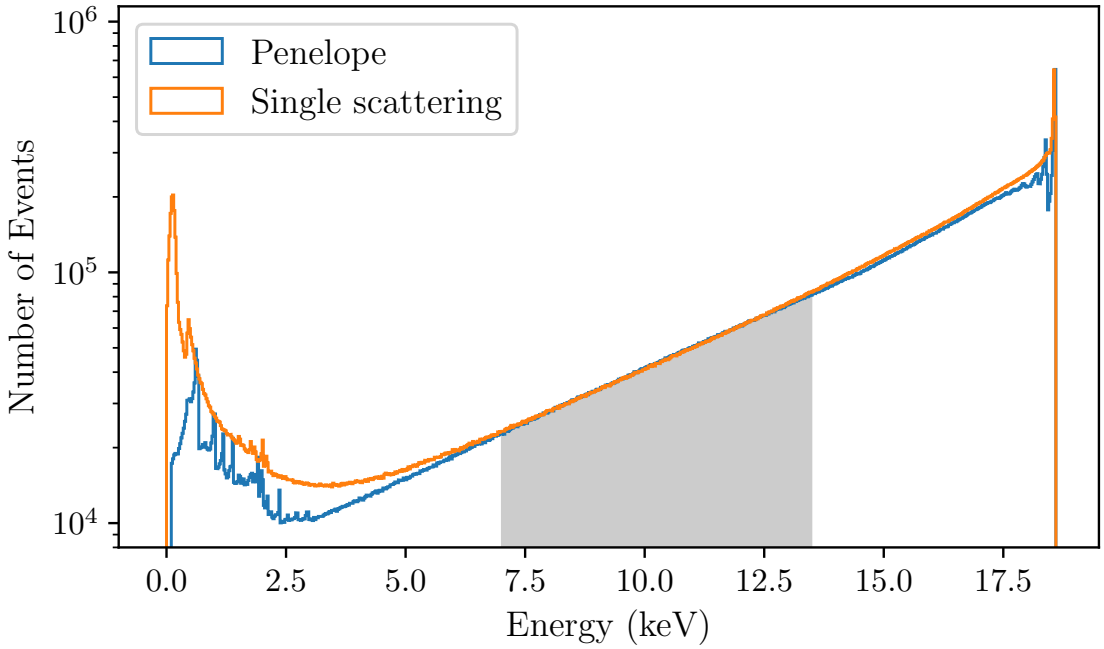

Figure 3.12: Comparison of backscattered spectra resulting from electrons with energies of (18.575 – 18.600) keV and angles of (0 – 8.1)° from gold, using the Penelope (blue) and Single Scattering (orange) physics lists. Within the shaded area, both spectra are in good agreement.

3.4.2 Comparison to experimental data

In the context of a previous KATRIN-related study, Huber (2021) compared the results of his Geant4 simulations of electron backscattering from the RW to experimental data. For the backscattering probability, a mean deviation of 6.3% between simulation and experiment (Hunger & Küchler, 1979) was found, and a larger weighted average deviation in the backscattered energy spectrum from silver of 19.6% (Darlington, 1975). These comparisons only paint an incomplete picture though, since many more experimental studies on electron backscattering probabilities were conducted in the past.

An extensive compilation of measured backscattering probabilities, together with comparisons to simulations using different versions of Geant4, is included in Kim et al. (2015). A similar, more recent study with agreeing conclusions was published by Dondero et al. (2018). Although newer versions of Geant4 are not included due to the age of the publications, they are still valid. In the study by Kim et al. (2015), the backscattering coefficient, defined as the ratio of backscattered electrons with energies above 50 eV to incoming ones, is treated as an indicator of the simulation accuracy. Multiple materials, including gold, were investigated in over 100 experimental datasets. Similar to the cases reviewed in the previous sections, the electrons hit the material surface perpendicularly in the experiments. Figure 3.13 shows one of their comparisons of multiple experimental datasets on

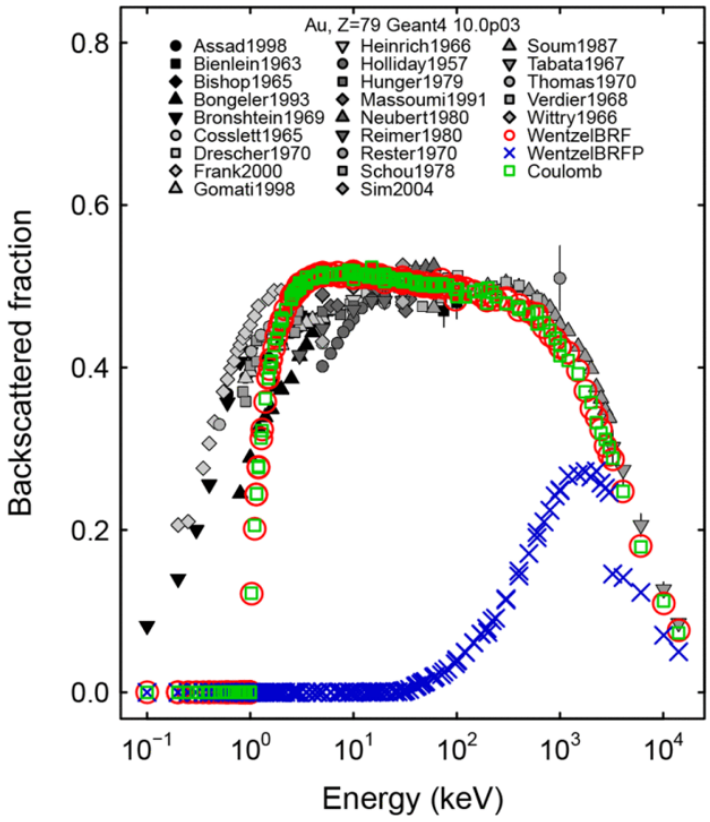

Figure 3.13: Comparison of the backscattered fraction of electrons from gold, including experimental results in the grey-scaled data points. Simulated results with different multiple scattering implementations are included as the coloured data points. Figure as published in Kim et al. (2015) under the CC BY 4.0 license https://creativecommons.org/licenses/by/4.0/.

the backscattering coefficient of gold with their simulations. The grey-scaled data points were obtained from experiments, and the coloured points indicate results from simulations using different multiple scattering algorithms. A wide energy range of $(10^{-1} - 10^{4})$ keV is available, which the authors divided into subsets; with the low-energy dataset containing energies from 1 keV to 20 keV. Kim et al. (2015) concluded that at the time of the study, the low-energy set could not be reproduced by the pre-defined physics lists, and that the simulated backscattering coefficients were mainly determined by the multiple scattering models used. This is evident from Figure 3.13, in which two of the three algorithms overestimate the backscattered fraction between 3 keV and 10 keV by up to 0.1, depending on the measurement. At higher energies, albeit irrelevant for the RW response above 32.5 keV, the simulations agree well with the experiments. The Penelope physics list uses a hybrid approach which employs Coulomb scattering, included in the figure as the green

squares. With the newer Geant4 version 10.7.2 used in this study, the simulations at very low energies ($< 1\,\mathrm{keV}$) can reproduce the experimental data.

The study by Kim et al. (2015) highlights the issue previously hinted at, however: the disagreement of the experimentally determined backscattering coefficients. The highest spread of around 0.2 is seen at an energy of 1 keV, decreasing to 0.1 at 7 keV. Since the fluctuations in the experiments are similar in magnitude as in the simulations due to the choice of physics list, it is impossible to identify a single dataset to compare the simulations to. Hence, to determine the accuracy of the available RW models, an in-situ characterisation and calibration of the electron backscattering on the RW is mandatory for TRISTAN measurements.

3.5 Conclusions

This chapter presented an overview on how the Geant4 simulations are used as input for the TRModel to study systematic RW effects for TRISTAN. Additionally, the production of new RW backscattering response matrices for gold and beryllium was documented. The most important findings from detailed analyses of the energy spectra of backscattered electrons are listed below.

1. Six new RW response matrices are available for use in an upcoming update of the TRModel code. These were produced with Geant4 for three materials: gold, beryllium and stainless steel, with the Penelope and Single Scattering physics lists each. It was possible to accelerate their calculation by adjusting the description of secondary electrons. Compared to the old matrices, these have finer binning, an extended energy range up to 32.5 keV to enable studies using krypton, and up to 280 times higher statistics, depending on the material and physics list.

2. The spectra simulated with the Penelope physics list experience narrow features due to numerical effects. With coarse binning, these are not necessarily visible. However, caution is advised when using the Penelope matrices to search for discrete deviations with small magnitude, e.g. the contribution of the sterile branch in the tritium β-spectrum. This issue does not arise for the Single Scattering RW response.

3. It was demonstrated that the initial settings, as well as the choice of physics list have a large impact on the backscattered spectra resulting from the simulation, with differences in the energy bin content of up to 60%. Benchmarking the simulation by including measurements is also not possible, since the measured backscattering coefficients experience large fluctuations as well. Therefore, an in-situ characterisation procedure of electron backscattering from the RW will need to be developed.

With the new response matrices, systematic RW effects, especially the activity on its surface, require to be revisited for an updated estimation on sensitivity loss. Ways to experimentally mitigate RW activity and backscattering are investigated in the next two chapters.

Chapter 4

Reduction of surface activity: UV/ozone decontamination

If the threshold for the acceptable Rear Wall (RW) contamination has been exceeded, an in-situ reduction will be necessary. The exact value has not been determined yet, but is subject to study in chapter 3. Previously, the decontamination was successfully performed multiple times with the ultra-violet (UV)/ozone cleaning method (Aker et al., 2024; Aker, 2025). To optimise this method, and to enable its application for a variety of systems, a deeper understanding is necessary. This includes the underlying mechanisms of UV based ozone production in a tritium-compatible vacuum system, its lifetime depending on the surface-area-to-volume ratio, and molecule number density in equilibrium (section 4.5). Additional factors such as carbon content on the surfaces are also of interest (subsection 4.5.2). For this task, the ultra-violet ozone (UVO) experiment was designed and commissioned, and its analytical systems for tritium-compatible ozone monitoring were calibrated (section 4.4). This chapter gives an overview of the current understanding of the UV/ozone decontamination method (section 4.3). Afterwards, the UVO experiment is presented (section 4.4) and the results on ozone properties like production, lifetime and equilibrium concentration are shown (section 4.5), which was already published in Batzler et al. (2024). In a follow-up study, the system was loaded with deuterium to test the hypothesis of adsorption on the surfaces, and deuterated hydrocarbons forming and desorbing under UV/ozone exposure. These were not detected, instead, the generation of D_2O prior to ozone measurements hinted towards oxidation of the vessel surfaces (section 4.7). Finally, the first successfully applied decontamination of a beryllium sample involving ozone in the absence of UV radiation is be discussed (section 4.8).

4.1 Observations from the KATRIN Rear Wall

The current working hypothesis based on in-situ RW activity measurements in the Karlsruhe Tritium Neutrino (KATRIN) experiment suggests that the tritium is bound to the RW in the form of tritiated amorphous carbon, which forms on the RW due to continuous

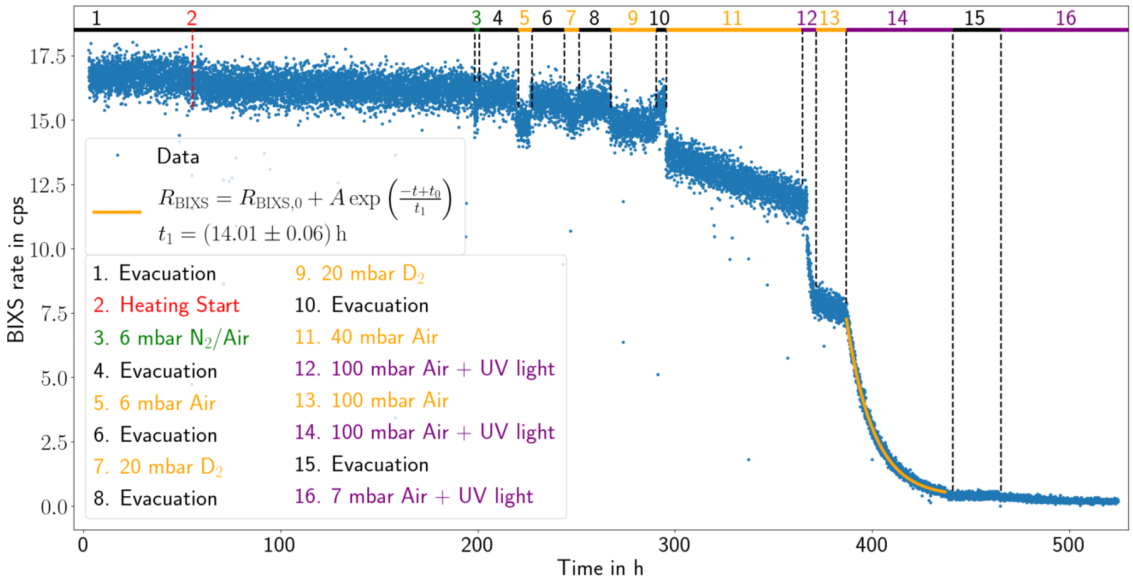

Figure 4.1: BIXS count rate, representing the visible activity, during the application of several in-situ decontamination techniques to the RW. Figure as published in Aker (2025) under the CC BY 4.0 license https://creativecommons.org/licenses/by/4.0/.

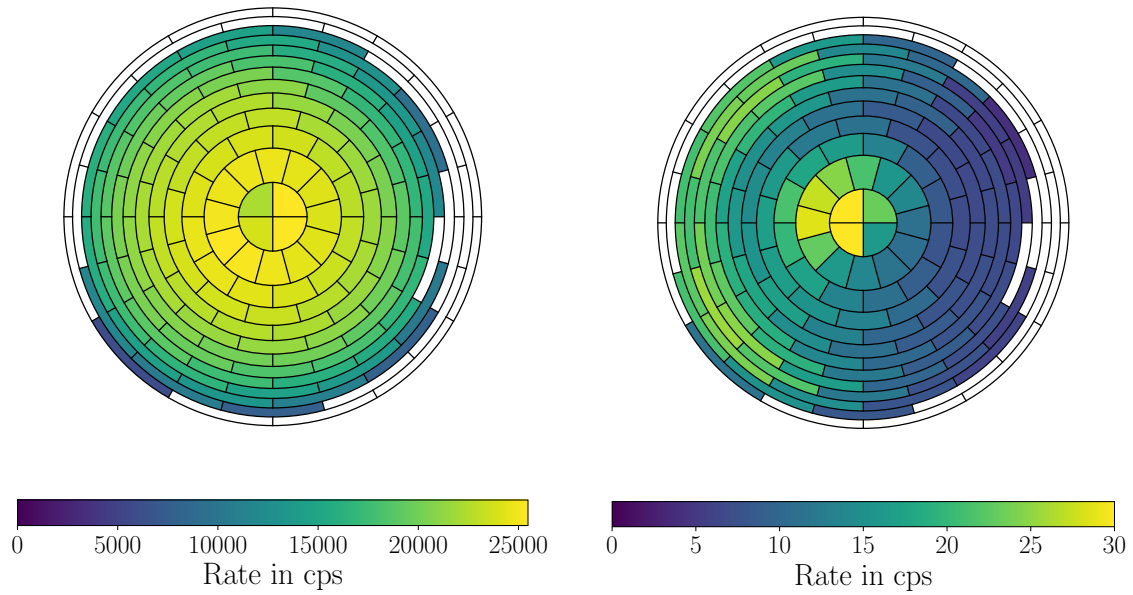

Figure 4.2: Observed count rate due to RW activity before (left) and after (right) the first UV/ozone decontamination. Data taken from Aker (2025).

bombardment with β-electrons (for a detailed description, see Aker (2025)). The goal of the first RW decontamination was to achieve the highest possible decontamination factor. In a systematic study, multiple in-situ decontamination methods were applied to the RW, shown in Figure 4.1. Continuously evacuating, baking out and purging the RW chamber did not lead to a significant reduction of surface activity. Introducing ambient air into the vacuum system induced a decrease in activity due to the residual humidity. However, irradiating 100 mbar of ambient air with UV light from a mercury lamp to form ozone drastically accelerated the process. Hence, UV/ozone cleaning proved to be the most efficient technique, yielding a decontamination factor of more than 1300. For the following two RW decontaminations, an 80:20 He/O_2 mixture at a pressure of 100 mbar was used with comparable performances. (Aker et al., 2024)

After the UV/ozone decontamination, the RW activity distribution was measured with KATRIN's focal plane detector (FPD) and displayed a dipole structure (Figure 4.2, right hand side). The detected spatial count rate transitioned from 4.203 ± 0.048 to (28.58 ± 0.13) cps, with the side facing the UV sources showing lower surface activity (Aker, 2025). The reason for this strong difference is not entirely understood. Possible explanations include gradients in either UV intensity due to absorption by the gas, or ozone concentration with increasing distance to the UV sources. Another open question is if there are pressures at which the decontamination is faster and/or more efficient than at the previously used pressure of 100 mbar. Finally, it is unclear whether the decontamination effect is purely caused by ozone, and if ozone exposure alone would be sufficient. To address these questions, an existing experimental setup closely related to the Tritium Adsorption Desorption Experiment (TRIADE) – which has already been utilised in the past to qualify the gold RW (Röllig, 2015) – is introduced.

4.2 Previous examinations with TRIADE

TRIADE was designed and commissioned to study tritium accumulation with sub-monolayer sensitivity by exposing surfaces to gasous tritium. The setup consists of a vessel containing the sample holder and a beryllium window to shield a silicon drift detector (SDD) from tritium contamination. Using beta-induced X-ray spectrometry (BIXS), the bremsstrahlung and characteristic X-rays generated by the tritium β-electrons interacting with matter can be related to near-surface activity. The sample holder and the recipient are coated with gold to increase the X-ray yield. Figure 4.3 shows tritium accumulation on a gold sample (blue data points), measured with TRIADE by Röllig (2015). The goal of this study was to investigate potential surface activity increase of the designated golden RW during tritium operation at KATRIN. As a reference, the orange data points show the temporal evolution of the RW rate measured during KATRIN neutrino-mass campaign (KNM) 5+6 (Aker et al., 2024; Aker, 2025), with rescaled x-axis to be directly comparable to the TRIADE measurements. Both datasets show excellent qualitative agreement, which confirms the suitability of external measurements on surface activity build-up.

A setup similar to TRIADE, the Tritium Activity Chamber Experiment (TRACE), explained in more detail in subsection 5.2.2, was upgraded to investigate UV/ozone de-

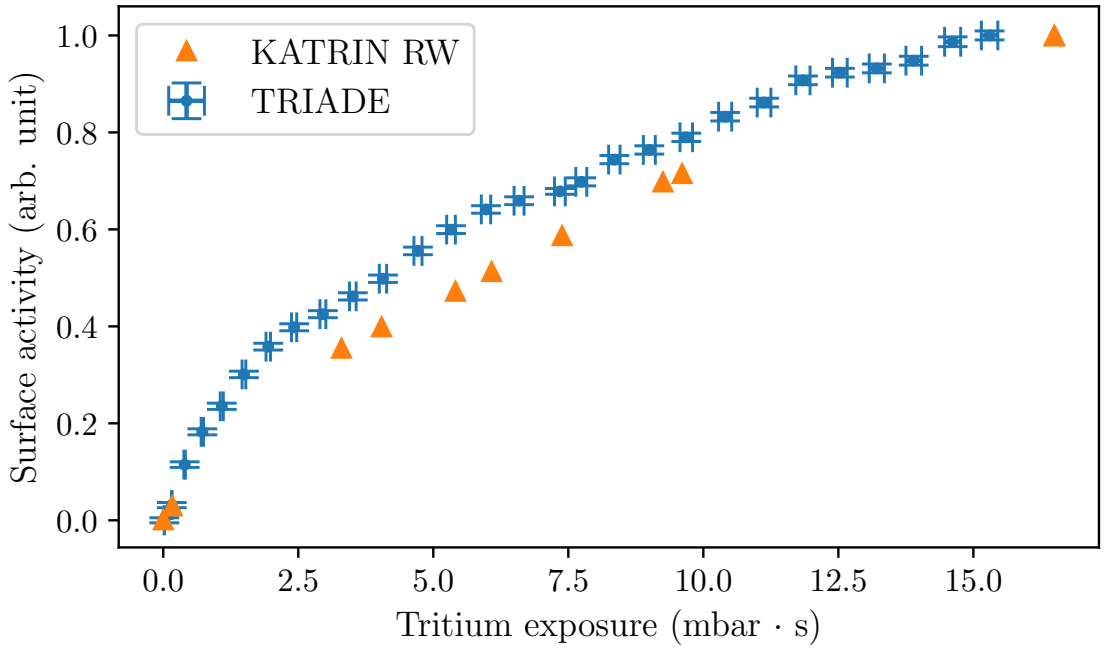

Figure 4.3: Tritium accumulation on gold measured with TRIADE (Röllig, 2015), and on the golden KATRIN RW during KNM5+6 (Aker, 2025). TRIADE used X-rays according to the BIXS principle to measure the activity, while the FPD was used to detect the electrons from the decay of surface-bound tritium on the KATRIN RW directly.

contamination. After this upgrade, it is not only possible to measure gradual tritium contamination, but also to in-situ decontaminate samples by exposure to ozone, while monitoring the surface activity in close to real time. This was realised by connecting a self-built ozone generator. To utilise the ozone to its full extent, more of its basic properties within vacuum systems, like production and lifetimes, as well as the equilibrium concentration, need to be better understood. A wide variety of literature on ozone in earth's atmosphere is available, but mostly inapplicable due to the lack of surfaces. Hence, a dedicated, tritium-compatible experimental setup was built and commissioned to measure these properties of ozone (subsection 4.4.2). In the next section, a brief overview of basic ozone chemistry regarding UV radiation and its cleaning mechanism is given.

4.3 Decontamination mechanism

For the in-situ RW decontamination in KATRIN, two mercury vapour UV lamps (miniZ by RBD Instruments) were installed, which can be used to apply the UV/ozone cleaning method. Until now, the RW has been decontaminated three times, with a highest achieved surface activity reduction by three orders of magnitude (Aker et al., 2024; Aker, 2025). UV/ozone cleaning is a widely used method in industry, e.g. for treating semiconductors,

since it not only removes tritium (Krasznai & Mowat, 1995; Shu et al., 2002; Gentile et al., 2002; Larsen et al., 2022), but organic compounds in general, leaving behind atomically clean surfaces (Vig, 1985; Musket, 1989). However, there is no consensus in literature on whether the decontamination effect should be attributed to UV radiation, ozone, or their combination. In fact, there is contradictory information available, e.g. ascribing the desorption to etching effects from ozone (Ishikawa & Hirose, 1997), or atomic oxygen radicals (Li et al., 2022) interacting with the surface. On the other hand, Oya et al. (2001) trace it back to UV radiation dissociating the tritiated hydrocarbons. UV illumination on its own was deemed ineffective in reducing the RW activity (Aker et al., 2024; Aker, 2025). A combination of both UV light and ozone was found to be most effective by Vig (1992).

In KATRIN, it is likely that UV radiation and ozone will continue to be used simultaneously and their impact on the decontamination efficiency cannot be disentangled. For this reason, it is important that both factors are sufficiently understood.

4.3.1 Interactions of UV radiation with oxygen

The production of ozone within a vacuum system from molecular oxygen using UV radiation follows the governing photochemistry of the oxygen-ozone cycle, also known as the Chapman cycle in atmospheric science (Chapman, 1930; Dütsch, 1968). In the reactions below, the wavelengths given correspond to the respective emission line present in the spectrum of the mercury UV source used in this study. In reality, the photons only need a minimum energy to induce the reaction.

Ozone generation

As a first step, molecular oxygen is dissociated by the absorption of a UV photon. The resulting atomic oxygen recombines with another oxygen molecule to form ozone:

$$\mathrm{O_2} + h\nu_{185\,\mathrm{nm}} \rightarrow 2\,\mathrm{O} \tag{4.1}$$

$$\mathrm{O_2} + \mathrm{O} + \mathrm{M} \rightarrow \mathrm{O_3} + \mathrm{M}, \tag{4.2}$$

where $h\nu$ denotes photons with a specific wavelength, O depicts oxygen, and M represents an additional particle for energy and momentum conservation.

Ozone destruction

In turn, there are also effects through which ozone is depleted or its production hindered. The second and most intense emission line at a wavelength of 254 nm is responsible for dissociating ozone into the same constituents it forms from. If atomic oxygen reacts with ozone instead of molecular oxygen, the ozone is also destroyed to produce oxygen molecules. Recombination of two oxygen atoms acts as a sink reaction to inhibit ozone formation, however, this is only a minor effect due to the low concentration of atomic oxygen. The reactions are given below:

$$O_3 + h\nu_{254\,\mathrm{nm}} \rightarrow O_2 + O \tag{4.3}$$
$$O_3 + O \rightarrow 2\,O_2 \tag{4.4}$$
$$2\,O + M \rightarrow O_2 + M. \tag{4.5}$$

It is generally possible for both oxygen molecules and atoms to be left in an excited state after a reaction. Photodissociation of ozone, as given in Equation 4.3, can generate a significant fraction of singlet oxygen (Houston, 2004; Schinke & McBane, 2010), which is even more reactive than ground-state oxygen (Wayne, 1969).

If water vapour is present, e.g. as residual humidity in a vacuum system, it can also lower the ozone concentration by either hindering its production due to the removal of atomic oxygen

$$O + H_2O \rightarrow 2\,OH, \tag{4.6}$$

or by reacting with the products of photodissociated water according to

$$H_2O + h\nu_{185\,\mathrm{nm}} \rightarrow H + OH \tag{4.7}$$
$$O_3 + H \rightarrow OH + O_2 \tag{4.8}$$
$$O_3 + OH \rightarrow HO_2 + O_2. \tag{4.9}$$

HO_2 from Equation 4.9 can in turn also deplete ozone. An overview of more possible reactions is given in Dütsch (1968).

4.3.2 Reaction of ozone with surfaces

The equations listed previously were derived from phenomena occurring in the Earth's atmosphere and do not consider interactions with surfaces. Surfaces of vacuum systems, commonly based on stainless steel, can act as carbon reservoirs from which hydrocarbons can form. A possible decontamination effect of ozone can be explained by the Criegee mechanism, which describes the reaction chain of ozone breaking carbon-carbon double bonds (Criegee, 1975; Geletneky & Berger, 1998). By the end of this process, volatile hydrocarbons are created which can be evacuated by pumps. UV radiation can possibly accelerate this process by either excitation or even dissociation of the initial hydrocarbons, which increases their susceptibility to reactions involving ozone (Vig, 1985). In the absence of hydrocarbons, metal and metal oxide surfaces are also known to act as catalysts for ozone depletion (Dhandapani & Oyama, 1997).

Previous studies hint towards surfaces playing a significant role in depleting ozone. While the lifetime of ozone in the atmosphere ranges from the ten-day (Prather & Zhu, 2024) to month (Bekki, S. & Lefevre, F., 2009) scale, lifetimes of only up to 36 hours were reported in laboratory experiments (McClurkin & Maier, 2010). Ozone-surface interactions being the primary depletion mechanism would be optimal for the decontamination, and short lifetimes, implying high reaction rates, are ideal. It is evident that the ozone

lifetimes depend on many factors, some of them potentially unknown that cannot be directly controlled or observed. Hence, more information on the decontamination effect in KATRIN can only be obtained experimentally under similar conditions.

4.4 Tritium compatible ozone production and monitoring

Regardless of the destruction channels of ozone on surfaces, a thorough understanding of its production and lifetime in confined spaces is required to understand and improve the efficiency of future UV/ozone decontaminations. To gain this knowledge, a tritium-compatible vacuum system with continuous composition analysis of the contained gas has been designed, commissioned and calibrated, as described in the following sections.

4.4.1 Requirements to investigate ozone

To successfully follow and investigate ozone chemistry, especially its lifetime, a system has to be designed which includes the following prerequisites:

- Molecular oxygen to serve as a basis for ozone production,
- UV radiation for photodissociation of molecular oxygen to form ozone,
- a vacuum system, within which ozone can be created without interference from the environment,
- analytics to monitor pressure, temperature and ozone content within the vacuum system.

In view of the above-mentioned requirements, the vacuum system must fulfil additional technicalities:

- Explosion safety:

  To mitigate the hazards of producing ozone, the use of oxygen in its pure form is to be avoided. Instead, a mixture with nitrogen – dry/synthetic air – is used.

- Low amount of impurities in the oxygen containing gas:

  Since the ozone properties are influenced by humidity and other trace gases, it is necessary to produce the ozone from relatively pure synthetic air. The gas should be supplied from a gas cylinder to guarantee reproducible gas mixtures at the start of each measurement.

- Low leak rate:

  The system should possess leak rates below $10^{-6}\,\mathrm{mbar{\cdot}l/s}$ to avoid introducing impurities in the form of ambient air which can react with the ozone.

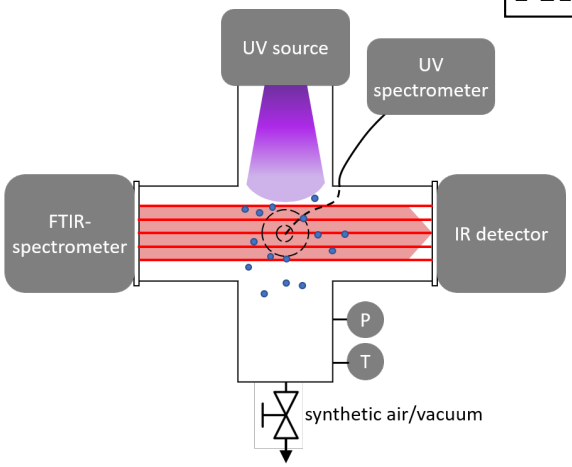

(a) Schematic of the measurement devices used, as published in Batzler et al. (2024) under the CC BY 4.0 license https://creativecommons.org/licenses/by/4.0/.

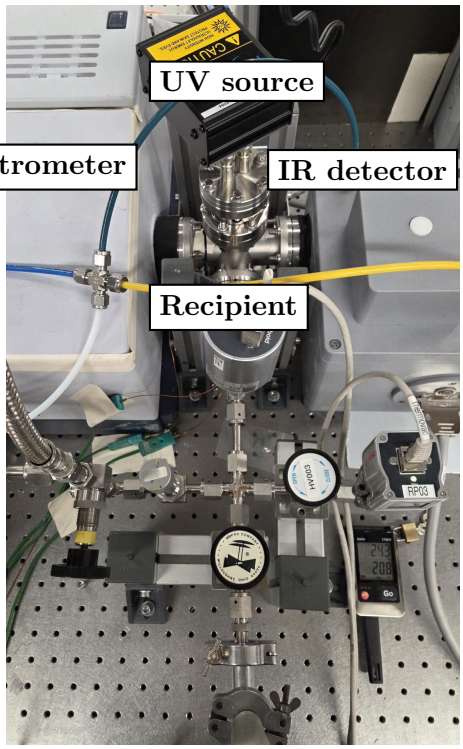

(b) The UVO setup

Figure 4.4: The UVO setup to determine properties of ozone in a recipient in a tritium-compatible manner. (a): Sketch of the measurement principle of absorption spectroscopy to determine the gas composition. (b): Physical setup located in the optics laboratory.

- Use of ozone-compatible components:

  Certain kinds of elastomer seals should be avoided, since these lose their leak tightness after prolonged ozone exposure. Preferred materials are metals, ceramics and glass. Components which are fully compatible with tritium are also suitable to be used with ozone.

4.4.2 The UVO test setup

With these requirements in mind, the UVO experiment (Figure 4.4) was set up. It consists of a DN40 CF double cross, within which the ozone is produced using a UV mercury lamp with discrete emission lines, similar to the setup at the KATRIN RW. Two opposing flanges incorporate ZnSe windows to enable Fourier transform infrared (FTIR) absorption spectroscopy of the contained gas mixture. Another UV fused silica window allows for monitoring the UV source using a compact grating spectrometer. A gas cylinder supplies 20.5% oxygen in nitrogen, with traces of water $< 2\,\mathrm{ppm}$, hydrocarbons $< 0.1\,\mathrm{ppm}$, carbon monoxide and carbon dioxide $< 0.5\,\mathrm{ppm}$. A pump station allows the system to be

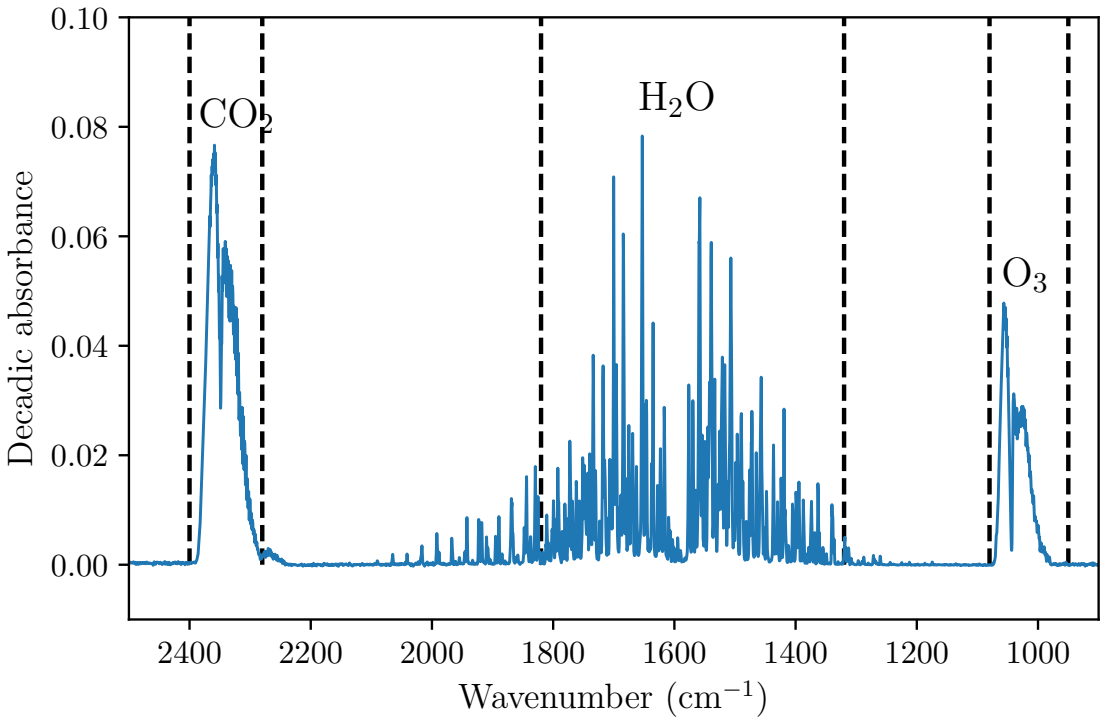

Figure 4.5: Selected wavenumber region of a processed IR spectrum. Absorption features of ambient CO_2 and H_2O, as well as O_3 in the vacuum system are visible. The dashed lines indicate the integration limits used in the data analysis.

evacuated to a pressure of $< 10^{-3}$ mbar to minimise the gas content from the previous measurement.

4.4.3 Monitoring tools for UV and ozone

To analyse both the gas composition and the UV source intensity, a combination of FTIR and UV spectroscopy is used. The FTIR spectrometer utilised is of type Tensor27 by Bruker, and the UV spectrometer is a Broadcom Qwave variant. An introduction, as well as an in-depth treatment of FTIR spectrometry is provided in Griffiths and De Haseth (2007).

4.4.3.1 FTIR spectroscopy for compositional gas analysis

Since FTIR absorption spectroscopy is sensitive to a molecule's transition dipole moment over large spectral ranges, a multitude of species, e.g. hydrocarbons, CO_2, H_2O, and O_3, can be detected in the system. Additionally, an exposure time of less than a minute per spectrum allows to track chemical processes. Hence, with the FTIR spectrometer it is possible to both identify and quantify the individual gas constituents in-line and without

interference. The acquisition parameters for the spectra, as well as parameters used in the analysis are given in Appendix D.

The basis of absorption spectroscopy is given by the Beer-Lambert law, which describes the wavelength-dependent absorption of radiation while propagating through an optically thick medium:

$$I(\tilde{\nu}) = I_0(\tilde{\nu}) \cdot e^{-\sigma(\tilde{\nu})nl}, \tag{4.10}$$

with the initial and transmitting intensities I_0 and I, wavenumber $\tilde{\nu}$, absorption cross section σ, molecule number density n, and path length within the absorbing medium l. Rearranging Equation 4.10 leads to

$$\ln 10 \int_{\tilde{\nu}} A \, \mathrm{d}\tilde{\nu} = \ln 10 \int_{\tilde{\nu}} \log\left(\frac{I_0}{I}\right) \mathrm{d}\tilde{\nu} = n \cdot l \int_{\tilde{\nu}} \sigma \, \mathrm{d}\tilde{\nu}, \tag{4.11}$$

with the quantity A being the absorbance, which is the negative logarithm of the transmittance. Since only I is measured directly with the FTIR spectrometer, it is required to determine I_0, l and σ by different means to obtain the molecule number density n.

Multiple spectroscopy databases for absorption cross sections exist. In this study, the high-resolution transmission molecular absorption database (HITRAN) (Gordon et al., 2022) is used, which consists of a mixture of theoretical and experimentally determined cross sections for various molecules in the infrared (IR) range.

For obtaining I_0, the spectral baseline correction, which considers the broad band emission of the IR source, is performed similarly to Größle (2015) using a rolling-circle filter (Mirz et al., 2019). In the wavenumber range relevant for ozone, the baseline curvature is sufficiently low for a linear fit. From the baselines, the decadic absorbance can be calculated. Figure 4.5 shows the wavelength-dependent absorbance of an exemplary IR spectrum, in which absorption features are generated by the presence of CO_2, H_2O and O_3. There are in principle two ways in which measured and reference spectra can be compared; either differentially by fitting one spectrum to the other, or by calculating their integral over individual vibrational transitions and comparing the resulting scalar. To mitigate the noise present in the measured spectra, the integration method is used in this study. In Figure 4.5, also the integration limits of the individual species are marked.

The last unknown quantity, the absorption path length l, needs to be obtained by performing a dedicated calibration using toluene. Toluene is commonly employed in spectroscopic applications due to its relatively low uncertainties of $< 2\%$ on its absorbance (Sharpe et al., 2004). The recipient was evacuated and filled with evaporating toluene from a liquid reservoir. In this case, a pressure of 11 mbar was chosen, which already produced sufficiently strong absorption features. Performing this procedure ensures that vapour-phase toluene is the only molecule species in the optical path of the IR spectrometer, hence, the molecular number density n can be calculated from the ideal gas law. By applying Equation 4.11, the absorption path length l could be extracted by fitting, leaving it as a free parameter. Figure 4.6 displays a differential fit of the reference cross sections taken from HITRAN to the measured IR spectrum of toluene in the wavenumber window relevant for ozone. At a wavenumber of $1032\,\mathrm{cm}^{-1}$, the fit shows a strong disagreement with the measured data due to the reference data being measured with a

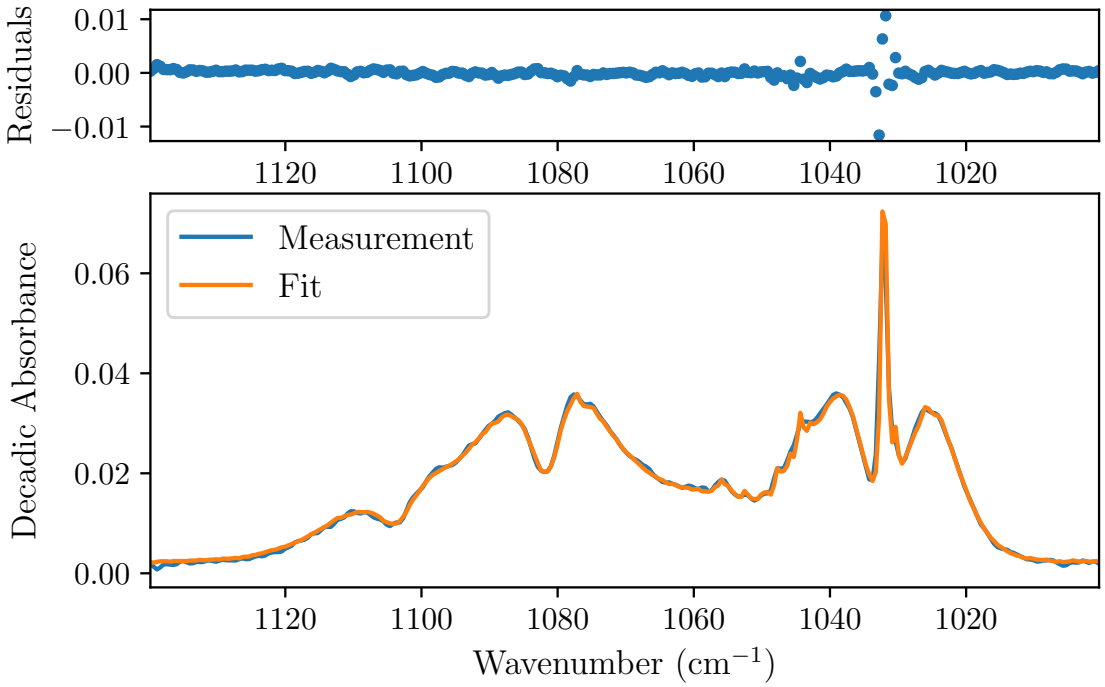

Figure 4.6: Differential fit of toluene reference data from HITRAN with its residuals for absorption path length calibration, yielding (11.89±0.24) cm for the path length. The strong disagreement between fit and data at 1032 cm^{-1} is an artefact stemming from the HITRAN data being measured with a higher spectral resolution, which only impacts narrow-band features.

higher spectral resolution. One possibility to prevent this is by convolving the reference spectrum with the instrument line shape function, which can be obtained by measuring an infinitely narrow spectral feature with the specific instrument. For FTIR spectrometers, this is a sinc-like function, with varying magnitude of the sidelobes depending on the measurement parameters (Griffiths & De Haseth, 2007). Since determining the exact function with the correct width requires elaborate measurements with specialised equipment, and the remaining spectrum is fully resolved, the convolution was neglected. Including the uncertainty on the cross sections of 2%, the absorption path length was determined to be $l = (11.89 \pm 0.24)$ cm, which is used to quantify ozone. With the path length calibration performed, it is possible to measure to quantity of any individual molecule, provided its absorption cross sections are available.

To verify the IR analysis chain, the measured ozone concentrations were compared to those obtained from a commercially available pre-calibrated ozone monitor (Ozone Monitor 206-MH from 2B Technologies) that uses absorption spectroscopy in the UV range. The device requires a connection to the recipient via Teflon tubes, through which it circulates the ozone-containing gas for internal analysis. Figure 4.7 shows the agreement

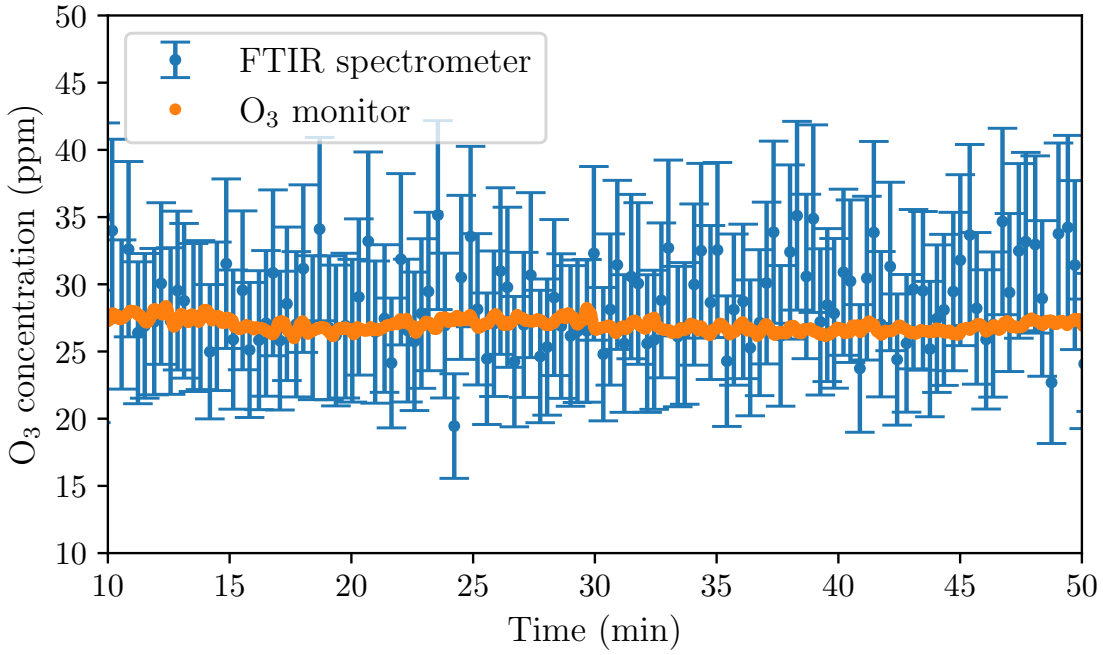

Figure 4.7: Comparison of the ozone concentrations measured with the FTIR spectrometer after calibration and a commercial, non-tritium compatible ozone monitor. For the IR spectrometer, the uncertainties on the reference absorption cross sections are the dominant source of uncertainty.

of the concentrations from the calibrated IR spectrometer with the data from the ozone monitor. While both datasets are consistent, the errors are significantly larger for the IR measurements. Two reasons were identified for this. Firstly, the absorption cross sections of ozone in the IR wavelength region are two orders of magnitudes smaller than in the UV, which explains the larger spread in data. Secondly, the relative uncertainties on the available IR cross sections are up to 20% (Flaud et al., 2003; Tyuterev et al., 2014), resulting in the large errorbars when converting the data to concentration. According to the ozone monitor's data sheet, it measures ozone concentrations with an accuracy and precision of 0.05 ppm or 2%, depending on which number is higher. Despite the higher accuracy, the commercial device is unsuitable for tritium applications due to the materials used and its high leak rate.

4.4.3.2 UV spectroscopy for UV source monitoring

Since ozone also absorbs UV wavelengths leading to molecular dissociation, a UV grating spectrometer (Broadcom Qwave AFBR-S20W2UV) coupled to an optical fibre is utilised to independently monitor the presence of ozone, as well as measuring the UV source intensity. The measured, normalised spectrum of the UV source (Figure 4.8) shows mercury's

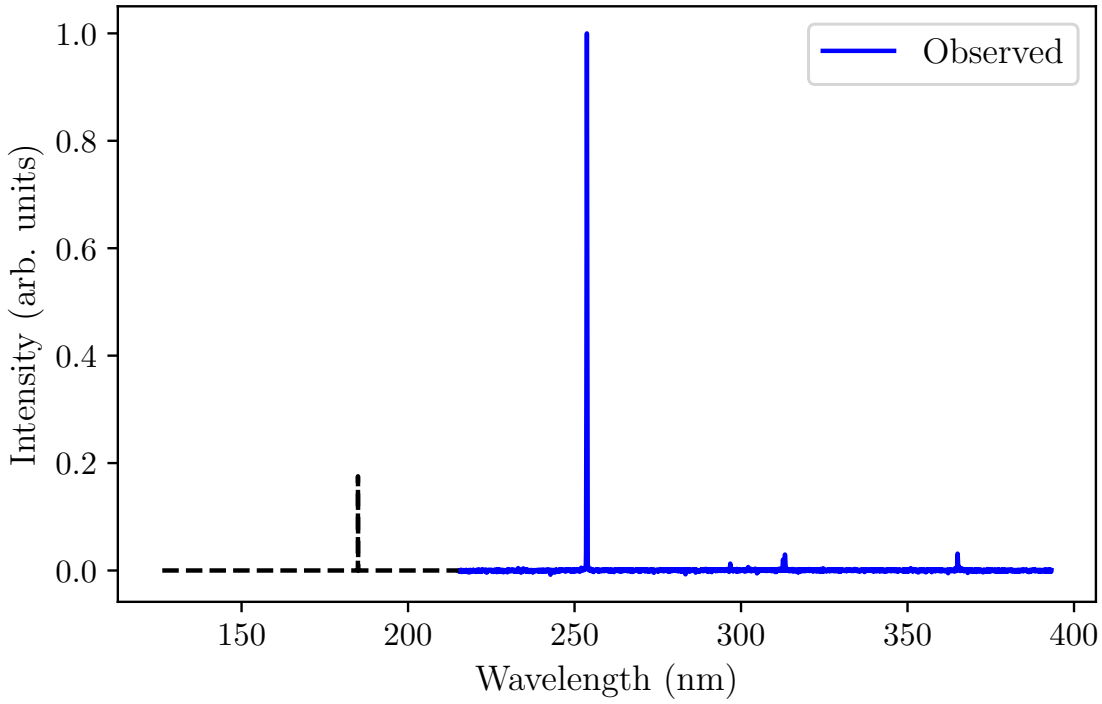

Figure 4.8: UV emission spectrum of the mercury lamp used in this study. The solid line represents the region of the spectrum that is visible with the UV spectrometer.

distinct emission line at 254 nm. With a spectral range of (220 – 390) nm, the line at 185 nm, responsible for ozone production, cannot be observed directly.

4.5 Investigation of ozone production and lifetimes

With the analytics in place to quantify the ozone content in gasses, first investigations on the interplay of UV radiation and synthetic air was performed using both IR and UV spectrometer. The results reported here were obtained from a follow-up study to a bachelor's project.[1]

Figure 4.9 shows the behaviour of synthetic air under UV irradiation. At the start of the measurement, the ozone concentration measured with the FTIR spectrometer, and UV intensities of the source emission lines at 254 nm and 365 nm, as measured with the UV spectrometer, are at their respective zero-points. The time span during which the UV source was switched on is displayed as the grey-shaded area. The warm-up of the UV source can be extracted from the emission line at 365 nm (green data points), which is not absorbed by the process gas constituents and follows an exponential growth. As the

[1] Peter Winney, "Druckabhängige Produktions- und Zerfallsraten von Ozon zur Dekontamination der KATRIN-Rearwall", Bachelor's thesis, IAP-TLK, 2022

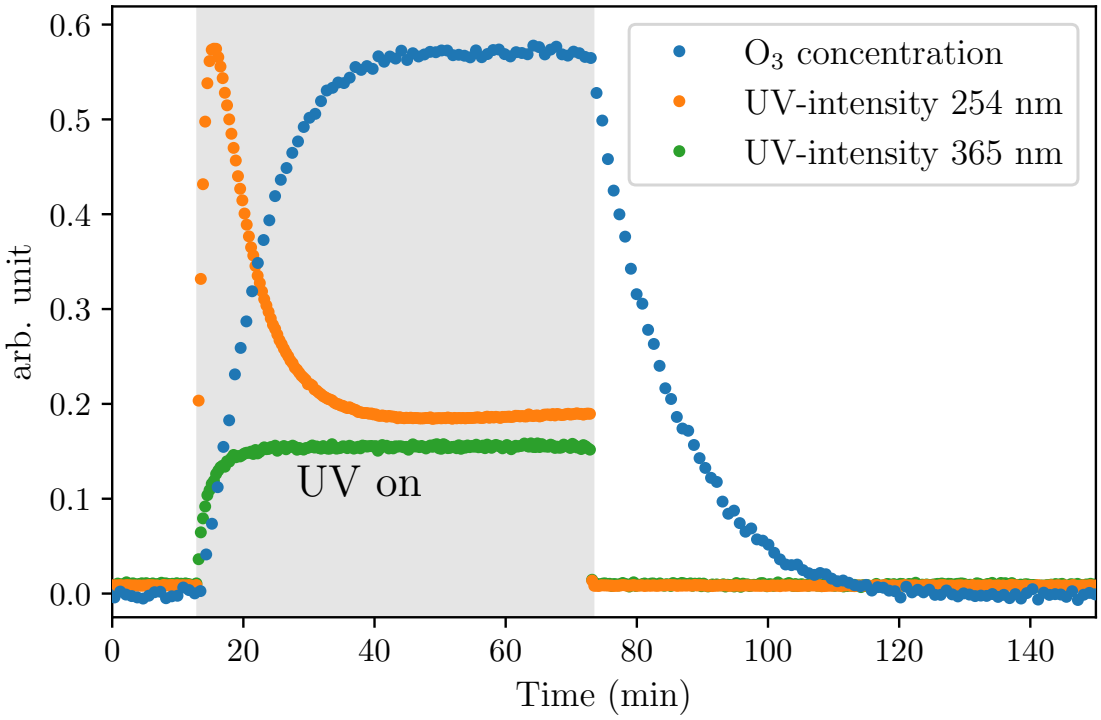

Figure 4.9: Interaction of UV radiation with molecular oxygen and ozone. The blue data points show the ozone quantity, which increases as soon as the UV source is turned on, and depletes when it is turned off. The source warm-up behaviour is visible in the increasing intensity at 365 nm, displayed in green. Wavelengths of 254 nm (orange) experience strong absorption due to the presence of ozone.

molecular oxygen is irradiated with UV, ozone forms. The ozone concentration increases as the sum of two exponential functions, with one of the two representing the source warm-up. In this instance, after about 25 min, the equilibrium concentration of ozone has been reached. The time evolution of the 254 nm line intensity (orange data points) shows a more complex behaviour. After a steep increase due to the warm-up, the gradual generation of ozone leads to significant absorption of exactly this wavelength, resulting in a sudden and continuing decrease in intensity until the equilibrium is reached. Within this study, a minimum transmittance of 7% could be observed. As soon as the UV source is switched off, the ozone decays exponentially.

To further explore the destruction mechanism of ozone, its production and lifetimes, as well as its equilibrium concentration are investigated at different absolute pressures. Prior to ozone production, the entire system is evacuated and filled two to three times to purge as much of the residual gas as possible. Multiple cycles of ozone production and destruction are recorded from absolute pressures ranging from 100 to 1000 mbar in 100 mbar steps. The production and depletion or lifetimes are defined as the time after the

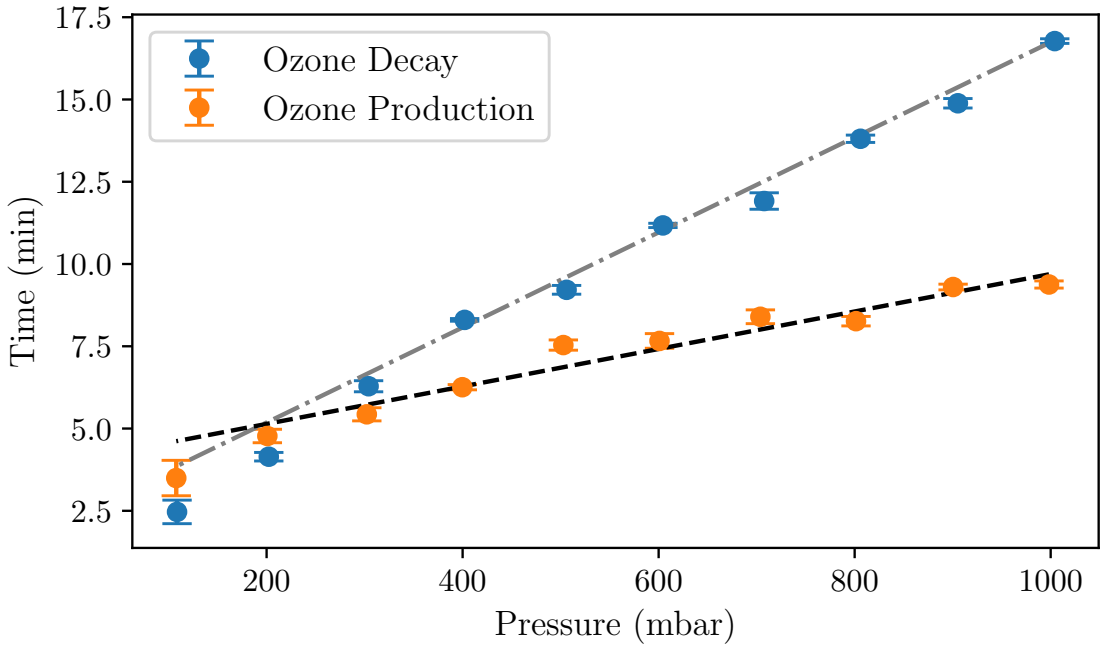

Figure 4.10: Ozone production and lifetimes as a function of pressure. Both properties show a linear dependence.

ozone concentration reached $1-1/e$ and $1/e$ of the equilibrium concentration, respectively, and are obtained through exponential fits. The ozone production and lifetimes are depicted in Figure 4.10, showing a linear dependence ranging from about 3 to 8 minutes and 2 to 17 minutes, respectively. The production time seems to transition to non-linear behaviour towards an even shorter timescale below 100 mbar. Unfortunately, at even lower pressures it is not possible to extract reliable information with the FTIR spectrometer due to too low ozone molecule number densities for their relatively small absorption cross section.

A closer look into ozone decay shows that the concentration follows a simple exponential function (Figure 4.11). The fit residuals reveal a sinusoidal structure in the percent level, that could be caused by various effects. Generating ozone induces a spatial temperature gradient of up to 5 K at the UV lamp. As soon as it is switched off, the system cools down and the temperature gradient, but also convection, vanish. The same exponential decrease was also observed for the RW activity during its UV/ozone decontamination (Figure 4.12), although with a longer time constant due to the significantly larger volume of the RW vessel. Since ozone must be involved in the desorption of tritium, the similarity of the temporal evolutions of ozone concentration and surface activity indicate that ozone is indeed primarily depleted on surfaces.

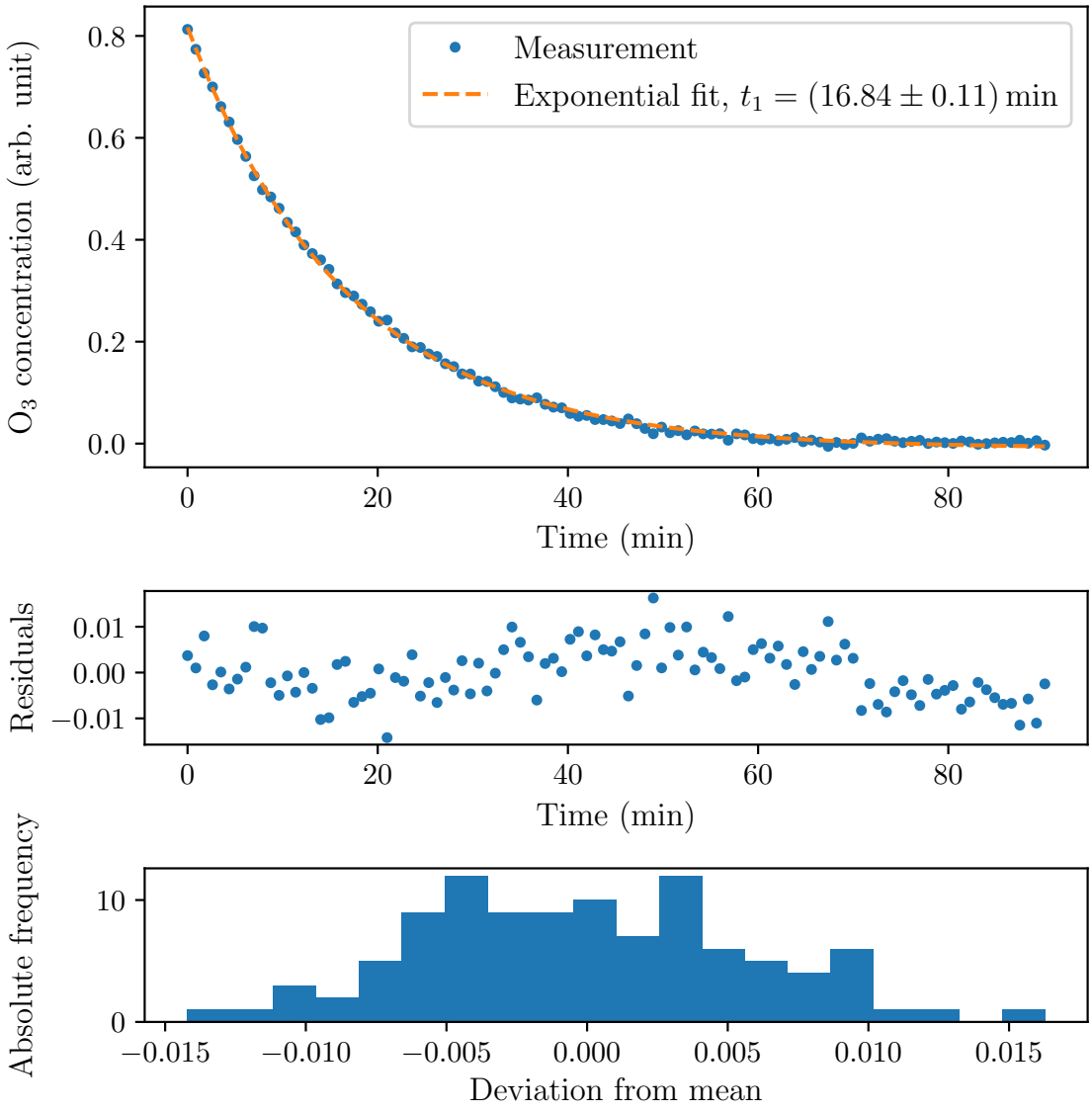

Figure 4.11: Fit of uncalibrated ozone concentration measured in the UVO setup at a pressure of 1000 mbar during decay, together with the residuals and histogram of deviation from the mean. Reasons for the slight differences of the data to exponential decrease are discussed in the main text.

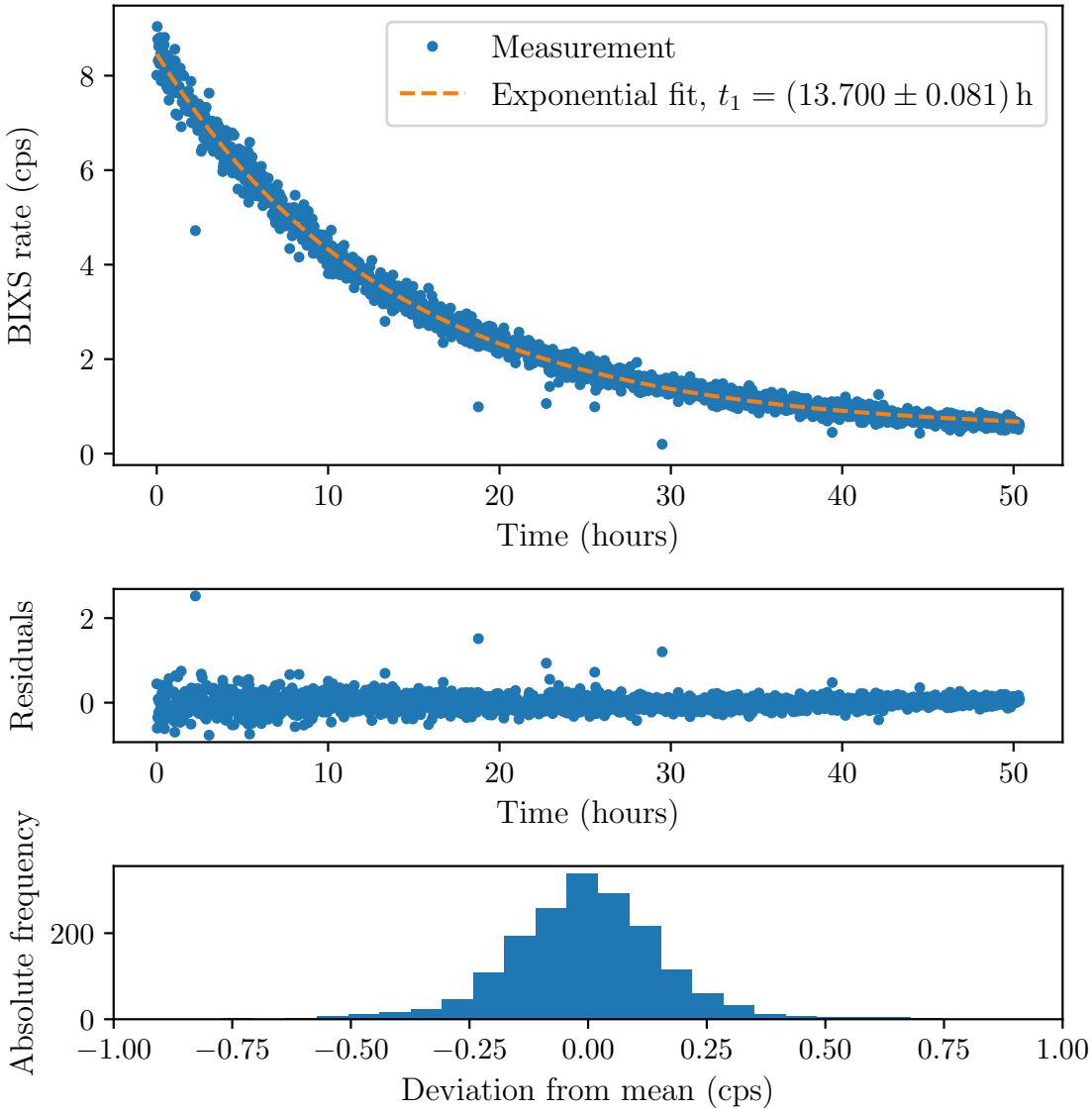

Figure 4.12: Fit of the BIXS rate, corresponding to surface activity, during step 14 (prolonged UV/ozone exposure) of the KATRIN RW decontamination. The temporal activity reduction perfectly follows a simple exponential decrease.

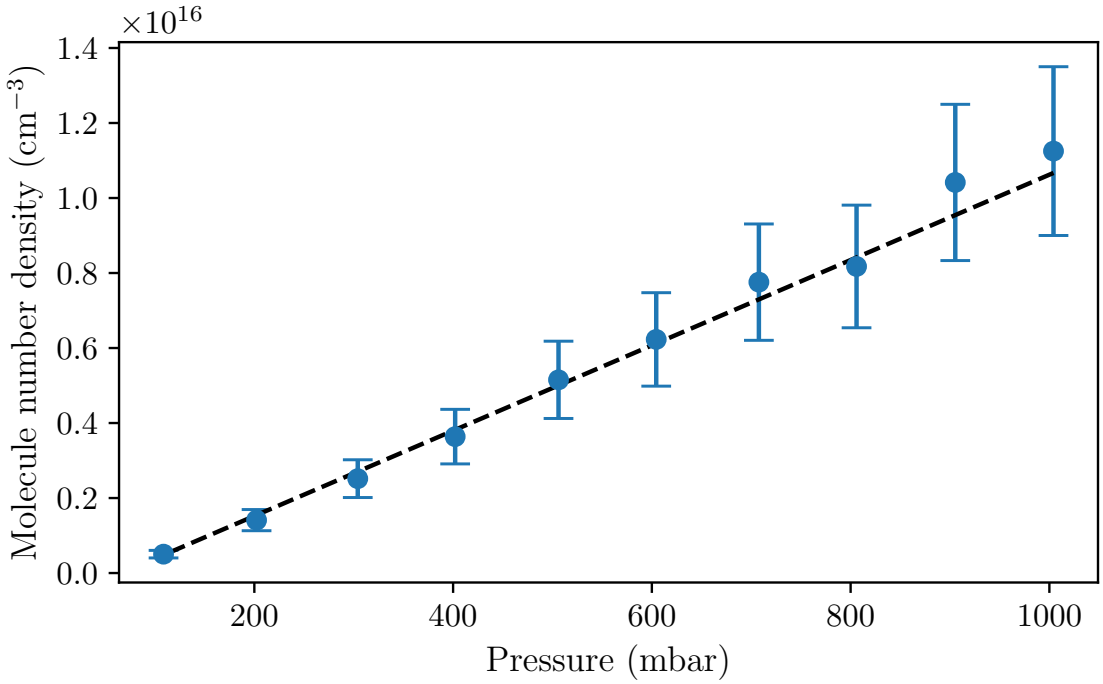

Figure 4.13: Ozone molecule density in equilibrium over pressure. The large errors result from the systematic uncertainty on the absorption cross sections.

4.5.1 Equilibrium concentrations

Since ozone is continuously created and destroyed within the vacuum system, an equilibrium concentration is reached. The number of ozone molecules available to react with contaminants during UV/ozone cleaning could severely affect its efficiency. Hence, it is important to exactly know the ozone concentration. From the measurements conducted on the production and lifetimes, the ozone molecule number density in equilibrium can be extracted as well, which is shown in Figure 4.13. Similar to the these properties, the number density scales linearly with pressure and shows a slope of $(1.138 \pm 0.030) \cdot 10^{13}$ molecules/mbar. Converting the number densities to concentrations gives (193 ± 39) ppm and (466 ± 93) ppm at pressures of 100 and 1000 mbar, respectively. With increasing pressures, the ozone concentrations show a saturation behaviour (see Appendix E), which is not yet fully understood. However, two reasons to explain this observation with are plausible. With higher pressures, interactions of ozone with other gas-phase molecules, potentially leading to depletion, become more likely due to the decrease in mean free path. Additionally, the 254 nm UV radiation is subject to stronger attenuation with a higher number of ozone molecules, which changes the spatial intensity gradient.

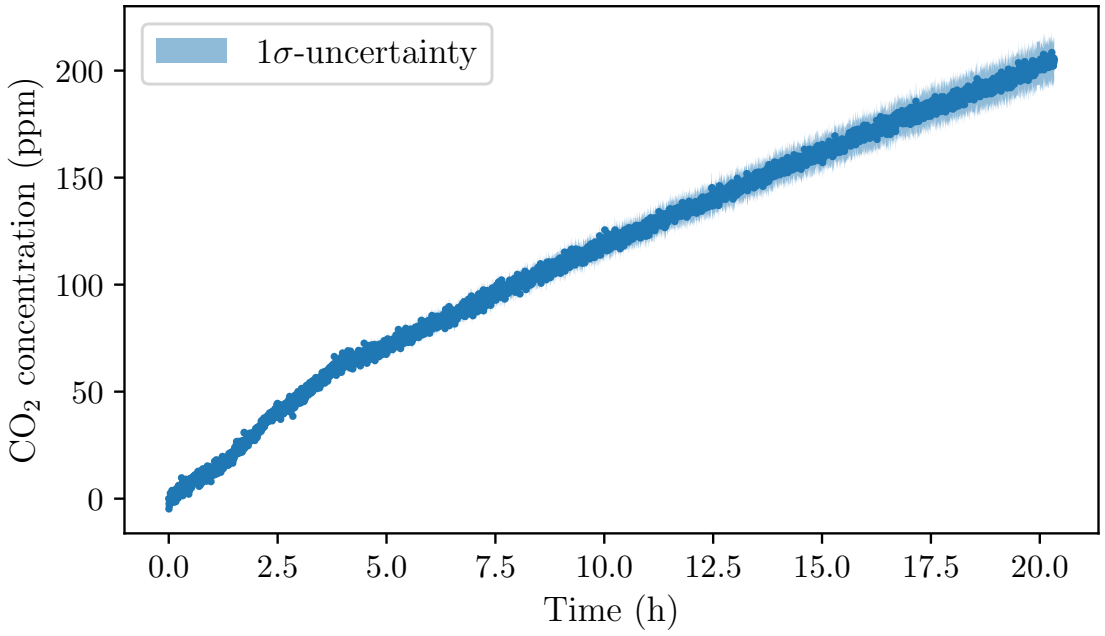

Figure 4.14: CO_2 production during ozone exposure in an early experimental stage. With subsequent ozone measurements, the effect gradually vanished. Since the gas mixture initially possessed hydrocarbon concentrations in the sub-ppm level, it is suspected that the carbon is released from the stainless steel surfaces.

4.5.2 CO_2 production as a hint for UV/ozone cleaning

In the starting phase of the experiment, ambient air was used for ozone production and the time constants for ozone were observed to be greater by roughly a factor of two. After selecting synthetic air from a gas cylinder as the initial mixture, multiple measurement campaigns as those shown in Figure 4.10 caused the time constants to converge to the reported stable level. Concurrently, large amounts of CO_2 were produced in early ozone exposures (Figure 4.14), which had not occurred in later measurements. Since no carbon was expected in the initial gas mixture, this again implies that the ozone was destroyed at the surfaces by reacting with and dissociating adsorbed hydrocarbons, leading to a cleaning effect. The hydrocarbon-depleted stainless steel surfaces might act as a more efficient catalyst for ozone destruction, causing the reduced time constants.

4.6 Ozone transport

If it is not possible to produce ozone in the vicinity of the surfaces to be decontaminated, it may be necessary to transport it within the system. Due to the high reactivity of ozone, this poses a challenge. To demonstrate this, slight hardware adaptations were made on the system (Figure 4.15). An additional chamber equipped with a UV source was connected

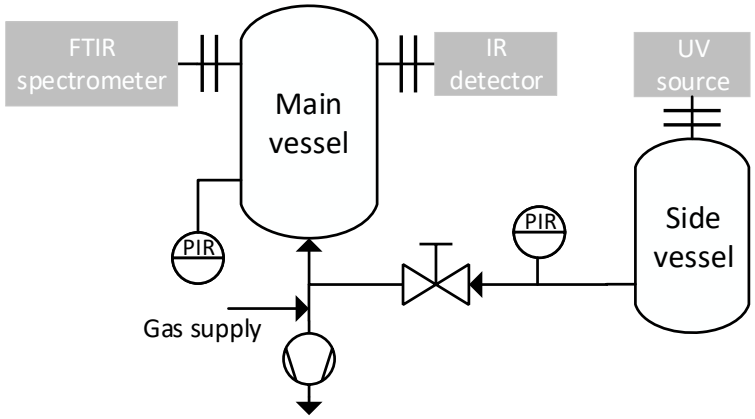

Figure 4.15: Simplified P&ID diagram of the adapted UVO setup to examine ozone transport. An additional vessel was connected, in which ozone could be generated. By opening the valve to the main recipient, ozone can be transported into the optical path of the FTIR spectrometer via gas expansion.

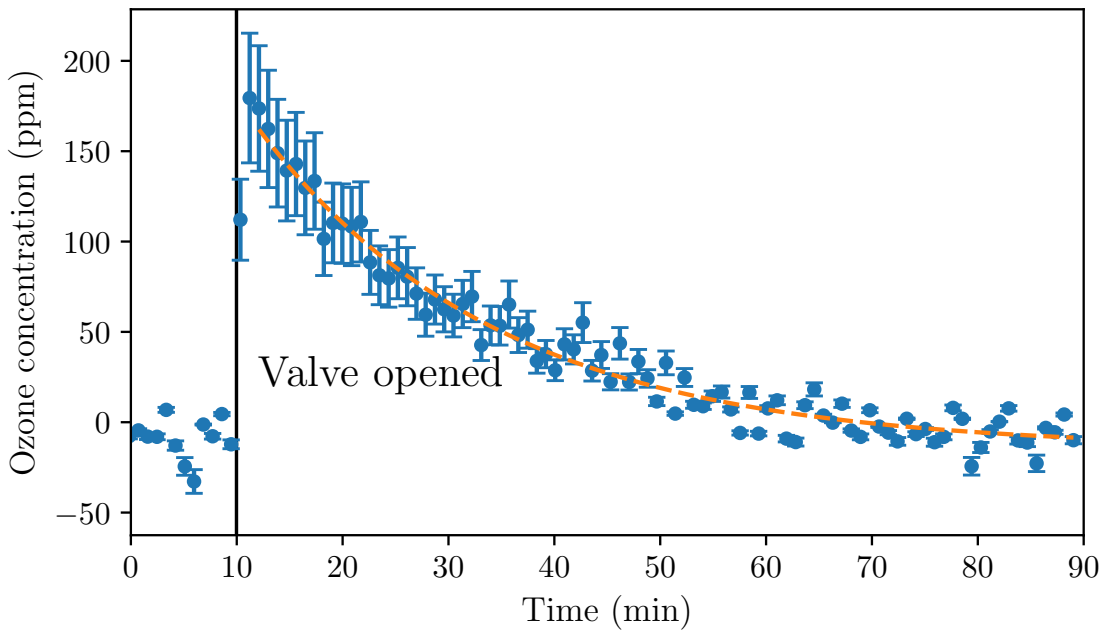

Figure 4.16: Ozone concentration in the initially evacuated UVO setup. The ozone was produced in a side chamber. At the 10 minutes mark, the valve was opened and the ozone containing gas expanded into the main chamber for detection. The large errorbars originate from the relative uncertainty on the absorption cross sections of 20%.

to the UVO setup and separated with a valve. The distance between the side and main chamber was around 40 cm, consisting of stainless steel pipes with an inner diameter of around 1 cm. Firstly, ozone was produced in the side chamber and the valve to the main chamber remained opened. Even after hours, the ozone could not reach the FTIR spectrometer for detection. Hence, with a lifetime of around 20 minutes, ozone transport by diffusion alone is not feasible for longer distances. As shown in Figure 4.16, transport via gas expansion is possible. Initially, the main chamber was evacuated and the valve to the side chamber, which contained ozone, was closed. After ten minutes, the valve was opened and a sudden ozone concentration of 170 ppm could be observed. Since the ozone was produced at a pressure of 1 bar, about 400 ppm should be expected. It is unclear if some of the ozone was destroyed during the transport or if less ozone was produced because the side chamber was not conditioned by multiple ozone measurements. Still, a considerable amount of ozone reached the main chamber, which makes gas expansion a promising transport mechanism. To improve the transport efficiency, e.g. increasing the distance or the final concentration, more investigations are necessary. The Reynolds number of the flow might have a major influence on the transport, as turbulences could induce the ozone to hit the surfaces and be destroyed in the process.

4.7 Interaction of deuterium with surfaces previously exposed to ozone

After having understood the behaviour of ozone inside a vacuum system, deuterium was used to investigate the chemical interactions between ozone and hydrogen isotopes without the radiochemistry tritium introduces.[2] Firstly, the evacuated system was filled with 1 bar of deuterium to saturate its surfaces, simulating tritium surface contamination. After a couple of hours, the system was evacuated again and an ozone measurement as previously described was conducted. It was expected that in the IR spectrum, absorption features of deuterated hydrocarbons and heavy water would gradually develop due to ozone-induced desorption. Fully desorbing a monolayer of deuterium bound to carbon would result in an estimated hydrocarbon concentration of roughly 25 ppm at 1 bar in the gas phase, assuming an average atomic deuterium to carbon ratio of 4:1. However, after sufficiently long times, none of these species could be observed with the FTIR spectrometer's detection limit for the number of molecules. This corresponds to minimum concentrations of $\mathcal{O}(1\text{–}100\,\text{ppm})$, depending on the species, that can be measured. It is likely that the elaborate measurements on ozone properties depleted the stainless steel surfaces of carbon, which could explain why no hydrocarbons were formed (see subsection 4.5.2). Between the preceding ozone measurements and the deuterium campaign, the recipient remained closed to prevent recontamination of the inner surfaces from contact with ambient air. Unexpectedly, the formation of gas-phase D_2O could be detected every time the system was filled with deuterium after an ozone measurement. The D_2O concentration (Figure 4.17)

[2] Semen Rusakov, "Spectroscopic study of UV-Ozone decontamination of deuterated surfaces", Bachelor's thesis, IAP-TLK, 2023

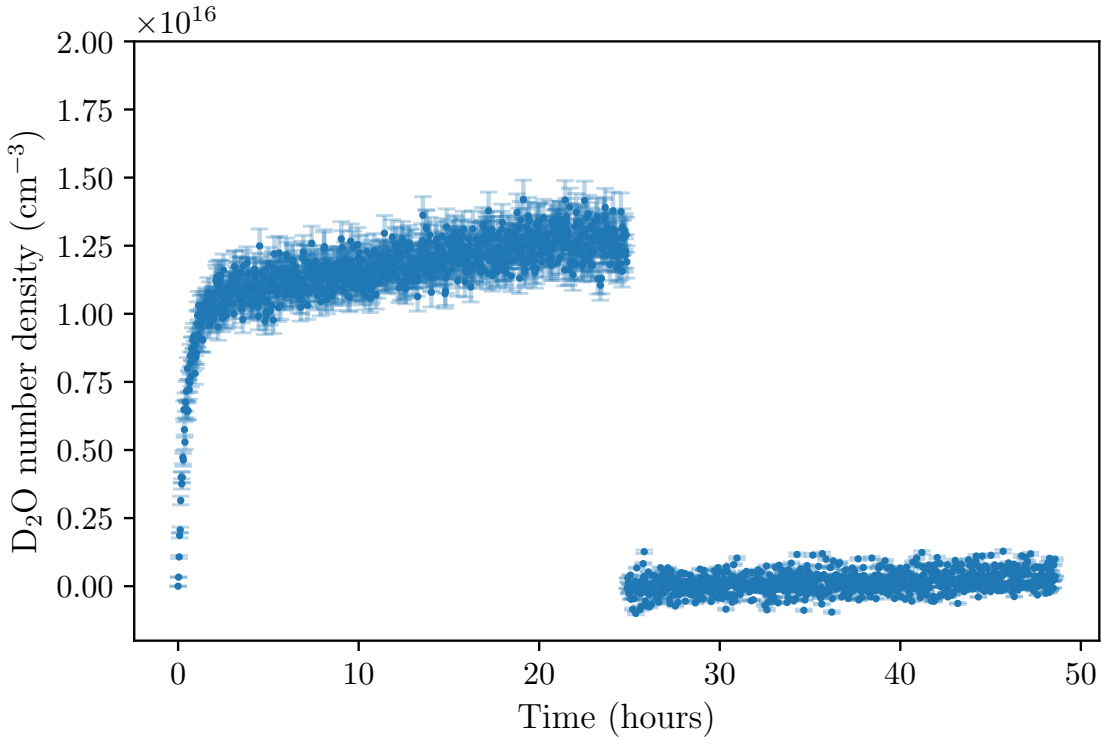

Figure 4.17: Production of D_2O from gaseous deuterium after oxidising the surfaces during ozone exposure. After 25 hours, the system was evacuated and refilled with fresh deuterium from the gas cylinder. After that, only a residual quantity of heavy water was produced.

showed a rapid increase for the first two hours, followed by a slow linear increase for almost another day. This way, about 500 ppm, corresponding to 10 µmol of D_2O in total, formed. At the 25 hours mark, the gas was exchanged with fresh deuterium from the gas cylinder, after which only a minor amount of D_2O was produced.

This observation hints towards a potential caveat of the UV/ozone method: the oxidation of metallic surfaces with the possibility of subsequent recontamination. Ozone not only reacts with contaminants, but it also oxidises the surfaces themselves. In this case, the vacuum system is primarily made of stainless steel, but it also includes copper from the gaskets. Solovey et al. (2021) report the growth of a 3 – 4 nm thick passivating oxide layer on copper during UV/ozone exposure, leading to the formation of CuO, which is also commonly used to convert hydrogen gas to its liquid phase by oxidation. The absence of D_2O production in Figure 4.17 after the gas was exchanged is consistent with fully reducing the surfaces again, leaving behind the pristine copper. This process can be repeated, which means the next time the surfaces come into contact with deuterium, small amounts of D_2O will form that can deposit on the surfaces. To determine the extent to which the stainless steel contributes to this effect, gold-coated copper gaskets should be used.

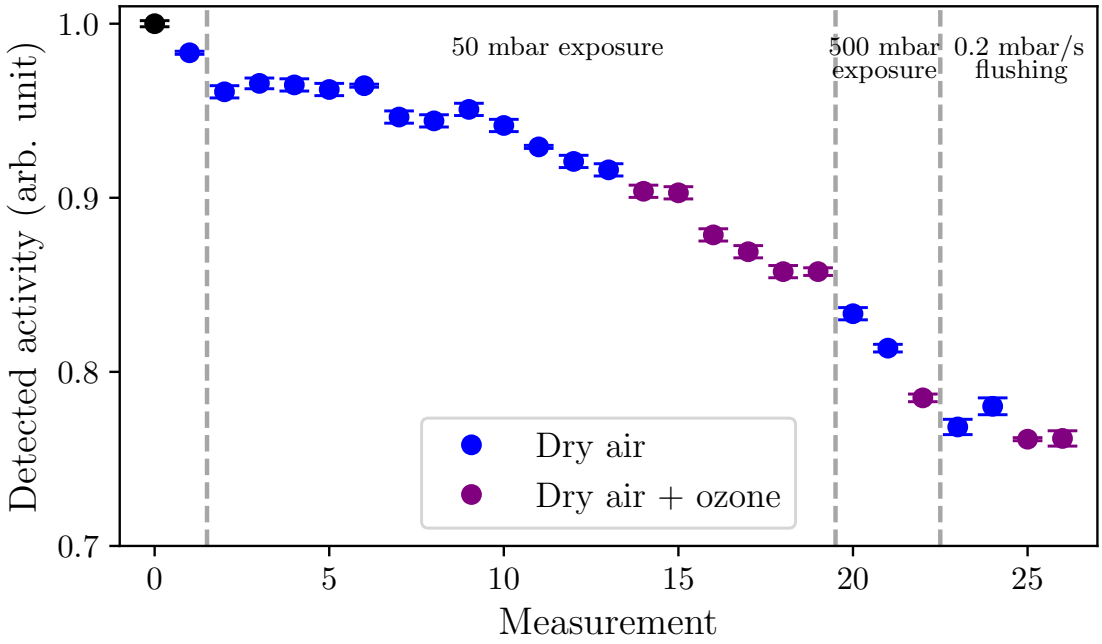

(a) Tungsten

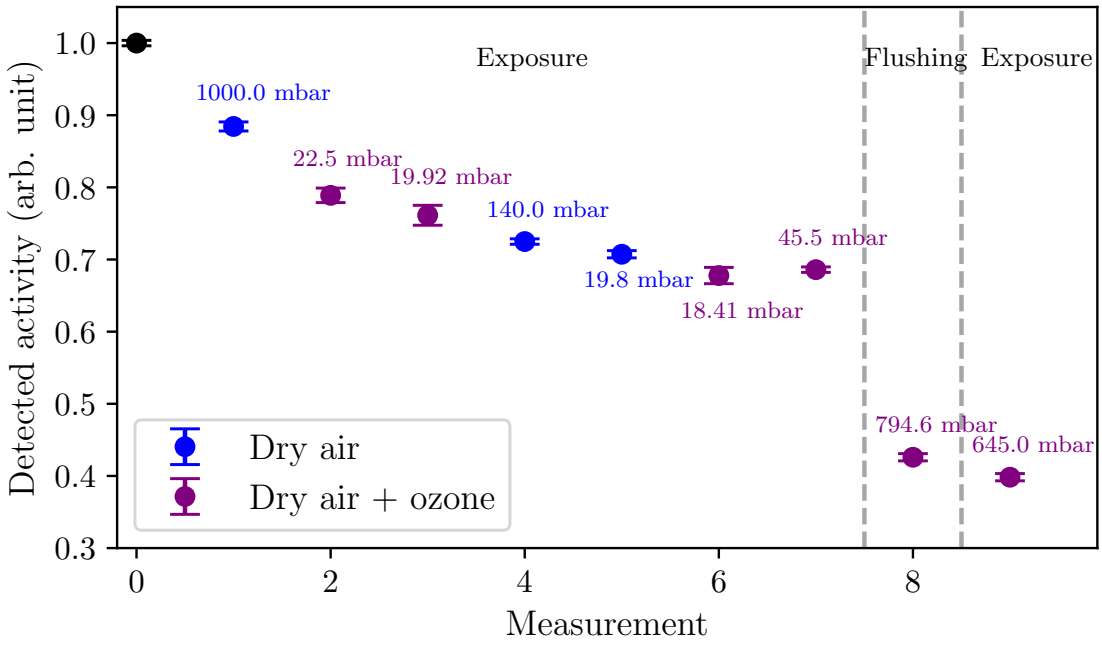

(b) Beryllium

Figure 4.18: Decontamination endeavours of tungsten (a), and beryllium (b) using only dry air (blue) and dry air containing ozone (purple). The y-axis represents the surface activity measured with BIXS. The labels denote the pressures that were applied prior to obtaining the individual data points.

4.8 Decontamination of tritiated surfaces

From previous KATRIN-related studies (Aker et al., 2024; Aker, 2025), it is clear that the combination of UV radiation and ozone is an efficient method for tritium decontamination. What is not clear, however, is if the UV radiation is required purely for ozone production, or if it also plays a role in the desorption mechanism (see section 4.3). To disentangle both effects, tritiated samples were exposed to ozone in dry air alone. As an additional test on the effectiveness of ozone, exposures to ozone-free dry air were performed as well. The samples were installed in the TRACE setup located in a glove box (for more details, see subsection 5.2.2), allowing for near-surface activity measurements with BIXS. An ozone generator similar to the UVO experiment (section 4.4) was connected to the sample chamber via a metal hose, through which ozone could be transported (section 4.6), while isolating the sample from UV radiation.

Figure 4.18 shows the decontamination attempts using dry air with and without ozone, performed on tungsten and beryllium samples as part of a master's project,[3] with the normalised surface activity on the ordinate. The first data point, coloured in black, indicates the starting activity. The labels of the data points report the pressure of the decontaminating gas in the sample cell. After the pressure was reached, the gas was left in the chamber for 20 min (Batzler et al., 2024) to interact with the sample surface, followed by a 40 min lasting evacuation period during which the activity was measured. For the blue data points, dry air taken from the glove box was used, and for the purple ones, dry air containing ozone due to prior UV irradiation. The pressure in the ozone generator was kept at (850 – 1000) mbar, resulting in an ozone concentration of about 400 ppm within (subsection 4.5.1). According to Figure 4.16, it is assumed that after the gas expansion, the ozone concentration above the samples was about 200 ppm.

By repeating the procedure of exposure followed by evacuation, it was possible to remove 25% and 60% of the surface activity of the tungsten and beryllium samples, respectively. There are in principle two reasons which could be responsible for the decontamination effect: ozone exposure and the initial flushing effect from the gas expansion. However, judging by the rate reduction after the individual exposures, no clear distinction could be made between the presence or absence of ozone at any pressure. This is especially evident from the tungsten data, for which the BIXS rate decreases after multiple exposures with 50 mbar of dry air. Even when including ozone, the slope of the activity decline did not change. At a higher pressure of 500 mbar the activity could be reduced at a slightly higher rate. Continuously flushing the sample cell did not have any significant influence on the activity of tungsten at all. Strikingly, continuously increasing the pressure above the beryllium sample with ozone-containing dry air had a major effect, with a desorption of 38% of the current surface activity. The reason for this is unknown, in particular if it was achieved by the prolonged flushing or by the continuous resupply of ozone.

Under the assumption that ozone was the dominant factor, the total exposure time of 40 minutes, including flushing, should be considered. During the following evacuation, the

[3] Elizabeth Paine, "In-situ Tritium Contamination and Decontamination of Fusion Relevant Materials", Master's thesis, IAP-TLK, 2025

removed activity corresponds to (4.68±0.50) MBq according to BIXS, or $(2.63\pm0.28)\cdot10^{15}$ tritium atoms. Estimating an ozone concentration of (200±100) ppm based on Figure 4.16, $(2.98 \pm 1.49) \cdot 10^{17}$ ozone molecules passed the sample surface over the course of the exposure. Based on this calculation, effectively 100 ozone molecules were needed to remove a single tritium atom from nearby surfaces.

During the first RW decontamination in KATRIN, the first phase of applying UV/ozone resulted in an activity decrease of 20.6% after 200 minutes (see Appendix F). Considering the vastly different geometry of the system, the efficiencies of the decontaminations in KATRIN and TRACE are comparable.

4.9 Conclusions

In order to better understand the UV/ozone decontamination method and to optimise its applications, the UVO experiment was designed, commissioned and calibrated. Key questions on fundamental properties of ozone could be answered. With this knowledge, the surface activity of a tritiated beryllium sample could be reduced by 60% in the pre-existing, modified TRACE setup. The major achieved results can be summarised as the following:

1. The production and lifetimes of ozone within a vacuum system are in the order of 10 minutes at 1 bar with an equilibrium concentration of around 460 ppm. All of its properties are linearly proportional to the absolute pressure, which hints towards ozone-surface interactions being the dominant destruction mechanism.

2. Despite the highly reactive nature of ozone, it is possible to transport it within a vacuum system, even through valves. In this system, the ozone concentration at the destination located 40 cm from its origin was half of its initial value. It is suspected that the Reynolds number of the gas flow, e.g. ozone molecules interacting with the walls due to turbulences, has a major influence on the transporting distance and efficiency (McClurkin & Maier, 2010). However, dedicated measurements are required in the future for confirmation.

3. In early stages of the experiment, an increase of gas-phase CO_2 up to a concentration of 200 ppm could be observed whenever ozone was produced and maintained. This phenomenon hints towards the depletion of carbon from the vessel's stainless steel surfaces, analogously to the formation of tritiated methane when introducing tritium gas into new vacuum systems (Morris, 1977; Gill, 1980; Dickson, 1990). UV/ozone cleaning of setups prior to commissioning with tritium appears to be a suitable conditioning method to prevent the generation and subsequent processing of tritiated methane.

4. Oxidising metallic surfaces during UV/ozone exposure was identified as a potential drawback of the decontamination method. Introducing deuterium into the system after ozone measurements resulted in the formation of D_2O – in case tritium were

used it would have been tritiated water. With an estimated surface area of 400 cm^2, 10 µmol formed.

5. Combining and applying the previously mentioned results enabled the decontamination of tritiated tungsten and beryllium samples in the absence of UV radiation. By repeatedly expanding dry air with and without ozone, a total of 25% and 60% of their initial surface activity could be removed. The largest reduction was achieved with the beryllium sample after an exposure to ozone at almost 800 mbar, which desorbed 38% of the current activity over the course of 40 minutes of exposure time. This was comparable to the efficiency of the UV/ozone decontaminations of the KATRIN RW (Aker et al., 2024; Aker, 2025). During this measurement, in the order of 100 ozone molecules per desorbed tritium atom were required. However, it is not yet possible to conclude whether the decontamination effect stems from the presence of ozone or the flushing effect from the gas expansion.

To conclude, although a marked decontamination effect using dry air and ozone was achieved, for a complete understanding of the underlying mechanism, measurements including UV radiation are required for comparison. A redesign of the system to do exactly that is currently in progress and will be available in the near future.

Chapter 5

Qualification routine for alternative Rear Wall materials

As shown in chapter 3, one way to reduce electron backscattering on the Rear Wall (RW) is to exchange it for a material with lower nuclear charge. Any potential material must first be examined for its suitability given the experimental framework. This procedure includes investigating surface contamination by tritium exposure, and exposing it to ultraviolet (UV)/ozone for potential decontaminations. In this chapter, the requirements of alternative RW materials for Tritium Investigation on Sterile to Active Neutrino Mixing (TRISTAN) phase II, such as tritium compatibility and UV/ozone resilience are established (section 5.1) and the experimental qualification strategy within the possibilities of Tritium Laboratory Karlsruhe (TLK) is presented (section 5.2). This testing procedure was applied to beryllium, and first results of its performance as an alternative material are shown and discussed (section 5.3), concluded by a preliminary verdict on its suitability.

5.1 Requirements towards a new RW material

As the RW is located at the end of the windowless gaseous tritium source (WGTS), it is subject to certain conditions, e.g. high vacuum with a pressure of $< 10^{-5}$ mbar (Aker et al., 2024), magnetic fields of 1.26 T, and tritium exposure (Aker et al., 2021a). This leads to a set of requirements towards alternative RW materials, which are also expected to hold for TRISTAN measurements:

- Low backscattering probability
- Mechanical stability
- Tritium compatibility
- Non-magnetic
- Tolerance for elevated temperatures
- UV/ozone resilience
- Electrically conductive surface
- Homogeneous work function (?)

The individual requirements are described in more detail in the next few subsections. Some of these can be combined into higher level properties.

5.1.1 Low backscattering probability

As already mentioned, and shortly demonstrated in chapter 3, electron backscattering from the RW is expected to be the dominant systematic effect for TRISTAN measurements (Descher, 2024). A material's backscattering probability is therefore the most important criterion for initial consideration as an alternative.

5.1.2 Tolerance for elevated temperatures

To be able to bake out the RW to remove residual humidity from its surface, the material should be unaffected by higher temperatures. During the decontaminations, the RW was heated to a temperature of 165 °C (Aker et al., 2024; Aker, 2025). Since increased temperatures accelerate chemical reactions, they might also reduce the time required for the UV/ozone decontamination.

5.1.3 Mechanical stability and UV/ozone resilience

During operation, and also after possible UV/ozone decontaminations, the RW's structural integrity, as well as its surface must remain intact. This is not generally the case for all materials. After exposing aluminium to UV/ozone, Vig (1985) found white powder in their setup, which was suspected to be aluminium oxide. Hence, applying UV/ozone decontaminations to non-resistant materials should be avoided at all costs. Loose particles stemming from the RW in the vacuum system could damage the turbo-molecular pumps. Substantial changes of the RW surfaces might also have a negative impact on the magnetic field coupling and surface potential.

5.1.4 Tritium compatibility

Tritium compatibility encompasses both chemical inertness with respect to tritium and low tritium accumulation during operation. These properties are interconnected. For example, a RW made of nickel would be unsuitable, since nickel is used in industry as a catalyst for hydrogenation (De et al., 2016; Shi et al., 2019; Barrero et al., 2024). During tritium circulation, tritiated hydrocarbons would form on the RW surface at an accelerated rate. Another issue is that a large tritium uptake could lead to the necessity for multiple instances of a UV/ozone cleaning, which might not be generally possible.

5.1.5 Electromagnetic properties

Since the RW is used to control the electrons' starting potential inside the WGTS via a magnetic field, electrical conductivity, as well as magnetic field compatibility was required for standard Karlsruhe Tritium Neutrino (KATRIN) measurements (Schönung, 2016). Some materials, e.g. beryllium, naturally possess an insulating oxide layer. UV/ozone

exposure could animate the formation or growth of such a layer. An oxide layer might lead to charge-up effects due to β-electron bombardment, which could propagate to the source potential if the plasma coupling to the RW is sufficiently strong. However, due to the significantly lower column density during the TRISTAN measurements, it is unclear how large the influence of RW charge-up on the source potential would be, and how it would impact the detected spectrum. Nevertheless, a material's susceptibility to charge up during tritium operation should be quantified beforehand to not encounter potential issues after restarting the measurements with a new RW for TRISTAN phase II.

5.2 Measurement routine to test materials for their suitability

In view of the aforementioned requirements towards new potential RW candidates, the following set of measurements is proposed:

- Surface activity evolution by tritium gas exposure
- UV/ozone resistance by ozone exposure
- Decontamination effectiveness
- Surface characterisation using Auger electron spectroscopy (AES)

The first three measurements can be conducted with the systems available at TLK. With the ultra-violet ozone (UVO) setup (subsection 4.4.2), it is possible to expose samples to ozone under UV irradiation. Afterwards, the sample can be checked for surface changes, either by eye or any arbitrary imaging technique. AES (subsection 5.2.1) was identified as a suitable method to characterise the sample surface regarding charge-up effects. Tritium accumulation, as well as decontamination, can be investigated with the pre-existing Tritium Activity Chamber Experiment (TRACE) (subsection 5.2.2), which was equipped with an ozone generator based on the UVO setup.

5.2.1 Surface characterisation using Auger electron spectroscopy

To obtain information on the quantities of interest presented previously, AES (Chang, 1971; Shimizu, 1983) is a promising analytical method for probing surfaces. AES works by bombarding the surface with electrons, and measuring the emitted Auger electrons. Since these typically have very low energies (see subsection 3.3.1), it is a surface-sensitive method. Due to the initial electron bombardment, the surface will charge up if an insulating oxide layer is present. When analysing beryllium oxide with primary electron energies of 1 keV, Musket (1989) found that the surface was charged to +12 V, seen as a shift in the energies of the Auger electrons. Although a nuisance in their study, this effect can be harnessed to check for the material's surface potential, and changes thereof after UV/ozone exposure. Additionally, AES yields information about the chemical composition of the sample surface, which can be used to quantify how efficiently UV/ozone

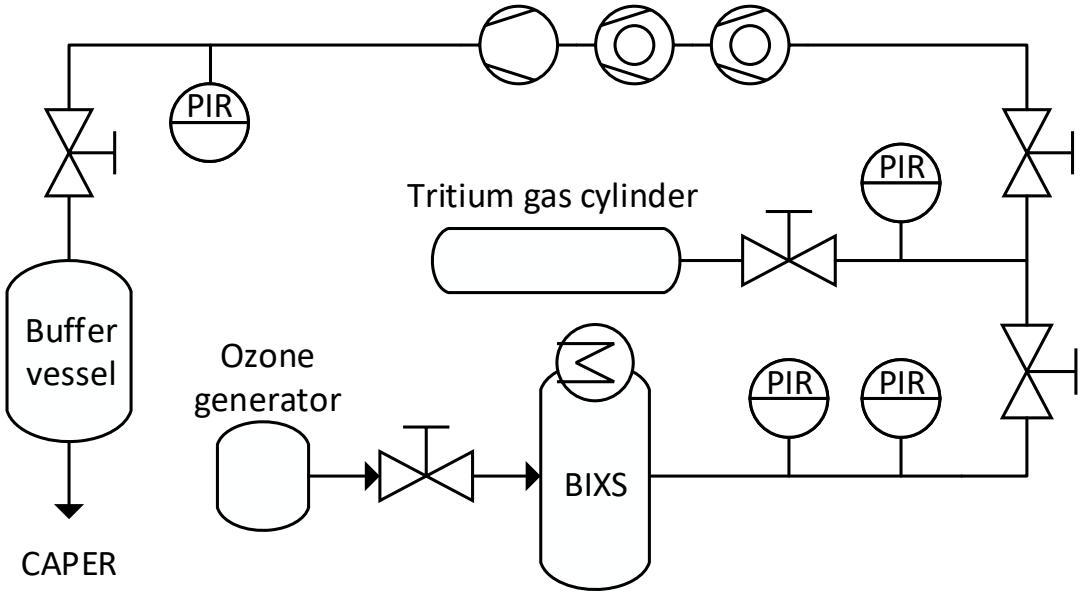

Figure 5.1: Simplified flow chart of the TRACE setup used to expose the beryllium samples to tritium. The samples are loaded and measured in-situ in the vessel labelled "BIXS". With the ozone generator directly connected, it is possible to introduce ozone into the vessel and measure its decontamination effect.

cleaning removes the carbon from surfaces (Musket, 1989). This is especially interesting as complementary information, since tritium adsorption can be strongly influenced by the carbon content (Aker, 2025). TLK currently does not possess a facility to perform AES measurements. Hence, these have to be conducted elsewhere, which eliminates the possibility to also measure tritiated samples.

5.2.2 Tritium contamination and decontamination with the TRACE setup

Tritium accumulation of the RW during operation can be simulated using the TRACE setup (Batzler et al., 2025). With this setup, it is possible to expose solid samples with a diameter of up to 38 mm to high-purity tritium. The near-surface activity of the sample can be measured continuously using beta-induced X-ray spectrometry (BIXS) (Matsuyama et al., 1998; Röllig, 2015). Similar to KATRIN, the beryllium window separating sample and X-ray detector is gold-coated to increase the generation of bremsstrahlung. Figure 5.1 shows a simplified flow diagram of the setup. The sample is located in the measurement cell labelled "BIXS", which is equipped with a heating sleeve for bake-out.

When comparing the tritium uptake measured with TRACE to the activity accumulated by the RW, some factors have to be considered. For example, the increased electron

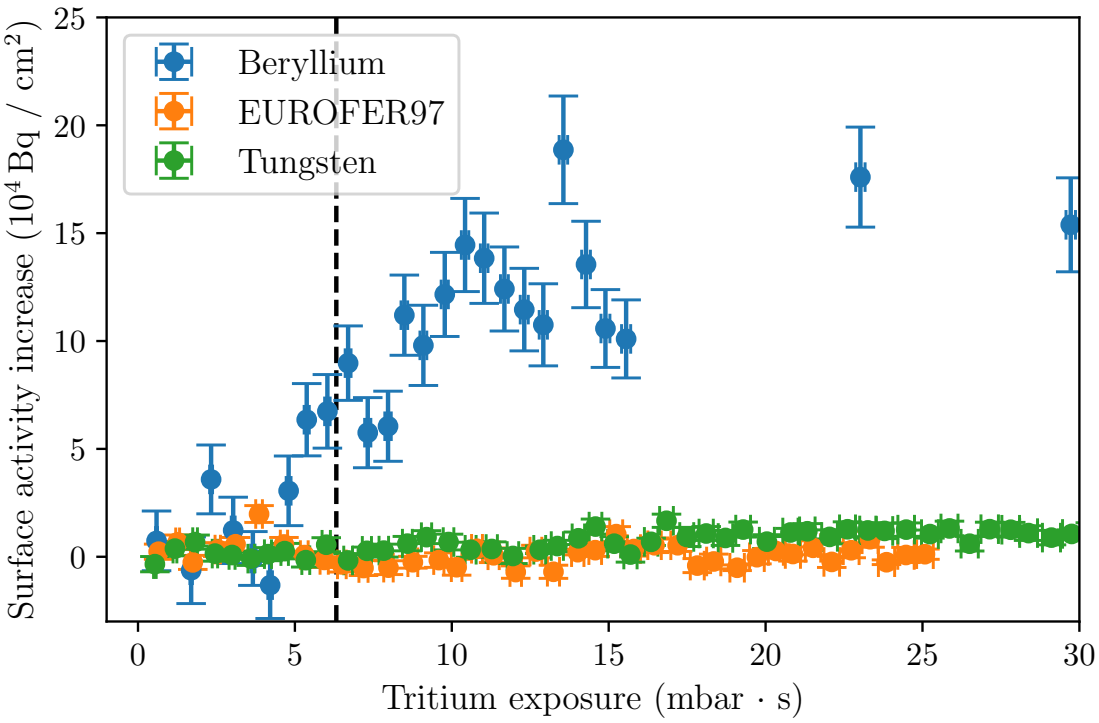

Figure 5.2: Surface activity increase of low (Be), intermediate (EUROFER97), and high (W) Z materials, measured with BIXS. The dashed line indicates the tritium exposure corresponding to two years of TRISTAN measurements. Out of the three materials, beryllium accumulated the most tritium.

and ion flux impinging on the RW due to magnetic field lines cannot be replicated. Because of the small volume of the TRACE setup, it is also not feasible to work with pressures as low as that at the RW. The tritium partial pressure close to the RW during KATRIN operation is of the order of $\leq 10^{-5}$ mbar (Aker et al., 2024). Assuming linear scaling with column density, this would correspond to lower than 10^{-7} mbar for TRISTAN measurements. Instead, with TRACE tritium pressure and exposure time are selected such that their product equals that in KATRIN. For the samples, a tritium pressure of 10^{-3} mbar is chosen, which ensures a molecular flow within the vessel. With an exposure time of 10 min per cycle, this corresponds to an exposure of 0.6 mbar·s, which is equivalent to roughly 70 days of KATRIN operation at 1% column density. After exposing the sample to tritium, the cell is evacuated for at least an hour, during which the surface activity is measured with BIXS. Calculating the mean count rate above a threshold energy of 0.7 keV yields a scalar value that is directly proportional to the near-surface activity. By introducing a known amount of tritium and measuring the resulting BIXS signal, the count rate is calibrated against absolute activities. The process of filling the cell with tritium and subsequent evacuation is repeated multiple times.

Since BIXS is sensitive to X-ray generation, the procedure was calibrated using three materials with high, intermediate, and low nuclear charges, namely tungsten ($Z = 74$), EUROFER97 ($Z \approx 26$), and beryllium ($Z = 4$), respectively, over the course of two bachelor's and a master's theses.[1,2,3] Apart from beryllium, the samples were polished and thoroughly cleaned with an ultrasonic bath. Figure 5.2 shows these materials' rise of activity per surface area during exposure to tritium. Adhering to the planned duration of the keV-scale sterile neutrino measurement phase, the dashed line indicates an equivalent exposure of two years. At this exposure, beryllium accumulated by far the most tritium, which is further investigated in section 5.3. EUROFER97 on the other hand, a type of reduced activation steel (Tavassoli et al., 2004; Gaganidze et al., 2018) for fusion applications (Schumacher, 2001; Kikuchi, 2012), did not retain significant amounts of tritium detectable with BIXS at any point in time. After the measurements were concluded, the samples were removed from the TRACE setup and decontaminated using de-ionised water in an ultrasonic bath. Determining the tritium content in the water with liquid scintillation counting (see Appendix G) confirmed the plausibility of the activities extracted with BIXS.

The capabilities of the TRACE setup to perform tests on in-situ decontamination of the samples using ozone were already demonstrated in section 4.8, Figure 4.18.

5.3 First qualification of beryllium as a new RW material

With the measurement routine to check materials for their suitability as RW alternatives established, beryllium as the prime candidate was tested for UV/ozone resistance, tritium accumulation and decontamination, as reported in the following sections.

5.3.1 Measurement of tritium accumulation of beryllium with TRACE

With the TRACE setup, three beryllium samples were exposed to gaseous tritium to replicate the activity build-up of a beryllium RW during TRISTAN measurements. Due to the high transmissivity of beryllium to X-rays (Henke et al., 1993), a sample thickness of 10 mm was chosen to prevent measuring activity below the sample.

Figure 5.3 displays the background-corrected count rate evolution over cumulative tritium exposure. All samples showed a linear increase in surface activity, each with a lower slope than the previous one. The reason for this is not entirely clear. Most of the components within the detector's field of view were new, so the increased adsorption once they got into contact with tritium and their gradual saturation could be a possible reason. To set an upper limit on the expected RW activity, only sample 1 will be considered, since this showed the largest count rate increase. After the exposure corresponding to two

[1] Dylan Roodt, "Untersuchung des Tritiumsorptionsverhaltens einer elementaren Wolframprobe mittels Beta-induzierter Röntgenspektrometrie", Bachelor's thesis, IAP-TLK, 2024

[2] Philipp Haag, "Characterization of beryllium with respect to tritium accumulation as an alternative material of the KATRIN rear wall", Bachelor's thesis, IAP-TLK, 2024

[3] Elizabeth Paine, "In-situ Tritium Contamination and Decontamination of Fusion Relevant Materials", Master's thesis, IAP-TLK, 2025

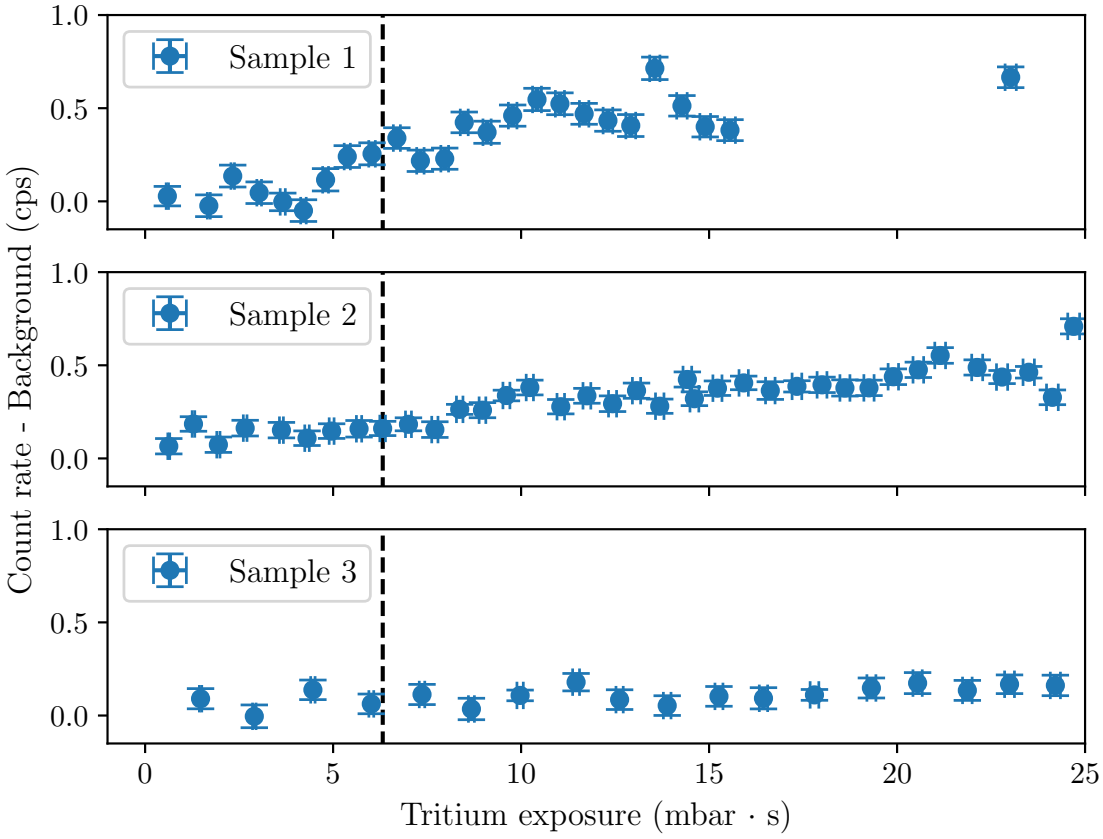

Figure 5.3: Background-corrected BIXS rates of beryllium samples after periodic tritium exposure. The dashed line represents two KATRIN years with tritium operation at 1% column density.

KATRIN years, a rise in count rate of (0.255 ± 0.059) cps was measured. The uncertainty on the BIXS rate was calculated according to Poisson statistics.

For beryllium and this system's geometry, the conversion factor from count rate to activity was determined to be $(2.64 \pm 0.27) \cdot 10^5$ Bq /cm^2/cps, with the dominant uncertainty stemming from the sample cell's volume. For the BIXS rate increase of sample 1, this yields a surface activity of $(6.7 \pm 1.7) \cdot 10^4$ Bq / cm^2 after two years of TRISTAN measurements. A regular-sized RW with a diameter of 14.5 cm would accumulate (11.1 ± 2.8) MBq in total, or (1.11 ± 0.28)% relative to a source activity of 10^9 Bq. This value should serve as a preliminary upper limit for the RW activity after two years of tritium operation without any UV/ozone decontaminations. It is only valid under the assumptions of neutral tritium being the dominant contamination mechanism of the RW and that the impact of the different pressure used in the TRACE setup is negligible. While these may not necessarily be true, a beryllium RW will be expected to accumulate tritium linearly over time, as determined in this study. To narrow down the magnitude of adsorbed activity further,

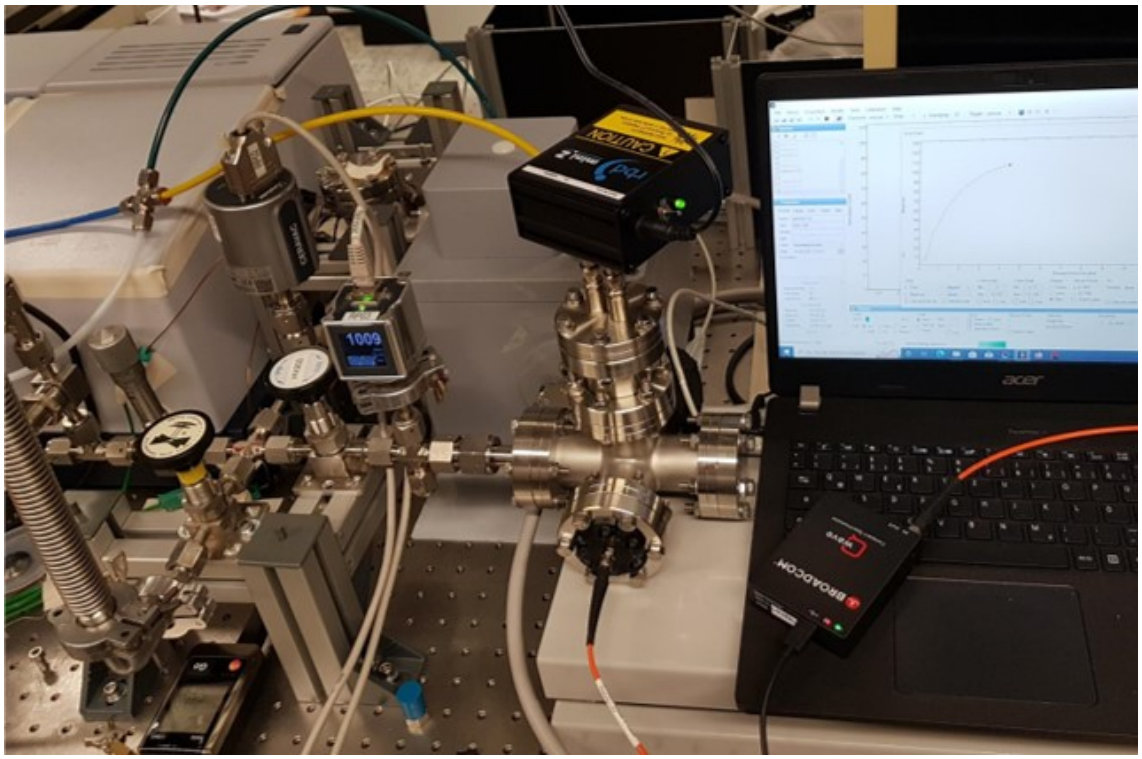

Figure 5.4: Setup used for the first exposure of beryllium to UV/ozone, which can be decoupled from the UVO experiment in case of contamination with beryllium dust. Only the gas supply is shared.

more beryllium samples will need to be measured. Should the reported upper limit of $(1.11 \pm 0.28)\%$ of the source activity already be too high, or should beryllium accumulate more tritium than expected, it is necessary to identify if UV/ozone decontamination can safely be applied.

5.3.2 UV/ozone resilience of beryllium

With beryllium being a hazardous material, which is especially toxic as powder, it is also crucial from a safety standpoint to prevent the formation of beryllium dust. Hence, making sure that all the samples maintain their solid form while being treated with UV/ozone is of utmost importance. The UVO setup, described in chapter 4, can also be employed for exposing solid samples to ozone at well-defined concentrations. However, since powder formation due to oxidation could not be ruled out initially, the first beryllium sample was exposed to ozone in a side chamber (see section 4.6) to prevent potential contamination of the remaining setup. It was equipped with multiple windows for optical checks of the beryllium sample, which was done regularly to plan the next steps. Beryllium oxide possesses a white colour, making visual identification possible. To confirm the generation of ozone, a UV spectrometer was connected (subsubsection 4.4.3.2).

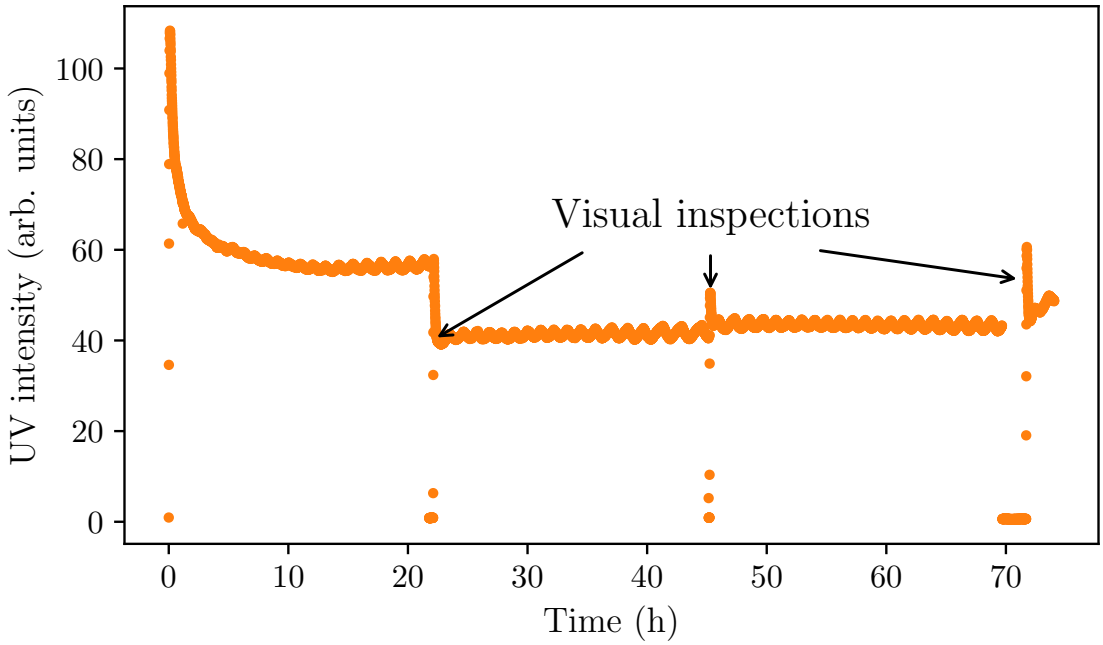

Figure 5.5: UV intensity during the first exposure of beryllium to ozone. The drops to zero indicate breaks for visual inspection of the sample, during which the UV source had to be turned off. After switching on the UV source, the intensity decreases again after some time due to ozone generation. The lab's air conditioning cycles led to slight oscillations in the intensity.

The first beryllium sample was exposed to ozone for around 75 hours, which is 50% longer than the duration of the first RW decontamination and hence an appropriate amount of time for the first test. The UV intensity is displayed in Figure 5.5, which is an indicator for the ozone concentration, as demonstrated in section 4.5. For visual inspection of the beryllium sample, the UV source was switched off, which leads to the intensity dropping to zero in the graph. The decrease in intensity after switching on the UV source again proved the presence of ozone. During and after ozone exposure, the sample surface viewed through the windows appeared to be unchanged. The side chamber was detached, transferred to a fume hood and carefully disassembled. All components, including the beryllium sample, were closely examined for any traces of dust. Tests included wiping the inner surfaces with wetted paper towels to coagulate potential dust particles, and rinsing them with water which was collected and also examined. No signs of beryllium oxide or powder were found and the surfaces of both sample and vacuum components remained in pristine conditions.

The beryllium sample exposed to ozone, as well as an untreated sample, were examined using an electron scanning microscope (Figure 5.6). Both surfaces appear to be identical,

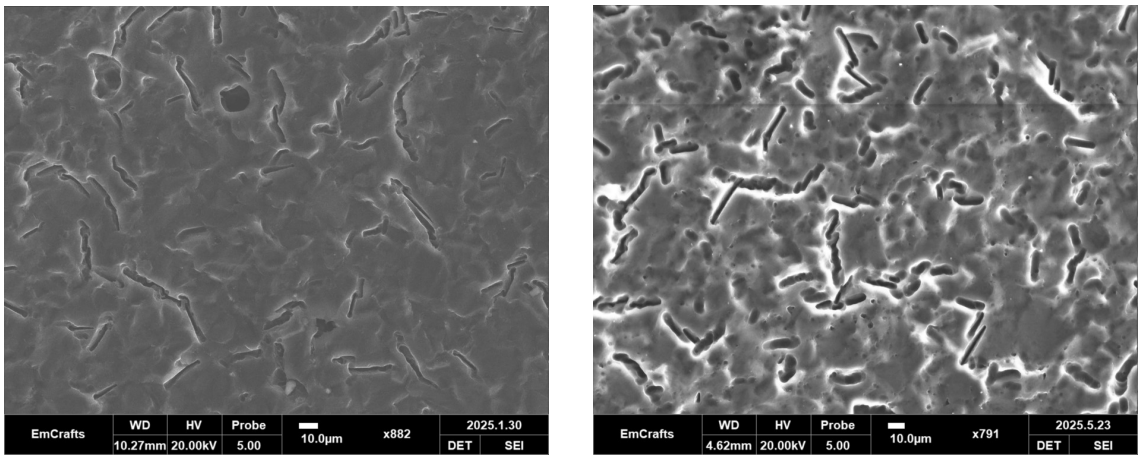

(a) before (b) after

Figure 5.6: Images of two different beryllium samples before (a) and after (b) ozone exposure, taken with a scanning electron microscope. Apart from the contrast, no changes in surface morphology were identified.

and grains of beryllium dust were not detected, which permits the conclusion that the beryllium was unaffected by the ozone.

A second beryllium sample was installed in the UVO setup such that the Fourier transform infrared (FTIR) spectrometer (subsection 4.4.3) measured the ozone concentration just above the sample surface. The distance between the sample surface and the UV source was about a tenth of the distance between the UV sources and the RW in KATRIN. To conserve the UV intensity irradiating the beryllium according to the Beer-Lambert law, a pressure of 1000 mbar for the UV/ozone treatment was chosen, which is ten times higher than during the previous RW decontaminations. The second sample was exposed to ozone for about 120 hours, corresponding to roughly two RW cleanings at KATRIN. Figure 5.7 shows the ozone concentration just above the sample surface, which was greater than 400 ppm for the entire duration. As seen through the viewport, the surface of the second beryllium sample was unaffected by the prolonged ozone exposure. This sample is planned to be investigated with AES measurements, for which the planning is ongoing. Nevertheless, the experience in beryllium handling and ozone exposure gained in these first tests is a good base to safely apply the decontamination to a tritiated beryllium sample with TRACE.

5.3.3 In-situ decontamination of beryllium using ozone

A tritiated beryllium sample was exposed to dry air with and without ozone, after which the recipient was evacuated to measure the activity with BIXS, as explained and briefly presented in section 4.8. Figure 5.8 once again displays the beryllium's surface activity after the individual exposures, which is inspected more closely. The initial drop in activity by roughly 10% was a result of connecting the ozone generator, for which a vacuum

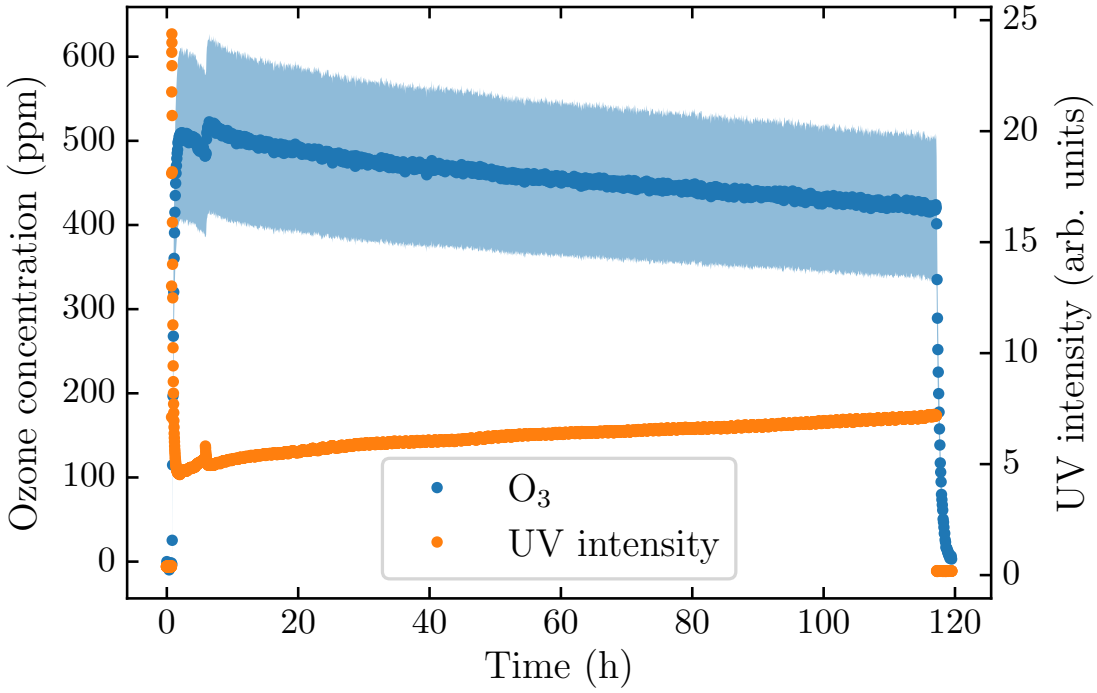

Figure 5.7: UV intensity and ozone concentration directly above the beryllium sample surface in the UVO setup. A long-term intensity drift of the UV source leads to a gradual decrease in ozone concentration.

connection to the sample cell was opened. Breaking the vacuum caused a sudden pressure increase to ambient pressure, which lowered the activity similar to gas flushing. Measurement 2 was conducted after exposing the sample to 22.5 mbar of ozone-containing air, which had the same effect in magnitude. Over the next four exposures, a linear decrease by another 10% in surface activity was observed. For these measurements, both air and ozone were used twice. Judging from the activity decrease, these two methods could not be distinguished. The eighth exposure resulted in a considerable decontamination of 26% of the initial activity. For this measurement, ozone-containing gas was used at an elevated pressure of almost 800 mbar for the first time. To minimise the kinetic influence of the gas flow on the sample surface, the expansion was executed over the course of half an hour. For this measurement, only 10 minutes of static exposure were spent. A second high-pressure exposure to ozone followed, but this time, the pressure of 645 mbar was reached after a couple of seconds. However, only 3% of the initial activity could be removed this way. Due to experimental boundary conditions, the decontamination was concluded. In total, about 60% of surface activity could be removed from the detector's field of view. Although it has not yet been identified whether the decontamination was achieved due to the ozone or a flushing effect, the data suggests that it is generally possible to decontaminate beryllium

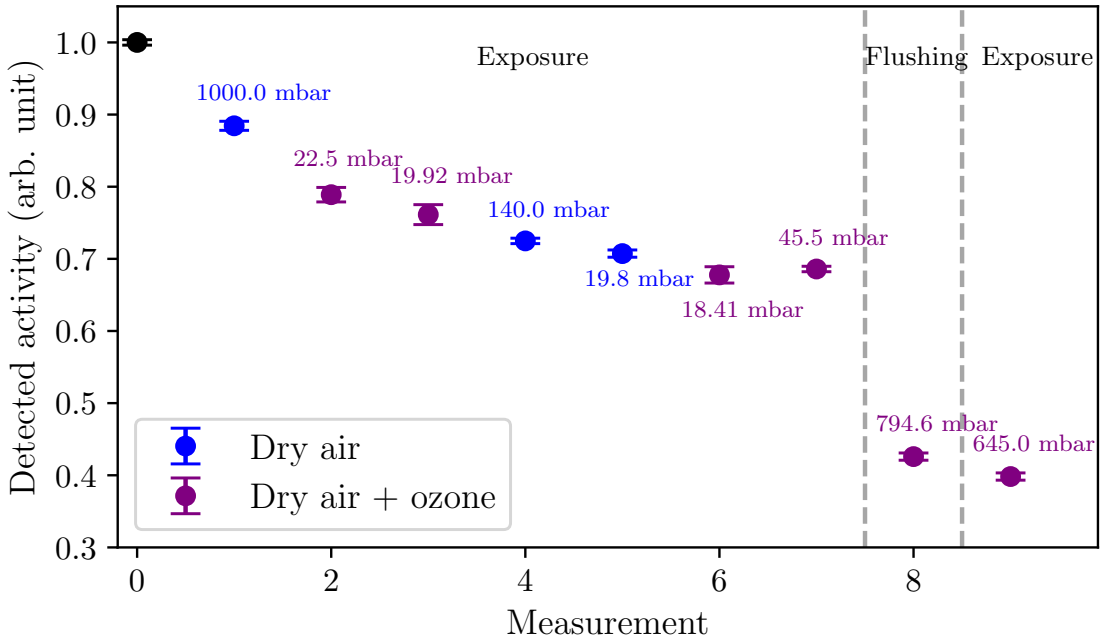

Figure 5.8: In-situ decontamination of a beryllium sample in TRACE using dry air (blue) and dry air containing ozone (purple). The eighth measurement, in which the pressure was slowly increased over 30 minutes, showed the largest effect.

in-situ. Removing the beryllium from the sample cell revealed no visible changes occurred due to ozone exposure, as expected from previous tests (subsection 5.3.2).

5.4 Further potential measurements

The results discussed in this chapter should serve as a first experimental basis for the suitability of beryllium as an alternative RW material. More measurements on tritium accumulation are necessary, especially on alternating contamination and decontamination measurements. From the KATRIN RW one could learn that tritium accumulation during circulation can be mitigated by UV/ozone decontamination due to the gradual removal of tritiated amorphous carbon from the surface (Aker, 2025). If this behaviour were also observed for beryllium using the TRACE setup, the upper limit on the expected activity given here could be reduced even further.

Another important factor is the identification and, if so, quantification of charge-up effects stemming from the growth of the insulating oxide layer. For this, AES appears to be the perfect measurement principle. If the results from the AES measurements remained unchanged after UV/ozone exposure, a sufficiently strong resilience of the beryllium surface, especially its oxide layer, would be proven.

5.5 Conclusions

An experimental procedure to qualify alternative RW materials in view of the given requirements was developed. This includes measurements on tritium contamination and decontamination, resistance to UV/ozone exposure, as well as electrical surface potential. Apart from the electromagnetic properties, this measurement routine was tested on beryllium, resulting in a positive initial verdict on its suitability to use as a new RW. The most important findings will be summarised below.

1. The proposed qualification routine is comprehensive and covers most of the expectedly relevant RW properties, such as tritium uptake and decontamination. This set of measurements is available for any considerable RW candidate material.

2. Three pristine beryllium samples were exposed to tritium in a way that can be compared to the RW during tritium circulation at 1% column density. After an exposure equivalent of two years of TRISTAN measurements, an upper limit for the RW activity of $(1.11 \pm 0.28)\%$ of the source activity was determined for accumulation by neutral gas. This is comparable to the performance of the gold RW in KATRIN prior to its first UV/ozone decontamination (Aker et al., 2024). The limits given holds under the assumption of neutral gas being the dominant source of tritium adsorption. A guided flux of electrons and ions towards the sample surface was not replicated. All three of the beryllium samples showed a linear increase in activity. Based on these and also previous results (Röllig, 2015), a linear tritium accumulation on the RW during TRISTAN operation is expected.

3. After prolonged exposure to UV/ozone, the surfaces of two beryllium samples showed no measurable changes with the techniques available. Modifications of their oxide layer could not be determined with optical and electron microscopy. In particular, the generation of dust did not occur and the beryllium remained intact. Hence, UV/ozone decontamination of beryllium appears to be an option.

4. Exposing a tritiated beryllium sample to dry air with and without ozone reduced its surface activity. About 60% of the tritium could be removed, given the experimental boundary conditions. However, more measurements including UV irradiation are required to fully understand the cause of it.

In view of these first results, no reason to disqualify beryllium as an alternative RW material was found. However, further measurements are required to finalise this verdict. Since beryllium possesses a native oxide layer, quantifying charge-up effects or changes thereof after ozone exposure is especially important. For this task, AES is recommended. The measurement procedure presented in this chapter should be applied to micro-structured silicon, another potential RW candidate, next, and can also be utilised to identify other suitable candidates.

Chapter 6

Summary and outlook

The observation of neutrino oscillations indicates that neutrinos must possess a small mass of yet unknown value and origin, although they are presumed to be massless in the Standard Model. One explanation could be the existence of sterile neutrinos on the keV mass scale, which couple to the active neutrinos and generate their mass, as described by the seesaw mechanism.

The Karlsruhe Tritium Neutrino (KATRIN) experiment can significantly contribute to research on both frontiers. Utilising tritium β-decay from a high-luminosity windowless gaseous tritium source (WGTS) and an integrating spectrometer of Magnetic Adiabatic Collimation with Electrostatic (MAC-E) filter type, it follows a model-independent approach based on kinematics. Recently, a new world-leading upper limit from laboratory experiments of 0.45 eV has been set (Aker et al., 2025). In its current phase, the main objective is to measure the effective electron antineutrino mass with a sensitivity of better than 0.3 eV by scanning the energy region near the kinematic endpoint. After having reached its goal in late 2025, KATRIN will enter the next measurement phase to probe the β-spectrum for kink-like signatures of sterile keV-scale neutrinos in the scope of the Tritium Investigation on Sterile to Active Neutrino Mixing (TRISTAN) project. Since these could have a wide range of mass, KATRIN will use a differential measurement mode to cover most of the energy range accessible from tritium decay. To achieve the target sensitivity on the mixing amplitude of $< 10^{-6}$, both old and new systematic effects are required to be understood to successfully identify a potential ppm-level signal in the spectrum.

Two systematic effects are connected to the Rear Wall (RW), which is a stainless steel disk sputter-coated with gold that serves to control the starting potential of the electrons inside the WGTS. One of them, namely tritium accumulation on its surface, has been extensively studied in KATRIN (Aker, 2025). RW activity emerges as a secondary, superimposed β-spectrum with a shifted endpoint compared to the source tritium whose amplitude increases during tritium circulation. The second effects, electron backscattering, is expected to be the largest contribution to the uncertainty budget of the TRISTAN measurements. It is a consequence of the large region of interest entailing the majority of the β-spectrum, since electrons scattering inelastically on the RW will still be included in the detected spectrum, even with significant energy-loss.

Within the scope of this work, three major topics were identified and researched to study and mitigate RW activity and backscattering in the TRISTAN project.

Contribution to an improved modelling of RW effects

To reach the desired ppm-level accuracy on the measured spectrum, elaborate modelling efforts are being undertaken, especially with the use of the TRModel code, which calculates the detected energy spectrum. This piece of software includes systematic effects as response matrices that are applied in sequence. Both RW effects can be described with the current set of matrices. A sensitivity study on the impact of RW activity revealed that the sensitivity loss saturates at 0.1% of the source activity adsorbed on the RW surface, with minor effects below sterile masses of 10 keV. Saturation effects were also observed in different studies, which might hint towards an insufficient amount of electrons simulated in the current response matrices. For ongoing developments towards a new major version of the TRModel, an improved set of RW matrices were generated in this work. For a combination of 130,000 input energies and angles per matrix, the backscattered energy and angle distributions from a target material were simulated using a newly developed code using Geant4. These are now available for beryllium, gold, and stainless steel, each with two independent physics model packages: Penelope and Single Scattering. Multiple refinements were implemented with respect to the current datasets, like finer binning, an extended energy range up to 32.5 keV to enable krypton studies, and increased statistics by a factor of up to 280. It was possible to fulfil the statistics requirement by implementing a hybrid approach to generate, but not track low-energy secondary electrons further, which conserved simulation accuracy but increased its performance by up to 2.2. The backscattered spectra were examined for physical and computational effects. Below energies of 3 keV, the energy spectra of electrons backscattered from gold show narrow features. In this case, using the Penelope physics list creates additional discrete numerical effects that are also visible in the high-energy region. Special care is advised when using the gold dataset generated with Penelope, since both of these effects could potentially be confused with the kink-like signature of a sterile neutrino. It was highlighted that depending on the specified settings, the simulation results can significantly differ. This issue is enhanced by the experimental data listed in literature, which also show a spread on the backscattering probability of up to 0.1. In conclusion, to estimate the overall accuracy of the simulations, in-situ characterisation and calibration measurements of electron backscattering from the RW will be required.

Further understanding of UV/ozone decontamination

From KATRIN it was already proven that the RW surface activity can be removed via ultra-violet (UV)/ozone decontamination. This method is also widely used in industry to deplete surfaces of hydrocarbons in general, but there is no consensus on how this mechanism works. UV and ozone separately, but also their combination have been reported in literature to be responsible. A better understanding of the individual components is required to optimise and enable its application to tritium-containing systems in and

outside of KATRIN. Ozone was focused on in particular, for which a tritium-compatible setup – the ultra-violet ozone (UVO) experiment – was designed and commissioned. This was essential for determining the pressure-dependent ozone properties. Its production and lifetimes range from 3 to 8 minutes and 3 to 16 minutes, respectively. Their linear pressure dependence, as well as the significantly shorter lifetimes than in the atmosphere, suggest ozone is primarily destroyed on surfaces, which is ideal for decontamination. It was also demonstrated that despite the high reactivity of ozone, it is possible to transport it through narrow openings such as valves. This is a great advantage in case ozone cannot be generated at the location where decontamination is required. The already existing Tritium Activity Chamber Experiment (TRACE) at Tritium Laboratory Karlsruhe (TLK) to contaminate samples with tritium was upgraded by connecting an ozone generator similar to the UVO setup. By exposing tritiated tungsten and beryllium samples sequentially to dry air and ozone in the absence of UV radiation, it was possible to remove 25% and 60%, respectively of their surface activity. For the beryllium sample, the time constant for decontamination was similar to that of the first KATRIN RW decontamination. It could not be conclusively determined whether tritium desorption was caused by the ozone itself or a gas flushing effect.

Development of a qualification strategy for alternative RW materials

Replacing the golden RW could significantly mitigate electron backscattering. Within this project, a qualification procedure to evaluate alternative materials on the basis of the requirements from KATRIN was developed. This includes investigation on tritium accumulation and tests for UV/ozone resilience, as well as decontamination. The procedure was applied to the candidate material beryllium, chosen for its very low nuclear charge number $Z = 4$. Three beryllium samples were exposed to gaseous tritium while continuously measuring their surface activity. Based on the assumption of neutral tritium being the main contributor to the activity build-up, a linear increase of surface activity to roughly 1% of the source activity can be expected after two years of operation. From the sensitivity study from a previous chapter, RW activity with this magnitude is not anticipated to be a problem. Still, exposure of beryllium to UV radiation and ozone left the surface intact, and potential dust formation or growth of its native oxide layer could not be detected with the imaging techniques available. Together with the observed activity reduction of 60% in one of the tests, it is safe to assume that a beryllium RW could also be decontaminated should it be necessary. In conclusion, none of the results of these first tests gives a reason to exclude beryllium as an alternative RW material.

Outlook

With the new set of response matrices available, sensitivity studies on RW activity and backscattering should be revisited as soon as the TRModel update is completed for a more accurate estimation of their impact. As for the decontamination of tritiated samples with TRACE, planning of an additional upgrade which additionally enables UV irradiation is in progress. By comparing the decontamination time-scales with and without UV radiation,

it will be possible to determine the extent to which UV and ozone individually contribute to the desorption of tritium from surfaces. To check if the observation of saturating RW activity accumulation after multiple UV/ozone cleanings are also applicable, alternating contamination and decontaminations using TRACE should be performed. Regarding an alternative beryllium RW, more checks on its surface structure are crucial, especially on charge-up effects due to its oxide layer. Measurements using Auger electron spectroscopy (AES) are currently being planned. In the near future, other RW candidates will also be tested using the procedure developed in this project. Another promising candidate with an expected low backscattering probability due to its geometry is micro-structured silicon. One critical question is whether this structure is persistent under ozone exposure, or if it will oxidise and experience changes in shape. Entirely different routes for RW mitigation are being pursued as well, e.g. a major hardware change to put the new RW behind a superconducting magnet. This could magnetically reflect electrons and thus prevent inelastic scattering, as well as prevent β-electrons due to RW activity from reaching the detector.

Appendix A

Geant4 simulation macro

```
# Physics settings
/process/em/deexcitation World true true true
/process/em/fluo true
/process/em/auger true
/process/em/augerCascade true
/process/em/pixe true
/process/em/deexcitationIgnoreCut true

/run/setCut 10 nm
/cuts/setLowEdge 100 eV

# Absorber settings
/rw/det/setAbsThickness 1 mm
/rw/det/setAbsMat G4_Au

# Computational settings
/run/numberOfThreads 96
/run/initialize

#/rw/stack/killSecondaries

# Particle source settings
/gps/particle e-
/gps/energy 18.5 keV
/gps/ang/mintheta 0.000 deg
/gps/ang/maxtheta 0.000 deg

/gps/position 0 0 -9.9 cm
####################################

# Run simulation
/analysis/setFileName HistoName
/run/printProgress 50000
/run/beamOn 1000000
```

Appendix B

Electron energy spectra from sub-surface tritium

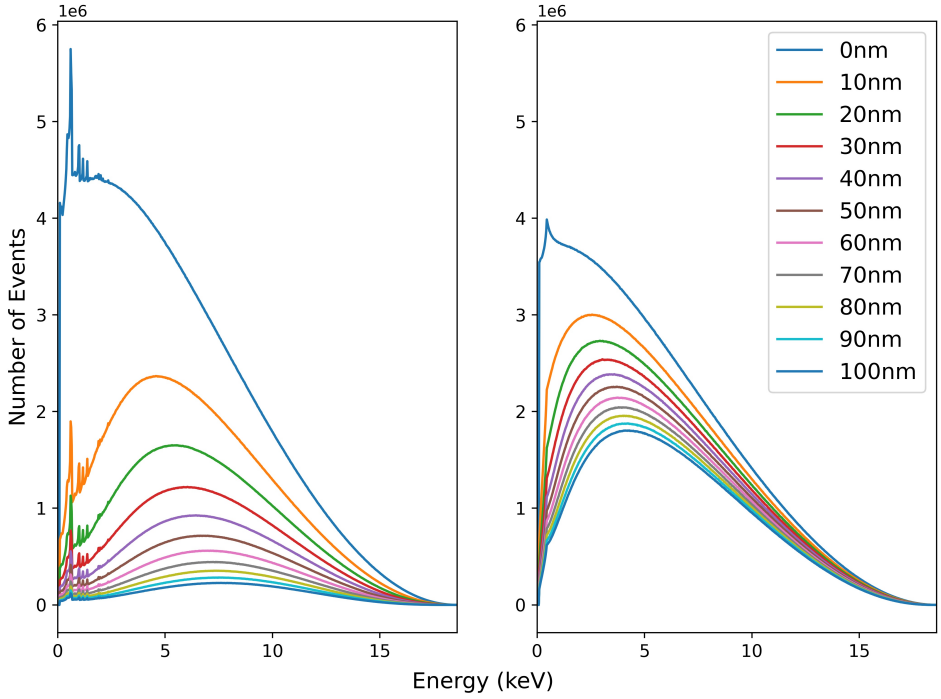

Figure B.1: Energy distribution of electrons from sub-surface tritium decay for gold (left) and beryllium (right), as visible at the surface. The length given in the legend corresponds to the depth at which the electrons are emitted.

Appendix C

Statistical Weights used for the new RW response

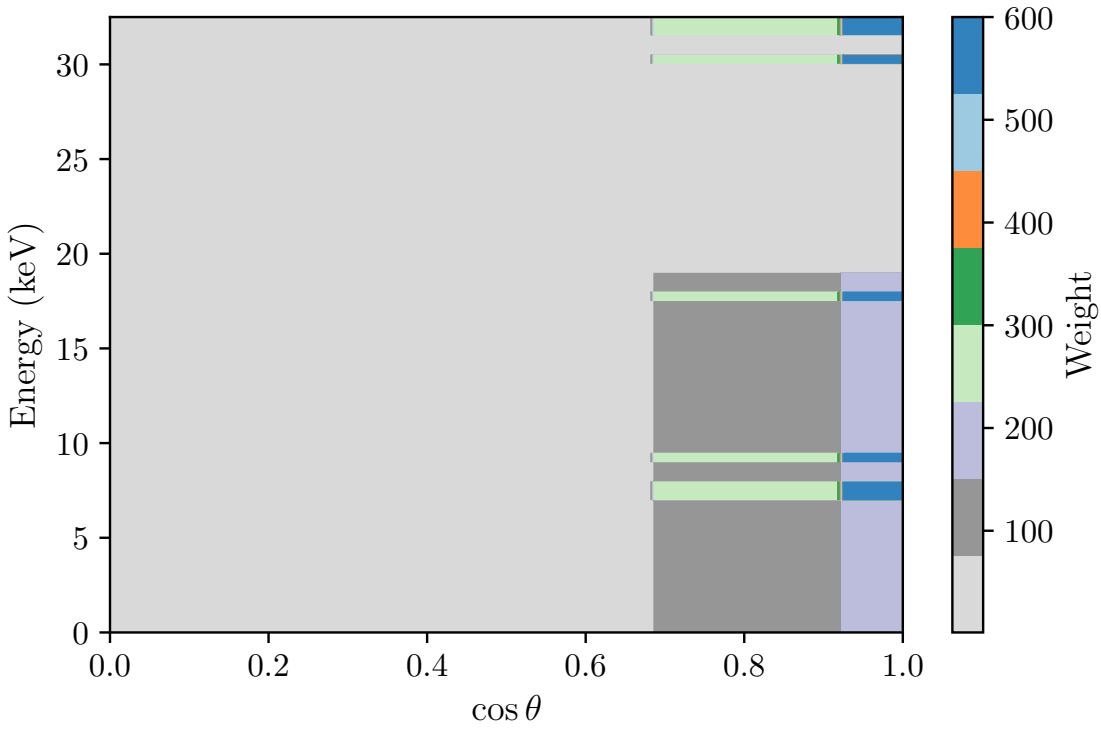

Figure C.1: Statistical weights applied to the number of simulated electrons for the new RW response matrices.

Appendix D

FTIR spectrometer acquisition and data analysis parameters

Table D.1: Most important spectrum parameters selected for data acquisition with the FTIR spectrometer.

Parameter	Value
Resolution	$1\,\mathrm{cm}^{-1}$
Aperture setting	6 mm
Source setting	MIR
Detector setting	RT-DLaTGS
Scans	16
Scan time	47.7 s
Scanner velocity	10 kHz
Acquisition mode	Double sided, forward-backward
Apodization function	Norton-Beer, medium
Phase resolution	6.00
Zero filling factor	2

Table D.2: Integration ranges and RCF baseline correction parameters used in the FTIR data analysis.

Molecule	Integration range (cm^{-1})	RCF parameters $r_{\tilde{\nu}}$ (cm^{-1}), r_I
O_3	950 – 1080	–
CO_2	2280 – 2400	345, -0.065
H_2O	1630 – 2100	450, -0.01
D_2O	2450 – 2825	600, -0.01

Appendix E

Pressure-dependence of ozone concentrations

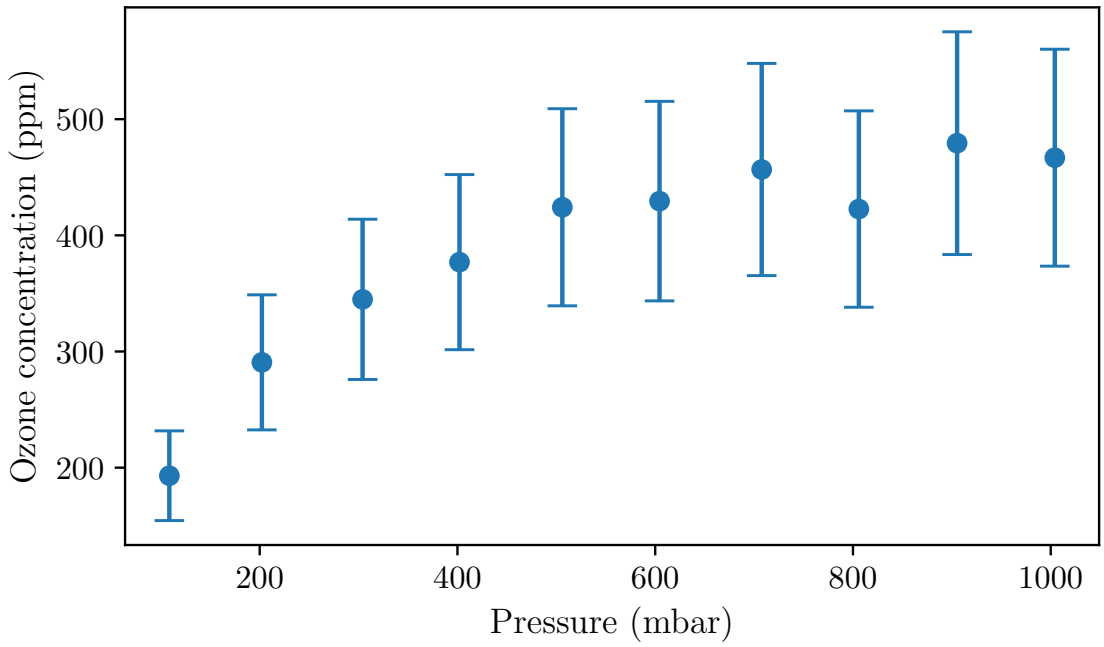

Figure E.1: Ozone concentration at equilibrium over pressure.

Appendix F

First phase of UV/ozone decontamination of the KATRIN RW

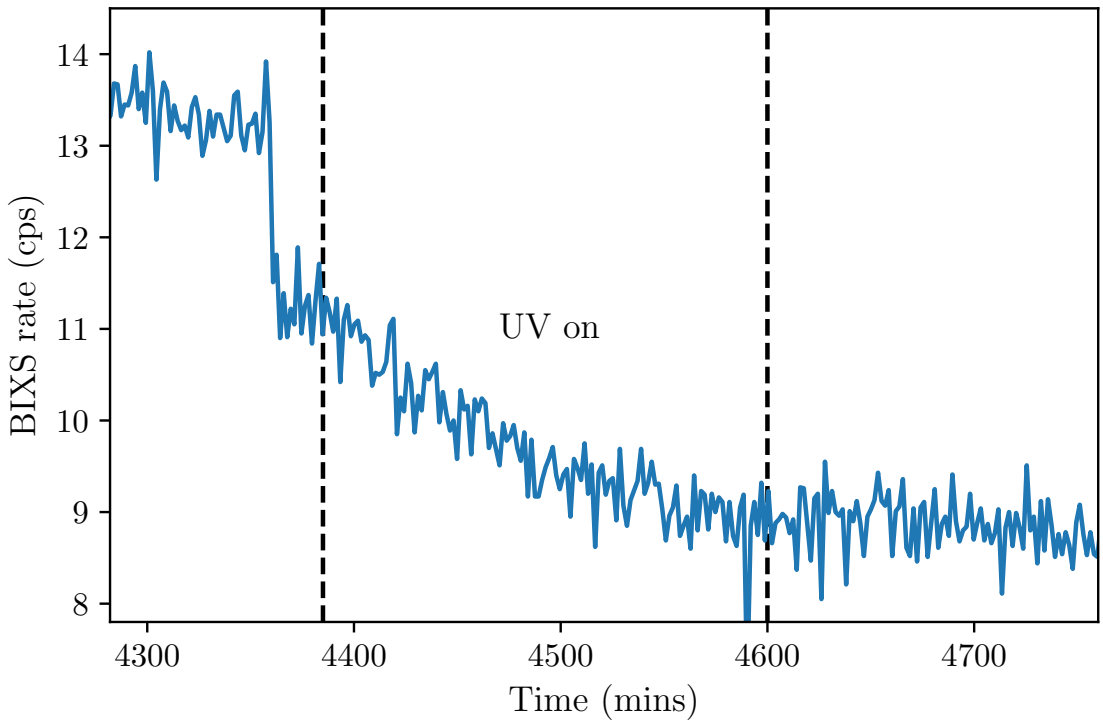

Figure F.1: BIXS rate representing near-surface activity of the KATRIN RW during the first hours of UV/ozone decontamination. Over the course of about 3.5 hours, the activity could be decreased by roughly 20%.

Appendix G

TRACE sample ex-situ decontamination and LSC analysis

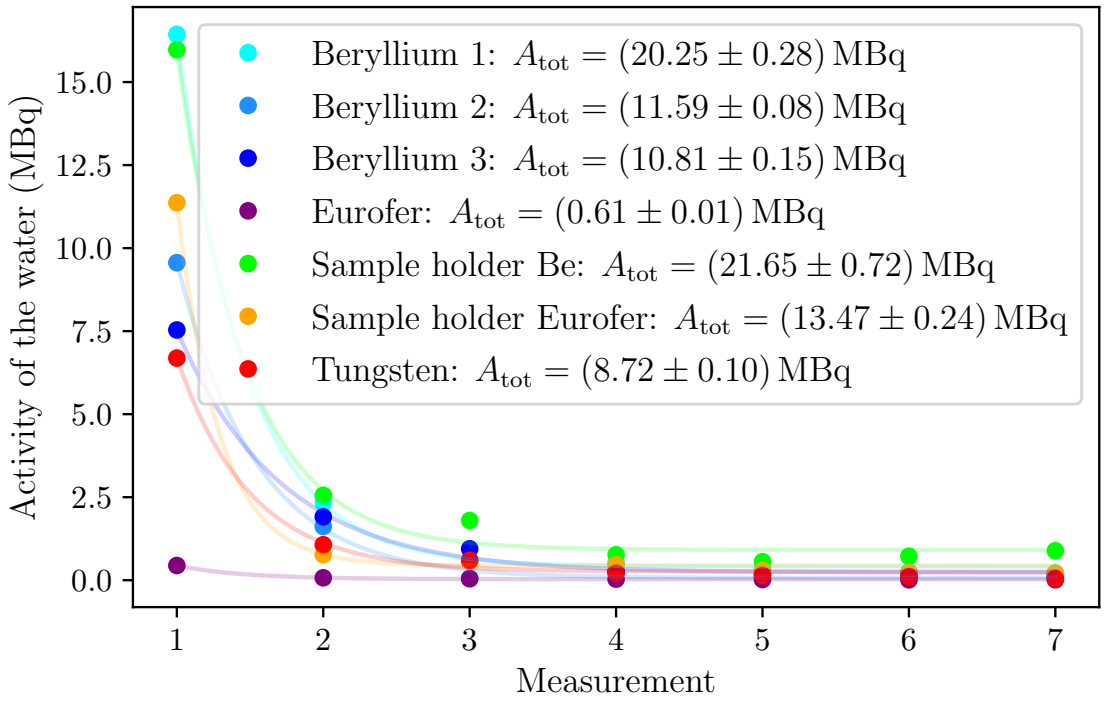

Figure G.1: Results of Total activities determined by decontaminating the TRACE samples in an ultrasonic bath and measuring the water's activity with liquid scintillation counting. The activities given are expected to have been homogeneously distributed across the sample surface, which is consistent with the BIXS measurements. Data kindly provided by M. Schaufelberger.

Bibliography

Abazajian, K., Fuller, G. M., & Patel, M. (2001). Sterile neutrino hot, warm, and cold dark matter. *Phys. Rev. D*, *64*, 023501. doi: 10.1103/PhysRevD.64.023501.

Acharya, H., Aker, M., Batzler, D., Beglarian, A., Beisenkötter, J., Biassoni, M., Bieringer, B., Biondi, Y., Block, F., Bornschein, B., Bornschein, L., Böttcher, M., Carminati, M., Chatrabhuti, A., Chilingaryan, S., Daniel, B. A., Descher, M., Barrero, D. D., Dragoun, O., ... Zeller, G. (2025). Measurement of the inhomogeneity of the KATRIN tritium source electric potential by high-resolution spectroscopy of conversion electrons from ^{83m}Kr. doi: 10.48550/arXiv.2503.13221.

Agostinelli, S., Allison, J., Amako, K., Apostolakis, J., Araujo, H., Arce, P., Asai, M., Axen, D., Banerjee, S., Barrand, G., Behner, F., Bellagamba, L., Boudreau, J., Broglia, L., Brunengo, A., Burkhardt, H., Chauvie, S., Chuma, J., Chytracek, R., ... Zschiesche, D. (2003). Geant4—a simulation toolkit. *Nuclear Instruments and Methods in Physics Research Section A: Accelerators, Spectrometers, Detectors and Associated Equipment*, *506*(3), 250–303. doi: 10.1016/S0168-9002(03)01368-8.

Aker, M., Altenmüller, K., Arenz, M., Babutzka, M., Barrett, J., Bauer, S., Beck, M., Beglarian, A., Behrens, J., Bergmann, T., Besserer, U., Blaum, K., Block, F., Bobien, S., Bokeloh, K., Bonn, J., Bornschein, B., Bornschein, L., Bouquet, H., ... Zeller, G. (2019). Improved Upper Limit on the Neutrino Mass from a Direct Kinematic Method by KATRIN. *Phys. Rev. Lett.*, *123*, 221802. doi: 10.1103/PhysRevLett.123.221802.

Aker, M., Altenmüller, K., Amsbaugh, J., Arenz, M., Babutzka, M., Bast, J., Bauer, S., Bechtler, H., Beck, M., Beglarian, A., Behrens, J., Bender, B., Berendes, R., Berlev, A., Besserer, U., Bettin, C., Bieringer, B., Blaum, K., Block, F., ... Zeller, G. (2021a). The design, construction, and commissioning of the KATRIN experiment. *Journal of Instrumentation*, *16*(08), T08015. doi: 10.1088/1748-0221/16/08/T08015.

Aker, M., Altenmüller, K., Beglarian, A., Behrens, J., Berlev, A., Besserer, U., Bieringer, B., Blaum, K., Block, F., Bornschein, B., Bornschein, L., Böttcher, M., Brunst, T., Caldwell, T. S., La Cascio, L., Chilingaryan, S., Choi, W., Díaz Barrero, D., Debowski, K., ... Zeller, G. (2021b). Analysis methods for the first KATRIN neutrino-mass measurement. *Phys. Rev. D*, *104*, 012005. doi: 10.1103/PhysRevD.104.012005.

Aker, M., Beglarian, A., Behrens, J., Berlev, A., Besserer, U., Bieringer, B., Block, F., Bobien, S., Böttcher, M., Bornschein, B., Bornschein, L., Brunst, T., Caldwell,

T. S., Carney, R. M. D., La Cascio, L., Chilingaryan, S., Choi, W., Debowski, K., Deffert, M., ... Zeller, G. (2022). Direct neutrino-mass measurement with sub-electronvolt sensitivity. *Nature Physics*, *18*(2), 160–166. doi: 10.1038/s41567-021-01463-1.

Aker, M., Batzler, D., Beglarian, A., Behrens, J., Berlev, A., Besserer, U., Bieringer, B., Block, F., Bobien, S., Bornschein, B., Bornschein, L., Böttcher, M., Brunst, T., Caldwell, T. S., Chilingaryan, S., Choi, W., Debowski, K., Descher, M., Barrero, D. D., ... Zeller, G. (2023). Search for keV-scale sterile neutrinos with the first KATRIN data. *The European Physical Journal C*, *83*(8). doi: 10.1140/epjc/s10052-023-11818-y.

Aker, M., Sturm, M., Priester, F., Tirolf, S., Batzler, D., Größle, R., Marsteller, A., Röllig, M., & Schlösser, M. (2024). In Situ Tritium Decontamination of the KATRIN Rear Wall Using an Ultraviolet/Ozone Treatment. *Fusion Science and Technology*, *80*(3-4), 303–310. doi: 10.1080/15361055.2023.2214695.

Aker, M., Batzler, D., Beglarian, A., Behrens, J., Beisenkötter, J., Biassoni, M., Bieringer, B., Biondi, Y., Block, F., Bobien, S., Böttcher, M., Bornschein, B., Bornschein, L., Caldwell, T. S., Carminati, M., Chatrabhuti, A., Chilingaryan, S., Daniel, B. A., Debowski, K., ... Zeller, G. (2025). Direct neutrino-mass measurement based on 259 days of KATRIN data. *Science*, *388*(6743), 180–185. doi: 10.1126/science.adq9592.

Aker, M. J. (2025). *Tritium Sorption on the KATRIN Rear Wall: Effects, Dynamics and Mitigation* [Ph.D. thesis]. Karlsruher Institut für Technologie (KIT). Karlsruher Institut für Technologie (KIT). doi: 10.5445/IR/1000178375.

Allison, J., Amako, K., Apostolakis, J., Araujo, H., Arce Dubois, P., Asai, M., Barrand, G., Capra, R., Chauvie, S., Chytracek, R., Cirrone, G., Cooperman, G., Cosmo, G., Cuttone, G., Daquino, G., Donszelmann, M., Dressel, M., Folger, G., Foppiano, F., ... Yoshida, H. (2006). Geant4 developments and applications. *IEEE Transactions on Nuclear Science*, *53*(1), 270–278. doi: 10.1109/TNS.2006.869826.

Allison, J., Amako, K., Apostolakis, J., Arce, P., Asai, M., Aso, T., Bagli, E., Bagulya, A., Banerjee, S., Barrand, G., Beck, B., Bogdanov, A., Brandt, D., Brown, J., Burkhardt, H., Canal, P., Cano-Ott, D., Chauvie, S., Cho, K., ... Yoshida, H. (2016). Recent developments in Geant4. *Nuclear Instruments and Methods in Physics Research Section A: Accelerators, Spectrometers, Detectors and Associated Equipment*, *835*, 186–225. doi: 10.1016/j.nima.2016.06.125.

Amsbaugh, J., Barrett, J., Beglarian, A., Bergmann, T., Bichsel, H., Bodine, L., Bonn, J., Boyd, N., Burritt, T., Chaoui, Z., Chilingaryan, S., Corona, T., Doe, P., Dunmore, J., Enomoto, S., Formaggio, J., Fränkle, F., Furse, D., Gemmeke, H., ... Wüstling, S. (2015). Focal-plane detector system for the KATRIN experiment. *Nuclear Instruments and Methods in Physics Research Section A: Accelerators, Spectrometers, Detectors and Associated Equipment*, *778*, 40–60. doi: 10.1016/j.nima.2014.12.116.

Apostolakis, J., Asai, M., Bogdanov, A., Burkhardt, H., Cosmo, G., Elles, S., Folger, G., Grichine, V., Gumplinger, P., Heikkinen, A., Hrivnacova, I., Ivanchenko, V., Jacquemier, J., Koi, T., Kokoulin, R., Kossov, M., Kurashige, H., McLaren, I.,

Link, O., ... Wright, D. (2009). Geometry and physics of the Geant4 toolkit for high and medium energy applications [Workshop on Use of Monte Carlo Techniques for Design and Analysis of Radiation Detectors]. *Radiation Physics and Chemistry*, *78*(10), 859–873. doi: 10.1016/j.radphyschem.2009.04.026.

Aseev, V. N., Belesev, A. I., Berlev, A. I., Geraskin, E. V., Golubev, A. A., Likhovid, N. A., Lobashev, V. M., Nozik, A. A., Pantuev, V. S., Parfenov, V. I., Skasyrskaya, A. K., Tkachov, F. V., & Zadorozhny, S. V. (2011). Upper limit on the electron antineutrino mass from the Troitsk experiment. *Phys. Rev. D*, *84*, 112003. doi: 10.1103/PhysRevD.84.112003.

Auger, P. (1923). Sur les rayons β secondaires produits dans un gaz par des rayons X. *CR Acad. Sci.(f)*, *177*, 169.

Babutzka, M. (2014). *Design and development for the Rearsection of the KATRIN experiment* [Ph.D. thesis]. Karlsruher Institut für Technologie (KIT). doi: 10.5445/IR/1000045598.

Barrero, D. D., Le, T. L., Niemes, S., Welte, S., Schlösser, M., Bornschein, B., & Telle, H. H. (2024). Generation and Analysis of Tritium-Substituted Methane. *Fusion Science and Technology*, *80*(3-4), 530–539. doi: 10.1080/15361055.2023.2194235.

Batzler, D., Aker, M., Größle, R., Kurz, D., Marsteller, A., Priester, F., Sturm, M., & Winney, P. (2024). Monitoring of ozone production and depletion rates in a tritium-compatible system. *Fusion Engineering and Design*, *203*, 114425. doi: 10.1016/j.fusengdes.2024.114425.

Batzler, D., Aker, M., Braun, J. R., Größle, R., Haag, P., Röllig, M., Roodt, D. R., Schäfer, M.-C., & Schaufelberger, M. (2025). In-situ measurement of tritium accumulation and decontamination of tungsten. *Fusion Engineering and Design*, *216*, 115041. doi: 10.1016/j.fusengdes.2025.115041.

Bekki, S. & Lefevre, F. (2009). Stratospheric ozone: History and concepts and interactions with climate. *EPJ Web of Conferences*, *1*, 113–136. doi: 10.1140/epjconf/e2009-00914-y.

Block, F. (2022). *Determination of Electromagnetic Fields and Tritium Column Density for Neutrino Mass Analysis with KATRIN* [Ph.D. thesis]. Karlsruher Institut für Technologie (KIT) [51.13.01; LK 01]. Karlsruher Institut für Technologie (KIT). doi: 10.5445/IR/1000145073.

Bodine, L. I., Parno, D. S., & Robertson, R. G. H. (2015). Assessment of molecular effects on neutrino mass measurements from tritium β decay. *Phys. Rev. C*, *91*, 035505. doi: 10.1103/PhysRevC.91.035505.

Chang, C. C. (1971). Auger electron spectroscopy. *Surface Science*, *25*(1), 53–79. doi: https://doi.org/10.1016/0039-6028(71)90210-X.

Chapman, S. (1930). XXXV. On ozone and atomic oxygen in the upper atmosphere. *The London, Edinburgh, and Dublin Philosophical Magazine and Journal of Science*, *10*(64), 369–383. doi: 10.1080/14786443009461588.

Coghlan, W., & Clausing, R. (1973). Auger catalog calculated transition energies listed by energy and element. *Atomic Data and Nuclear Data Tables*, *5*(4), 317–469. doi: 10.1016/S0092-640X(73)80005-1.

Criegee, R. (1975). Mechanism of Ozonolysis. *Angewandte Chemie International Edition in English*, *14*(11), 745–752. doi: 10.1002/anie.197507451.

Darlington, E. H. (1975). Backscattering of 10-100 keV electrons from thick targets. *Journal of Physics D: Applied Physics*, *8*(1), 85. doi: 10.1088/0022-3727/8/1/016.

De, S., Zhang, J., Luque, R., & Yan, N. (2016). Ni-based bimetallic heterogeneous catalysts for energy and environmental applications. *Energy Environ. Sci.*, *9*, 3314–3347. doi: 10.1039/C6EE02002J.

Descher, M. (2024). *Differential spectrum modeling and sensitivity for keV sterile neutrino search at KATRIN* [Ph.D. thesis]. Karlsruher Institut für Technologie (KIT). Karlsruher Institut für Technologie (KIT). doi: 10.5445/IR/1000166956.

Dhandapani, B., & Oyama, S. (1997). Gas phase ozone decomposition catalysts. *Applied Catalysis B: Environmental*, *11*(2), 129–166. doi: 10.1016/S0926-3373(96)00044-6.

Dickson, R. S. (1990, November). Tritium interactions with steel and construction materials in fusion devices. A literature review.

Dodelson, S., & Widrow, L. M. (1994). Sterile neutrinos as dark matter. *Phys. Rev. Lett.*, *72*, 17–20. doi: 10.1103/PhysRevLett.72.17.

Dolgov, A., & Hansen, S. (2002). Massive sterile neutrinos as warm dark matter. *Astroparticle Physics*, *16*(3), 339–344. doi: https://doi.org/10.1016/S0927-6505(01)00115-3.

Dondero, P., Mantero, A., Ivanchencko, V., Lotti, S., Mineo, T., & Fioretti, V. (2018). Electron backscattering simulation in Geant4. *Nuclear Instruments and Methods in Physics Research Section B: Beam Interactions with Materials and Atoms*, *425*, 18–25. doi: 10.1016/j.nimb.2018.03.037.

Dütsch, H. U. (1968). The photochemistry of stratospheric ozone. *Quarterly Journal of the Royal Meteorological Society*, *94*(402), 483–497. doi: 10.1002/qj.49709440205.

Fermi, E. (1934). Versuch einer Theorie der β-Strahlen. I. *Zeitschrift für Physik*, *88*(3), 161–177. doi: 10.1007/bf01351864.

Flaud, J.-M., Piccolo, C., Carli, B., Perrin, A., Coudert, L., Teffo, J., & Brown, L. (2003). Molecular line parameters for the MIPAS (Michelson Interferometer for Passive Atmospheric Sounding) experiment. *Atmospheric and Oceanic Optics*, *16*, 172–182.

Gaganidze, E., Gillemot, F., Szenthe, I., Gorley, M., Rieth, M., & Diegele, E. (2018). Development of EUROFER97 database and material property handbook. *Fusion Engineering and Design*, *135*, 9–14. doi: https://doi.org/10.1016/j.fusengdes.2018.06.027.

Geletneky, C., & Berger, S. (1998). The Mechanism of Ozonolysis Revisited by 17O-NMR Spectroscopy. *European Journal of Organic Chemistry*, *1998*(8), 1625–1627. doi: 10.1002/(SICI)1099-0690(199808)1998:8¡1625::AID-EJOC1625¿3.0.CO;2-L.

Gentile, C., Parker, J., Guttadora, G., & Ciebiera, L. (2002). Oxidative Tritium Decontamination System, 159–163. doi: 10.1109/FUSION.2002.1027666.

Gill, J. T. (1980). Effect of container preparation on the growth of protium and methane impurities into tritium gas. *Journal of Vacuum Science and Technology*, *17*(2), 645–654. doi: 10.1116/1.570532.

Gordon, I., Rothman, L., Hargreaves, R., Hashemi, R., Karlovets, E., Skinner, F., Conway, E., Hill, C., Kochanov, R., Tan, Y., Wcisło, P., Finenko, A., Nelson, K., Bernath, P., Birk, M., Boudon, V., Campargue, A., Chance, K., Coustenis, A., ... Yurchenko, S. (2022). The HITRAN2020 molecular spectroscopic database. *Journal of Quantitative Spectroscopy and Radiative Transfer*, *277*, 107949. doi: 10.1016/j.jqsrt.2021.107949.

Griffiths, P. R., & De Haseth, J. A. (2007). *Fourier Transform Infrared Spectrometry* (2nd ed.). Wiley.

Größle, R. (2015). Das TapIR Experiment - IR-Absorptionsspektren flüssiger Wasserstoffisotopologe. doi: 10.5445/IR/1000055643.

Henke, B., Gullikson, E., & Davis, J. (1993). X-Ray Interactions: Photoabsorption, Scattering, Transmission, and Reflection at E = 50-30,000 eV, Z = 1-92. *Atomic Data and Nuclear Data Tables*, *54*(2), 181–342. doi: 10.1006/adnd.1993.1013.

Hillesheimer, D., Marsteller, A., Priester, F., Röllig, M., Sturm, M., Welte, S., Wydra, J., Bornschein, L., Falke, T., Weber, T., Tuchscherer, N., Le, T.-L., & and, S. N. (2023). Four Years of Tritium Operation of the KATRIN Experiment at TLK. *Fusion Science and Technology*, *80*(3-4), 465–471. doi: 10.1080/15361055.2023.2209691.

Houston, P. L. (2004). *Photodissociation dynamics of ozone in the Hartley band*. World Scientific. doi: 10.1142/9789812565808˙0006.

Huber, A. (2021). *Analysis of first KATRIN data and searches for keV-scale sterile neutrinos* [Ph.D. thesis]. Karlsruher Institut für Technologie (KIT). Karlsruher Institut für Technologie (KIT). doi: 10.5445/IR/1000128344.

Hunger, H.-J., & Küchler, L. (1979). Measurements of the electron backscattering coefficient for quantitative EPMA in the energy range of 4 to 40 keV. *physica status solidi (a)*, *56*(1), K45–K48. doi: 10.1002/pssa.2210560157.

Ishikawa, Y., & Hirose, H. Y. (1997). Etching of Nondiamond Carbon in Diamond Thin Films Synthesized by Hot-Filament Chemical Vapor Deposition with Ultraviolet Irradiation. *Japanese Journal of Applied Physics*, *36*(3R), 1233. doi: 10.1143/JJAP.36.1233.

Ivanchenko, V. N., Kadri, O., Maire, M., & Urban, L. (2010). Geant4 models for simulation of multiple scattering. *Journal of Physics: Conference Series*, *219*(3), 032045. doi: 10.1088/1742-6596/219/3/032045.

Kellerer, J. (2022). *Simulation of the KATRIN Source Plasma using Monte Carlo and Particle in Cell Methods* [Ph.D. thesis]. Karlsruher Institut für Technologie (KIT). Karlsruher Institut für Technologie (KIT). doi: 10.5445/IR/1000143868.

Kikuchi, M. (2012). *Fusion physics*. IAEA.

Kim, S. H., Pia, M. G., Basaglia, T., Han, M. C., Hoff, G., Kim, C. H., & Saracco, P. (2015). Validation Test of Geant4 Simulation of Electron Backscattering. *IEEE Transactions on Nuclear Science*, *62*(2), 451–479. doi: 10.1109/TNS.2015.2401055.

Kleesiek, M., Behrens, J., Drexlin, G., Eitel, K., Erhard, M., Formaggio, J. A., Glück, F., Groh, S., Hötzel, M., Mertens, S., Poon, A. W. P., Weinheimer, C., & Valerius, K. (2019). β-Decay spectrum, response function and statistical model for neutrino mass measurements with the KATRIN experiment. *The European Physical Journal C*, *79*(3). doi: 10.1140/epjc/s10052-019-6686-7.

Krasznai, J. P., & Mowat, R. (1995). UV/Ozone Treatment to Decontaminate Tritium Contaminated Surfaces. *Fusion Technology*, *28*(3P2), 1336–1341. doi: 10.13182/FST95-A30597.

Kraus, C., Bornschein, B., Bornschein, L., Bonn, J., Flatt, B., Kovalik, A., Ostrick, B., Otten, E. W., Schall, J. P., Thümmler, T., & Weinheimer, C. (2005). Final results from phase II of the Mainz neutrino mass searchin tritium β decay. *The European Physical Journal C*, *40*(4), 447–468. doi: 10.1140/epjc/s2005-02139-7.

Kuckert, L. (2016). *The Windowless Gaseous Tritium Source of the KATRIN Experiment - Characterisation of Gas Dynamical and Plasma Properties* [Ph.D. thesis]. Karlsruher Institut für Technologie (KIT). Karlsruher Institut für Technologie (KIT). doi: 10.5445/IR/1000065077.

Larsen, G. K., Nguyen, K., & Murph, S. E. H. (2022). Preventing Tritium Memory Effects in Ion Chambers Using Ultraviolet LEDs. *IEEE Transactions on Nuclear Science*, *69*(5), 1092–1097. doi: 10.1109/TNS.2022.3163630.

Li, Y., Jiang, Y., Liu, X., Bai, Q., Liu, H., Wang, J., Zhang, P., Lu, L., & Yuan, X. (2022). Influence of reactive oxygen species concentration and ambient temperature on the evolution of chemical bonds during plasma cleaning: a molecular dynamics simulation. *RSC Adv.*, *12*, 30754–30763. doi: 10.1039/D2RA05901K.

Lobashev, V. (2003). The search for the neutrino mass by direct method in the tritium beta-decay and perspectives of study it in the project KATRIN. *Nuclear Physics A*, *719*, C153–C160. doi: 10.1016/S0375-9474(03)00985-0.

Lobashev, V., & Spivak, P. (1985). A method for measuring the electron antineutrino rest mass. *Nuclear Instruments and Methods in Physics Research Section A: Accelerators, Spectrometers, Detectors and Associated Equipment*, *240*(2), 305–310. doi: 10.1016/0168-9002(85)90640-0.

Lucas, L., & Unterweger, M. (2000). Comprehensive review and critical evaluation of the half-life of tritium. *Journal of Research of the National Institute of Standards and Technology*, *105*(4), 541. doi: 10.6028/jres.105.043.

Marsteller, A., Bornschein, B., Bornschein, L., Drexlin, G., Friedel, F., Gehring, R., Grohmann, S., Gumbsheimer, R., Hackenjos, M., Jansen, A., Kosmider, A., La Cascio, L., Lichter, S., Müller, K., Priester, F., Rinderspacher, R., Röllig, M., Röttele, C., Sharipov, F., … Wolf, J. (2021). Neutral tritium gas reduction in the KATRIN differential pumping sections. *Vacuum*, *184*, 109979. doi: 10.1016/j.vacuum.2020.109979.

Marsteller, A., Böttcher, M., Bornschein, B., Enomoto, S., Fengler, C., Lebeda, O., Machatschek, M., Priester, F., Ráliš, J., Röllig, M., Röttele, C., Schlösser, M., Michal, Š., Sturm, M., & Vénos, D. (2022). Operation modes of the KATRIN experiment Tritium Loop System using 83mKr. *Journal of Instrumentation*, *17*(12), P12010. doi: 10.1088/1748-0221/17/12/P12010.

Marsteller, A. C. (2020). *Characterization and Optimization of the KATRIN Tritium Source* [Ph.D. thesis]. Karlsruher Institut für Technologie (KIT). Karlsruher Institut für Technologie (KIT). doi: 10.5445/IR/1000127553.

Matsuyama, M., Watanabe, K., & Hasegawa, K. (1998). Tritium assay in materials by the bremsstrahlung counting method. *Fusion Engineering and Design*, *39-40*, 929–936. doi: 10.1016/S0920-3796(98)00232-4.

McClurkin, J. D., & Maier, D. E. (2010). Half-life time of ozone as a function of air conditions and movement. *Proceedings of the 10th International Working Conference on Stored Product Protection, 27 June to 2 July 2010 Estoril, Portugal*, *425*(1), 381–385. doi: 10.5073/20141204-132222.

McDonald, A. B., Ahmad, Q. R., Allen, R. C., Andersen, T. C., Anglin, J. D., Barton, J. C., Beier, E. W., Bercovitch, M., Bigu, J., Biller, S. D., Black, R. A., Blevis, I., Boardman, R. J., Boger, J., Bonvin, E., Boulay, M. G., Bowler, M. G., Bowles, T. J., Brice, S. J., ... Yeh, M. (2002). Direct Evidence for Neutrino Flavor Transformation from Neutral-Current Interactions in SNO. *AIP Conference Proceedings*, *646*(1), 43–58. doi: 10.1063/1.1524553.

Meitner, L. (1922). Über die Entstehung der β-Strahl-Spektren radioaktiver Substanzen. *Zeitschrift für Physik*, *9*(1), 131–144. doi: 10.1007/bf01326962.

Mertens, S., Lasserre, T., Groh, S., Drexlin, G., Glück, F., Huber, A., Poon, A., Steidl, M., Steinbrink, N., & Weinheimer, C. (2015). Sensitivity of next-generation tritium beta-decay experiments for keV-scale sterile neutrinos. *Journal of Cosmology and Astroparticle Physics*, *2015*(02), 020. doi: 10.1088/1475-7516/2015/02/020.

Mertens, S., Alborini, A., Altenmüller, K., Bode, T., Bombelli, L., Brunst, T., Carminati, M., Fink, D., Fiorini, C., Houdy, T., Huber, A., Korzeczek, M., Lasserre, T., Lechner, P., Manotti, M., Peric, I., Radford, D. C., Siegmann, D., Slezák, M., ... Wüstling, S. (2019). A novel detector system for KATRIN to search for keV-scale sterile neutrinos. *Journal of Physics G: Nuclear and Particle Physics*, *46*(6), 065203. doi: 10.1088/1361-6471/ab12fe.

Minkowski, P. (1977). $\mu \to e\gamma$ at a rate of one out of 109 muon decays? *Physics Letters B*, *67*(4), 421–428. doi: 10.1016/0370-2693(77)90435-X.

Mirz, S., Groessle, R., & Kraus, A. (2019). Optimization and quantification of the systematic effects of a rolling circle filter for spectral pre-processing. *Analyst*, *144*, 4281–4287. doi: 10.1039/C8AN02476F.

Mohapatra, R. N., & Senjanović, G. (1980). Neutrino Mass and Spontaneous Parity Nonconservation. *Phys. Rev. Lett.*, *44*, 912–915. doi: 10.1103/PhysRevLett.44.912.

Morris, G. (1977). *Methane Formation in Tritium Gas exposed to Stainless Steel* (tech. rep.). Lawrence Livermore National Lab.(LLNL), Livermore, CA (United States).

Musket, R. (1989). Cleaning surfaces of sintered beryllium oxide. *Applied Surface Science*, *37*(1), 55–62. doi: 10.1016/0169-4332(89)90973-2.

Myers, E. G., Wagner, A., Kracke, H., & Wesson, B. A. (2015). Atomic Masses of Tritium and Helium-3. *Phys. Rev. Lett.*, *114*, 013003. doi: 10.1103/PhysRevLett.114.013003.

Otten, E. W., & Weinheimer, C. (2008). Neutrino mass limit from tritium β decay. *Reports on Progress in Physics*, *71*(8), 086201. doi: 10.1088/0034-4885/71/8/086201.

Oya, Y., Shu, W., O'hira, S., Hayashi, T., Nakamura, H., Sakai, T., Tadokoro, T., Kobayashi, K., Suzuki, T., & Nishi, M. (2001). A study of tritium decontamination of deposits by UV irradiation [14th Int. Conf. on Plasma-Surface Interactions in Controlled Fu-

sion Devices]. *Journal of Nuclear Materials*, *290-293*, 469–472. doi: 10.1016/S0022-3115(00)00440-2.

Perkins, S. T., Cullen, D. E., Chen, M. H., Rathkopf, J., Scofield, J., & Hubbell, J. H. (1991, October). *Tables and graphs of atomic subshell and relaxation data derived from the LLNL Evaluated Atomic Data Library (EADL), Z = 1–100* (tech. rep.). Lawrence Livermore National Lab. (LLNL), Livermore, CA (United States). doi: 10.2172/10121422.

Picard, A., Backe, H., Barth, H., Bonn, J., Degen, B., Edling, T., Haid, R., Hermanni, A., Leiderer, P., Loeken, T., Molz, A., Moore, R., Osipowicz, A., Otten, E., Przyrembel, M., Schrader, M., Steininger, M., & Weinheimer, C. (1992). A solenoid retarding spectrometer with high resolution and transmission for keV electrons. *Nuclear Instruments and Methods in Physics Research Section B: Beam Interactions with Materials and Atoms*, *63*(3), 345–358. doi: 10.1016/0168-583X(92)95119-C.

Prather, M. J., & Zhu, X. (2024). Lifetimes and timescales of tropospheric ozone. *Elementa: Science of the Anthropocene*, *12*(1), 00112. doi: 10.1525/elementa.2023.00112.

Röllig, M. (2015). *Tritium analytics by beta induced X-ray spectrometry* [Ph.D. thesis]. Karlsruhe Institute of Technology, Faculty of Physics. doi: 10.5445/IR/1000054050.

Röttele, C., Steidl, M., Sturm, M., Röllig, M., Marsteller, A., Schimpf, L., Friedel, F., Jansen, A., Gil, W., Schrank, M., Wolf, J., Drexlin, G., & Bornschein, B. (2023). Characterization of the KATRIN cryogenic pumping section. *Vacuum*, *208*, 111699. doi: 10.1016/j.vacuum.2022.111699.

Saenz, A., Jonsell, S., & Froelich, P. (2000). Improved Molecular Final-State Distribution of HeT^+ for the β-Decay Process of T_2. *Phys. Rev. Lett.*, *84*, 242–245. doi: 10.1103/PhysRevLett.84.242.

Salvat, F., Sempau, J., Fernandez-Varea, J., & Acosta, E. (2001). Penelope–a code system for monte carlo simulation of electron and photon transport. *Workshop Proceedings. Issy-les-Moulineaux, France*, 5–7.

Schechter, J., & Valle, J. W. F. (1980). Neutrino masses in SU(2) $\bigotimes$ U(1) theories. *Phys. Rev. D*, *22*, 2227–2235. doi: 10.1103/PhysRevD.22.2227.

Schinke, R., & McBane, G. C. (2010). Photodissociation of ozone in the Hartley band: Potential energy surfaces, nonadiabatic couplings, and singlet/triplet branching ratio. *The Journal of Chemical Physics*, *132*(4), 044305. doi: 10.1063/1.3299249.

Schneidewind, S., Schürmann, J., Lokhov, A., Weinheimer, C., & Saenz, A. (2024). Improved treatment of the T_2 molecular final-states uncertainties for the KATRIN neutrino-mass measurement. *The European Physical Journal C*, *84*(5). doi: 10.1140/epjc/s10052-024-12802-w.

Schönung, K. (2016). *Development of a Rear Wall for the KATRIN Rear Section and investigation of tritium compatibility of Rear Section components* [Ph.D. thesis]. Karlsruhe Institute of Technology, Faculty of Physics. doi: 10.5445/IR/1000056077.

Schumacher, U. (2001). Status and problems of fusion reactor development. *Naturwissenschaften*, *88*(3), 102–112. doi: 10.1007/s001140100214.

Sharpe, S. W., Johnson, T. J., Sams, R. L., Chu, P. M., Rhoderick, G. C., & Johnson, P. A. (2004). Gas-Phase Databases for Quantitative Infrared Spectroscopy. *Applied Spectroscopy*, *58*(12), 1452–1461. doi: 10.1366/0003702042641281.

Shi, D., Wojcieszak, R., Paul, S., & Marceau, E. (2019). Ni Promotion by Fe: What Benefits for Catalytic Hydrogenation? *Catalysts*, *9*(5). doi: 10.3390/catal9050451.

Shimizu, R. (1983). Quantitative Analysis by Auger Electron Spectroscopy. *Japanese Journal of Applied Physics*, *22*(11R), 1631. doi: 10.1143/JJAP.22.1631.

Shu, W. M., Kawakubo, Y., O'hira, S., Oya, Y., Hayashi, T., Nakamura, H., Iwai, Y., Nishi, M. F., Gentile, C. A., Skinner, C. H., Langish, S., Guttadora, G., Carpe, A., & and, K. M. Y. (2002). Tritium Decontamination of TFTR D-T Plasma Facing Components Using an Ultra Violet Laser. *Fusion Science and Technology*, *41*(3P2), 690–694. doi: 10.13182/FST02-A22675.

Siegmann, D., Edzards, F., Bruch, C., Biassoni, M., Carminati, M., Descher, M., Fiorini, C., Forstner, C., Gavin, A., Gugiatti, M., Hiller, R., Hinz, D., Houdy, T., Huber, A., King, P., Lechner, P., Lichter, S., Mießner, D., Nava, A., ... Mertens, S. (2024). Development of a silicon drift detector array to search for keV-scale sterile neutrinos with the KATRIN experiment. *Journal of Physics G: Nuclear and Particle Physics*, *51*(8), 085202. doi: 10.1088/1361-6471/ad4bf8.

Solovey, V. R., Yakubovsky, D. I., Ermolayev, G. A., Lebedinskij, Y. Y., Markeev, A. M., Voronov, A. A., Zamboni, F., Popok, V. N., Arsenin, A. V., Volkov, V. S., & Novikov, S. M. (2021). UV/Ozone Treatment and Open-Air Copper Plasmonics. *Journal of Physics: Conference Series*, *2015*(1), 012148. doi: 10.1088/1742-6596/2015/1/012148.

Sternheimer, R. M. (1952). The Density Effect for the Ionization Loss in Various Materials. *Phys. Rev.*, *88*, 851–859. doi: 10.1103/PhysRev.88.851.

Sternheimer, R., Berger, M., & Seltzer, S. (1984). Density effect for the ionization loss of charged particles in various substances. *Atomic Data and Nuclear Data Tables*, *30*(2), 261–271. doi: 10.1016/0092-640X(84)90002-0.

Sturm, M., Priester, F., Röllig, M., Röttele, C., Marsteller, A., Hillesheimer, D., Bornschein, L., Bornschein, B., Größle, R., & Welte, S. (2021). Kilogram scale throughput performance of the KATRIN tritium handling system. *Fusion Engineering and Design*, *170*, 112507. doi: 10.1016/j.fusengdes.2021.112507.

Tavassoli, A.-A., Alamo, A., Bedel, L., Forest, L., Gentzbittel, J.-M., Rensman, J.-W., Diegele, E., Lindau, R., Schirra, M., Schmitt, R., Schneider, H., Petersen, C., Lancha, A.-M., Fernandez, P., Filacchioni, G., Maday, M., Mergia, K., Boukos, N., Baluc, ... Lucon, E. (2004). Materials design data for reduced activation martensitic steel type EUROFER. *Journal of Nuclear Materials*, *329-333*, 257–262. doi: https://doi.org/10.1016/j.jnucmat.2004.04.020.

Tyuterev, V., Barbe, A., Mikhailenko, S., & Tashkun, S. (2014). Ozone 5 micron range revisited: accurate laboratory measurements and ab initio calculations. Retrieved from the S&MPO database (Ref. [1076]) In October 2016.

Vénos, D., Sentkerestiová, J., Dragoun, O., Slezák, M., Ryšavý, M., & Špalek, A. (2018). Properties of 83mKr conversion electrons and their use in the KATRIN experiment. *Journal of Instrumentation*, *13*(02), T02012. doi: 10.1088/1748-0221/13/02/T02012.

Vig, J. R. (1985). UV/ozone cleaning of surfaces. *Journal of Vacuum Science & Technology A*, *3*(3), 1027–1034. doi: 10.1116/1.573115.

Vig, J. R. (1992). Ultraviolet-ozone cleaning of semiconductor surfaces. *Research and Development Technical Report SLCET-TR-91-33, Army Research Laboratory*.

Wayne, R. P. (1969). *Singlet Molecular Oxygen*. John Wiley & Sons, Ltd. doi: 10.1002/9780470133378.ch4.

Wilkerson, J., Bowles, T., Friar, J., Robertson, R., Stephenson, G., Wark, D., & Knapp, D. (1991). Limit on νe mass from observation of the beta decay of molecular tritium. *Nuclear Physics B - Proceedings Supplements*, *19*, 215–224. doi: 10.1016/0920-5632(91)90202-P.

Yanagida, T. (1980). Horizontal Symmetry and Masses of Neutrinos. *Progress of Theoretical Physics*, *64*(3), 1103–1105. doi: 10.1143/PTP.64.1103.

Danksagung

Abschließend möchte ich noch all denjenigen danken, die in irgendeiner Weise zum Gelingen dieser Arbeit beigetragen haben.

Als erstes möchte ich mich bei Kathrin Valerius bedanken, die mich aus Eigeninitiative auf die offene Doktorandenstelle am TLK im Rahmen von KATRIN aufmerksam machte, womit das Abenteuer begonnen hat.

Ebenso gebührt mein Dank Guido Drexlin für das Ermöglichen dieses tollen Projekts. Er hat sich stets die Zeit für viele – zumindest für mich – sehr hilfreiche und inspirierende Diskussionen genommen.

Des Weiteren möchte ich mich bei Susanne Mertens bedanken, die sich bereit erklärt hat, die Rolle der Korreferentin zu übernehmen. Besonders durch die vielen Deep Model Besprechungen hatte ich immer wieder die Bestätigung erhalten, dass meine Arbeit zur RW sinnvoll und relevant für die KATRIN-Kollaboration war.

Besonderen Dank möchte ich Beate Bornschein für die schöne, hoffentlich noch lange andauernde Zeit am TLK aussprechen. Obwohl ich nun schon knapp vier Jahre dort angestellt bin, wächst meine Faszination für dieses einzigartige Labor von Tag zu Tag weiter.

Leider besitze ich nicht das nötige Vokabular um auszudrücken, wie dankbar ich meinem Gruppenleiter, Robin Größle, bin. Von unschätzbarem Wert war, dass er mir im Labor immer meinen Freiraum ließ, um meine Interessen zu fördern – auch bei Dingen, die nicht unmittelbar relevant für mein Projekt waren (Stichwort Wasserdetritiierung). Seine Expertise und sein Blickwinkel haben mich nachhaltig und maßgeblich geprägt.

Vielen Dank auch an Marco Röllig, der immer zur Stelle war, wenn es um Simulationen und TRACE ging, oder ich mal etwas "aktiver" an seiner Handschuhbox zugange war. Aus Fairnessgründen sehe ich davon ab, ihm eigene drei Seiten zu widmen, stattdessen erwähne ich ihn mehrfach.

Mein Dank gilt auch Florian Priester, Marco Röllig, Michael Sturm, Simon Niemes und Alexander Marsteller. Ihre Unterstützung war unentbehrlich für den Erfolg dieser Arbeit. Die LOOPS-Gruppensitzung freitags um 9 Uhr hat mir immer wieder geholfen, den letzten Tag vor dem Wochenende durchzustehen.

Für jegliche Arbeiten im Labor möchte ich folgenden Personen danken: Immanuel Müller für das Abfüllen von Tritium, Thanh-Long Le für das Zurücknehmen von verunreinigtem Tritium nach Ende meiner Messungen, und generell Adalbert Braun, Bernhard Heinle, Nancy Tuchscherer, Simone Wadle, Tobias Weber und Stefan Welte.

Ich danke Robin Größle, Alexander Marsteller, Marco Röllig (dreimal muss jetzt reichen) und Kerstin Trost für das Korrekturlesen der Arbeit und das hilfreiche Feedback.

Bedanken möchte ich mich auch bei all meinen Mitdoktoranden, insbesondere Max Aker und Johanna Wydra. Von Euch habe ich viel über das Doktorandsein gelernt.

Ganz besonderen Dank verdienen meine zahlreichen Studenten und HiWis: Daniel Kurz, Peter Winney, Semen Rusakov, Marius Schaufelberger, Marie-Christine Schäfer, Dylan Roodt, Philipp Haag und Kerstin Trost. My last student, Elizabeth Paine, indubitably deserves special thanks. You provided me with my final dataset, and with that opened up a whole lot of new questions that I didn't ask for. Cheers! Danke, dass ich an Euch meine Fähigkeiten als wissenschaftlicher Betreuer üben durfte!

Ebenso danke ich meinem ehemaligen Kommilitonen Robin Herlan. Gemeinsam haben wir das Studium gemeistert und durch Dich war auch so manche Vorlesung deutlich unterhaltsamer (wenn auch weniger vom Stoff hängengeblieben ist).

Zum Schluss bedanke ich mich von Herzen bei meinen Eltern und meiner Oma, die nie an mir gezweifelt haben und mich immer bei meiner Studien- bzw. Berufswahl unterstützt haben.